Ground calibration and flight data analysis of PoGOLite balloon experiment for cosmic gamma-ray polarization measurement

広島大学大学院理学研究科
高エネルギー宇宙・可視赤外線天文学研究室
M125560
河野 貴文
主査: 深澤 泰司
副査: 大川 正典

日付:2014/2/10

ABSTRACT

パルサー星雲における粒子加速は、詳細が未解明である宇宙線の加速起源候補の 1 つである。硬 X 線帯域で最も明るい天体であるパルサー星雲：”かに星雲”では、実際に粒子加速が起こっている証拠も確認されている。パルサー星雲内部における粒子の加速現場を特定する為には、磁場の情報を持つ偏光観測が有力な手段となるが、X 線・ガンマ線帯域で観測することは技術的に難しく、これまでの有意な検出結果は 2.6 keV, 5.2 keV (OSO-8 衛星)、100–1000 keV (INTEGRAL 衛星) の報告しかない。また、これらの結果ではエネルギー帯域によって偏光方位角が異なっているため、その間の帯域は非常に注目されている。

PoGOLite (Polarized Gamma-ray Observer: 左図) 気球実験では、日瑞米で協力し世界に先駆けて未観測である 25-80 keV の硬 X 線帯域での偏光測定を目指している。PoGOLite 検出器は、井戸型フォスイッチ構造のプラスチックシンチレータアレイを BGO アクティブシールドで囲みバックグラウンドを極限まで抑え、コンプトン散乱の異方性を利用することで偏光を検出する。本実験により新たな磁場情報を得て、粒子加速のジオメトリを制限出来ると期待される。

私は 2012 年および 2013 年に PoGOLite 放球前の較正試験にも参加し、^{241}Am からの 59.5 keV のガンマ線を延べ 150 時間以上にわたって主検出器に照射した。全較正試験データの解析を行うことで、右図のようなモジュレーションカーブや 61 本の PDC のイベント分布を得る事が出来た。この結果は、チーム内で行われたシミュレーション結果と比較し、シミュレーションにフィードバックをかけた。PoGOLite は 2013 年 7 月 14 日にスウェーデンのキルナ市にある Esrange 気球実験場から放球され、26 日にロシアのノリスクに着陸した。我々は約 2 週間のフライトを完遂し、かに星雲からの信号を検出している。本論文では、地上較正実験の結果とフライトデータの初期解析結果について報告する。

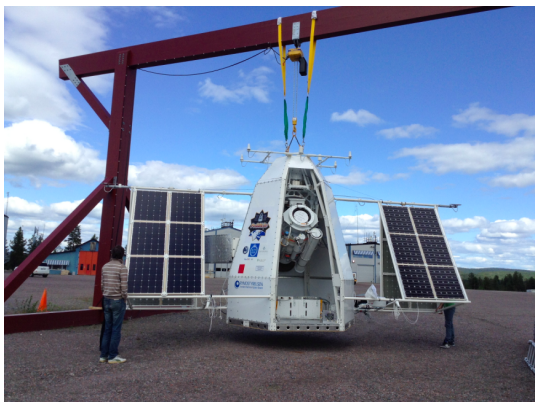

PoGOLite の外観、私がスウェーデン滞在時に撮影した。

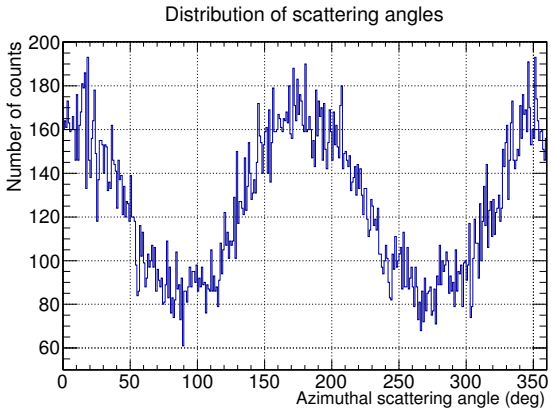

^{241}Am を用いた地上較正試験によって得られたモジュレーションカーブ

ABSTRACT

The particle acceleration in pulsar wind nebula is one of strong candidates of acceleration of cosmic ray. The acceleration of cosmic ray is still unsolved and one of the most important problem for science of astronomy. Crab nebula is a pulsar wind nebula, and is the brightest celestial object in X-ray.

The Crab nebula is one of the most studied objects in the Galaxy and there are evidences of particle acceleration. To identify the location of particle acceleration, polarization measurement will be powerful method since it is including informations of a magnetic field. However it is technically difficult to observe polarized X-ray and gamma-ray. Actually there is only a few measurements of polarization for Crab Nebula: 2.6 keV, 5.2 keV (OSO-8 satellite), and 100—1000 keV (INTEGRAL satellite). These results show different polarization angles at different energies. There is a energy gap between the past measurements, and needed to observe in the energy range to fill the energy gap.

The Polarized Gamma-ray Observer (PoGOLite) is a balloon-borne instrument that can measure gamma-ray polarization in the energy range of 25—80 keV. The instrument of PoGOLite adopts well-type phoswich counter and realize very low background. Utilizing anisotropy of Compton scattering against polarized gamma-rays, we can observe polarization from the target. The PoGOLite instrument has been constructed and tested with unpolarized and polarized gamma-ray of 59.5 keV from 241Am radioactive source, and results have been compared with simulations.

During July 14–26, 2013, there was a successful flight from Kiruna, Sweden to Norilsk, Russia. We have operated two-week flight and detected signals from Crab nebula, in this thesis I show the results of ground calibration and preliminary results of flight-data analysis.

CONTENTS

Chap.1 Introduction **9**
1.1 X-ray and gamma-ray polarimetry . . . 9
1.2 Measurement techniques . . . 9
1.2.1 Bragg reflection . . . 9
1.2.2 Photoelectric effect . . . 10
1.2.3 Compton scattering . . . 11
1.2.4 Pair production . . . 13
1.2.5 Modulation factor . . . 14
1.2.6 Minimum Detectable Polarization . . . 15
1.3 Target objects . . . 16
1.3.1 Crab nebula . . . 16
1.3.2 Cyg X-1 . . . 20
1.3.3 Short summary of past measurements . . . 25

Chap.2 The PoGOLite experiment **29**
2.1 Overview of the PoGOLite . . . 29
2.2 Main detector of PoGOLite . . . 30
2.3 Detection method of polarization . . . 31
2.4 The ground calibration with prototype detector . . . 33

Chap.3 Ground calibration **35**
3.1 Requirement of the ground calibration . . . 35
3.2 The ground calibration with the flight detector of PoGOLite . . . 36
3.2.1 Setup of the calibration . . . 36
3.2.2 The techniques to make modulation curve . . . 40
3.3 The results of the calibration . . . 42
3.3.1 Energy spectra . . . 42
3.3.2 Distribution of the interaction site among 61 PDCs . . . 42
3.3.3 Modulations curves . . . 49
3.3.4 Comparison with the simulation . . . 49
3.3.5 Changing threshold . . . 57
3.3.6 Summary and future works for the ground calibration . . . 61

Chap.4 Analysis of 2013-flight data **62**

Chap.5 Summary and future works **73**

Appendix A **74**

A.1 Modulation curves with some set up and event selection of the ground calibration 74

A.2 Comparison of modulation curves between the ground calibration (left) and the Geant4 simulation (right) 74

Appendix B **93**

B.1 2D histogram and the projection (means energy spectrum) with the threshold 0 ADC channel and 60 ADC channel 93

Appendix C **108**

C.1 Comparison between scattering event and absorption event of 2-hit event based on flight-data108

Appendix D **111**

D.1 List of grand calibration data 111

LIST of FIGURE

1.1 Mass attenuation coefficient (cm^2/g) for photon interactions in carbon, adopted from NIST. 10

1.2 Left: Concept diagram of focusing Bragg-crystal polarimeters. Right: Exploded view of OSO-1 polarimeter assembly. 11

1.3 Distribution in space of K-shell photo-electrons after the absorption of a polarized photo beam.[8] 12

1.4 Geometry of the Compton scattering process. 12

1.5 Three-dimensional geometry of the Compton scattering process. Left: The incident photon has momentum k_0 and polarization $\vec{e_0}$ along the z-axis and x-axis, respectively. It scatter toward the direction of a polar angle θ relative to the z-axis, whereafter it retains momentum $\vec{k_0}$. Right: ϕ is the azimuthal angle of the scattered photon with respect to the polarization vector of the incident photon. 13

1.6 The geometry of the pair production process [10]. Left: This is a general case for pair production. Vectors k, p^+ and p^- indicate the momenta of the incident photon, positron and electron, respectively. Angles θ^+ and θ^- are the polar angles of the positron and electron respect to the direction of incident photon (vector k). The polarization direction is indicated by ε, and Ψ is the angle between this direction and the projection of p^+ onto the plane perpendicular to the direction of the incident photon. Finally, ϕ is the angle between the projections of p^+ and p^- on this plane. Right: This is a special case ($\Phi = 180$ degree), but it is the most common ($\approx$80 %) in the co-planar case, i.e. the electron-positron pair is in the same plane as the incident photon. 14

1.7 An example of polarization-induced modulation. The the horizontal axis is azimuthal angle. A is an Amplitude of this curve, and B is a mean value of a fitted sinusoidal modulation curve. 15

1.8 Color composite of the Crab nebula, blue: Chandra X-ray image, green: Hubble Space Telescope optical image, red: Very Large Array radio image. 16

1.9 Cartoons of the Crab. Left: a simple X-ray structure of the Crab pulsar, inner ring (termination shock), torus and jets [13]. Right: conceptual diagram of pulsar wind nebula, pulsar wind (electron-positron pair) is emitted by pulsar, are accelerated to high energy at the termination shock, and emit synchrotron radiation. 17

1.10 The broad spectrum of the Crab nebula [14]. Below 1 GeV radiation is well described by synchrotron emission and above that due to inverse Compton scattering. 17

1.11 The polarization vectors for the Crab Nebula at (a) 2.6 keV and (b) 5.2 keV. Surrounding vectors in the order of increasing size correspond to the 67% and 99% confidence contours [15]. 18
1.12 The energy dependency of modulation factors for SPI and IBIS onboard INTEGRAL satellite [17]. 19
1.13 Left: The light curve of the Crab pulsar. There are two pulse phases (0.88 $<\phi<$ 0.14 and 0.25 $<\phi<$ 0.52), off-pulse phase (0.52 $<\phi<$0.88), and last phase called as "Bridge" phase (0.14 $<\phi<$ 0.25). The data for polarization analysis for INTEGRAL/SPI is selected from within the phase interval from 0.5 to 0.8 of the pulsar period (shaded area) in 100–1000 keV. Right: The composite image of the Crab, blue: Chandra X-ray image, green: Hubble Space Telescope optical image, and the gamma-ray polarization vector is superimposed with the limits on the direction of the vector (shaded area). The direction of the polarization vector is along with the jet. 20
1.14 The polarization of Crab nebula observed by INTEHRAL/IBIS. The polarization angle and polarization degree are measured for the Crab data between 200–800 keV, in the off-pulse (top), off-pulse and bridge (middle), and two-peak (bottom) phase intervals. The error bars for the profile are at 1σ. The 68%, 95%, and 99% confidence regions are shaded from dark to light gray. The SPI result [16] is indicated in the top figure by a cross [18]. . 21
1.15 The spectrum of Cyg X-1 observed by Suzaku satellite. Black: XIS (CCD), red: HXD-PIN, green: HXD-GSO. The spectrum in the high/soft state has a dominant soft emission below 10 keV while that in the low/hard state is dominated by higher energy component [19]. 22
1.16 The averaged polarization vectors for the Cyg X-1 at 2.6 keV and 5.2 keV [20]. 24
1.17 The energy spectrum of Cyg X-1 observed by INREGARL/IBIS. The spectral shape of Cyg X-1 requires the presence of two components, a cutoff power-law in 20 – 400 keV and a power-law spectrum up to 2000 keV [22]. 24
1.18 The polarization of Cyg X-1 observed by INTEGRAL/IBIS. The polarization angle and polarization degree are measured in 250–400 keV (left), and in 400—2000 keV (right). These results show that upper limit of 20 % in 250–400 keV and 67% $\pm$ 15% polarization degree with 40 $\pm$ 15 degree polarization angle in 400–2000 keV. [22] 25
1.19 The Cyg X-1 spectrum observed by INTEGRAL/SPI. Blue: "standard (single) events" in 22–2000 keV and " multiple event " in 130–2000 keV. The solid lines is the fit model composed of a thermal Comptonization plus a fixed cutoff power-law model (photon index = 1.6, E_{cut} = 700 keV; dashed line). 0.5% of systematic have been added to the data. [23] 26
1.20 The polarization of Cyg X-1 observed by INTEHRAL/SPI. Left columns are the polarization angle and polarization degree, and right columns are contours show that the confidence regions at 1σ, 2σ and 3σ, are shaded from dark to light gray. (i) to (iv) are in 130–230 keV, 230–370 keV, 370–850 keV, and 230–850 keV, respectively. [23] 27

2.1 The launch of PoGOLite from Esrange on July 12th 2013, 0818 UT. The distance from the top of the balloon to the gondola is ∼300 m. 30
2.2 Left: The main detector consists of 61well-type phoswich detector cells (PDCs) and 30 side anti-coincidence shields (SASs) with BGO for PoGOLite. Right: One of phoswich detector cells (PDCs), which is consisting of a hollow "slow" plastic scintillator (60 cm long), a solid "fast" plastic scintillator (20 cm) and a BGO (bismuth germanate oxide, $Bi_4Ge_3O_{12}$) crystal (4 cm). 31
2.3 Output from the charge-sensitive amplifier (shown with a negative polarity). The rise time is shorter for a signal from the fast plastic scintillator than for one from the slow scintillator or BGO crystal. 32
2.4 Computer-generated top view of a 61-unit detector array. The PDCs (purple) are surrounded by a segmented side anti-coincidence shield (green). 32
2.5 The detection method of polarization. Left: Top view of the detector, polarization vector and distribution of scattered photon make perpendicular direction. Right: Cross section of the detector, tracking both of scattering and absorption position of X-rays. There are other background signals shown together. 33
2.6 A photograph of the PoGO prototype mounted on the rotation stage attached to the experiment table. 34

3.1 A photograph of the ground calibration with ^{241}Am and PoGOLite flight detector. 36
3.2 Cartoons of the ground calibration setup. Upper: Top view. Lower: Cross section. 37
3.3 Photograph and cartoon of scattering piece. Left: 2012, Right: 2013. 38
3.4 Definition of the Ring0-4, PDC number, PDC name of the detector. Left: Position of the scattering piece from the center to the Ring4 to irradiate every ring of the detector. Right: Definition of PDC number (0-60) and name. 38
3.5 The definition of some event selections of 2-hit events. There are three parameters to define one event selection, irradiation site, scattering site and absorption site. 40
3.6 Example of azimuth scattering angle reconstruction, and example of how two events with two different angles are reconstructed the same angle. In order to take into account this effect the azimuth angle distribution can be smeared out. [2] 42
3.7 Comparison between with Randomization and without Randomization data: the distribution of the with Randomization data (green histogram) are fitted with the (green) modulation curve. The without Randomization data (red histogram) are fitted with the modulation (red) curve. The fit of the with Randomization data gives a modulation factor of 20.3% ± 0.7% with 178.7 ± 1.8 polarization angle. The fit of the without Randomization data gives a modulation factor of 50.3% ± 0.6% with 135.2 ± 0.3 polarization angle. [2] . 43
3.8 The spectrum of ^{241}Am measured by the central PDC, with irradiating gamma-ray at the central PDC. 44

3.9 The setup of "new" background compared with (1): Normal polarized irradiation, (2): The center PDC is covered with a 2-mm thick lead sheet, and (3): The lead block of scatter holder is rotated by 90 degree, and the ^{241}Am source is blocked. 45
3.10 The distribution of the interaction site among 61 PDCs in 2012.. Black: Center irradiating polarized gamma-ray with 90/270 polarization angle for 1440 minutes. Red: Center irradiating polarized gamma-ray with 0/180 polarization angle for 600 minutes. Green: "New" background with lead sheet for 250 minutes (Fig. 3.9(2)). Blue: "New" background with lead block for 250 minutes (Fig. 3.9(3)). Magenta: Room background for 200 minutes. . . 46
3.11 The distribution of the interaction site among 61 PDCs in 2012. Green: After subtracting "new" background from Center irradiating polarized gamma-ray with 90/270 polarization angle for 1440 minutes. Magenta: Room background for 200 minutes. 47
3.12 The same as figure 3.11but for the comparison between different scatter pieces and with out the scatter piece. Black: 2012 Center irradiating polarized gamma-ray with 90/270 polarization angle for 1440 minutes after subtracting "new" background of 2012. Red: 2012 Center irradiating non-polarized (without the scatter piece) gamma-ray for 30 minutes. Green: 2013 Center irradiating polarized gamma-ray with 90/270 polarization angle for 750 minutes after subtracting "new" background of 2013. Blue: 2013 Center irradiating non-polarized (without the scatter piece) gamma-ray for 30 minutes. 48
3.13 Modulation curves with irradiating polarized/non-polarized gamma-ray at the Center PDC. The event selection is "All-2hit" event. Upper left: Polarization angle is 90/270 degree without Randomization. Upper right: Polarization angle is 90/270 degree with Randomization. Upper middle left: Polarization angle is 0/180 degree without Randomization. Upper middle right: Polarization angle is 0/180 degree with Randomization. Lower middle left: Non-polarized gamma-ray without Randomization. Lower middle right: Non-polarized gamma-ray with Randomization. Lower left: "New" background without Randomization. Lower right: New" background with Randomization. 50
3.14 The same as those is figure 3.13but for the event selection of "CenterCentral" event. . . 51
3.15 Comparison between ground calibration and Geant4 simulation of the distribution of the interaction site among 61 PDCs. Red: The ground calibration, irradiating non-polarized gamma-ray at Center PDC in 2013. Blue: The Geant4 simulation with the same setup for as ground calibration. 52
3.16 The coordinate of the detector 53
3.17 Comparison the modulation curves between the ground calibration (left) and the Geant4 simulation (right). 57
3.18 The distribution of the interaction site among 61 PDCs with raising up the threshold of the scattering energy from 0 to 60 ADC channel, corresponding from 0 to 4.95 keV. Left: The raw data. Right: The normalized at the central PDC. 58

3.19 2-D histogram and the projections (i.e., the energy spectra) with the threshold 0 and 60 ADC channel. The data are irradiating non-polarized gamma-ray at Center PDC. Scattering site is one PDC in Ring1 and absorption site is any PDC with threshold 0 ADC channel and 60 ADC channel. Upper left: Scattering site is Jiro with threshold of 0 ADC channel. Upper right: Scattering site is Jiro with threshold of 60 ADC channel. Lower left: Scattering site is Hicks with threshold of 0 ADC channel. Lower right: Scattering site is Hikcs with threshold of 60 ADC channel. 59
3.20 The same as figure 3.19but for the two selections: (1) the scattering site is Barret (Center) and absorption site is Jiro (Ring1), and (2) the scattering site is Barret (Center) and absorption site is Hicks (Ring1). 60

4.1 The trajectory of PoGOLite after the launch from Esrange. The tendency for the balloon to follow a Northerly track is seen in the days prior to termination. The launch took place from Esrange on 12th July at 0818 UT and the gondola landed in Siberia on July 25th at 0015 UT. In the yellow and red circles, E-Link communications are available. 62
4.2 The altitude of the PoGOLite balloon. From the launch to the end of E-Link region. . . . 63
4.3 An example of the number of hits in different units of the detector during the flight. The exposure time is 300 sec. 64
4.4 The count rate per one SAS unit . Upper: The plot as a function of time (MJD). Lower: The plot as a function of altitude. 65
4.5 The count rate per PDC. Upper: The plot as a function of time (MJD). Lower: The plot as a function of altitude. 66
4.6 The 2-hit count rate per PDC for scattering site. Upper: The plot as a function of time (MJD). Lower: The plot as a function of altitude. 68
4.7 The 2-hit count rate per PDC for absorption site. Upper: The plot as a function of time (MJD). Lower: The plot as a function of altitude. 69
4.8 The LiCAF count rate. Upper: The plot as a function of time (MJD). Lower: The plot as a function of altitude. 70
4.9 Left: An example of "Fast" and "slow" outputs of detector cell of LiCAF. Right: Projection of the left figure after selecting only LiCAF events and fitted with Gauss function. 71
4.10 Event rates of LiCAF and BGO in the neutron detector. Blue: Total, Green: Events of BGO crystal, Red: Events of LiCAF region, Magenta: Events in the Gauss function. Upper: The plot as a function of time (MJD). Lower: The plot as a function of altitude. 72

LIST of TABLE

1.1 The polarization measurements of the Crab nebula observed by INTEGRAL/IBIS in 200–800 keV . . . 20
1.2 Past measurements of Crab nebula . . . 21
1.3 Polarization measurements of Cyg X-1 observed by OSO-8 . . . 23
1.4 Past measurements of Cyg X-1 . . . 28

3.1 The list of ground calibration measurements . . . 39
3.2 The list of parameters of the modulation curves using Center irradiating data with "All-2hit event" . . . 49
3.3 The list of parameters of the modulation curves using Center irradiating data with "CenterCentral" event . . . 49
3.4 The positions of the scatter piece (x, y) mm . . . 53
3.5 The list of parameters of the modulation curves of the ground calibration and the Geant4 simulation . . . 54
3.6 Entry ratios of each Ring with raising up the threshold of the scattering energy from 0 to 60 ADC channel, corresponding from 0 to 4.95 keV. . . . 58

Chap.1 Introduction

1.1 X-ray and gamma-ray polarimetry

Astrophysical phenomena can be observed with electromagnetic radiations by imaging, spectroscopy, timing analysis, and polarimetry. Since the X-ray observation began 50 years ago, many observatories have provided us the data for imaging, spectroscopy, and timing analyses. On the other hand, polarization measurements of X-rays and gamma-rays have been technically difficult and no sensitive observations have been performed. Nevertheless, polarized X-rays and gamma-rays are expected to be emitted from a wide variety of astronomical sources, including pulsars, X-ray binary systems, strongly magnetized neutron stars, collimated outflows from active galactic nuclei and gamma-ray bursts. Therefore, polarimetric studies of these sources are expected to provide important new insight into the physics of such high energetic objects. In particular, it is important to understand the acceleration site and magnetic field structure of pulsars and their ambient wide nebulae by identifying the emission mechanisms with polarimetry.

1.2 Measurement techniques

Measurements of polarization of X-rays and gamma-rays depend on the physical processes of photons with materials, and there are four types of polarimetry. In the soft X-ray band, Bragg refraction and photoelectric effect are utilized. Compton scattering dominates in an intermediate energy region of several tens keV to MeV, and the pair production process takes over in the highest energy region above 10 MeV. Because these processes dominate in different energy regions (Fig. 1.1), polarimetric instruments should be designed to utilize an appropriate process in the target energy band.

1.2.1 Bragg reflection

In the Bragg reflection, an incident photon is refracted by a mosaic crystal, and the angular dependence of the integrated reflectivity is given by equation (1.1).

$$\Delta\theta = \frac{N^2\lambda^3F^2r_0^2}{2\mu}\left[\frac{1}{sin\ 2\theta} - \frac{sin\ 2\theta}{2}(1 + P\ cos\ 2\phi)\right] \tag{1.1}$$

Here λ is the wavelength of Bragg refraction, μ is the absorption coefficient, N is the number of scattering cells per unit volume, F is the crystal structure factor, that is, the effective number of scattering electrons per cell, r_0 is the classical electron radius, P is the polarization of the incident radiation, θ is the Bragg

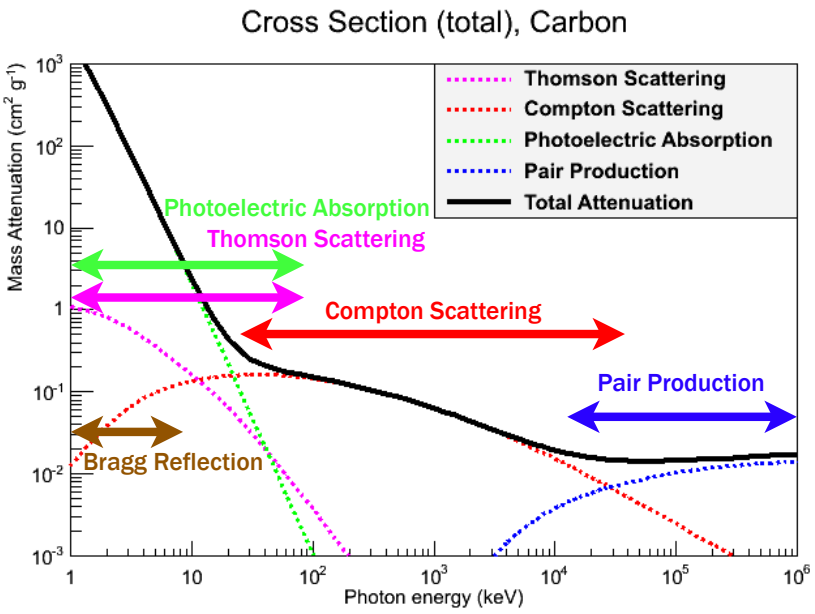

Figure. 1.1: Mass attenuation coefficient (cm^2/g) for photon interactions in carbon, adopted from NIST.

angle, ϕ is the azimuth angle between the plane of incidence and the plane formed by the incident photon direction and polarization vectors.

In the case of a 45 degree Bragg angle ($\theta = 45$ degree), equation (1.1) becomes equation (1.2).

$$\Delta\theta = \frac{N^2\lambda^3F^2r_0^2}{4\mu}(1 - P\ cos\ 2\phi) \tag{1.2}$$

Obviously operating at an angle 45 degree acts as a perfect polarization analyzer over the energy bandwidth characteristic of the Bragg reflection, and also in the equation (1.2), $\Delta\theta$ is the largest when the ϕ is 90 degree. Therefore refracted X-ray tends to have perpendicular angle with the crystal [6].

Rotating the instrument with uniform angular velocity, we can know the modulation of the celestial targets, and modulation factor using Bragg reflection technique is quite high (e.g. modulation factor of the OSO-8 satellite is 0.93 [7]).

To reduce background, the detector should be small, and the parabolic panels are formed from a mosaic of small flat crystals (Fig. 1.2) [6].

1.2.2 Photoelectric effect

In the photoelectric effect, an incident photon interacts with an atom through the electromagnetic process, and disappear with an ejection of a bound electron having a kinetic energy by equation (1.3).

$$E_{k,e^-} = h\nu - E_b \tag{1.3}$$

where h is Planck's constant, ν is the frequency of the incident radiation and E_b is the binding energy of the electron in question (1.3).

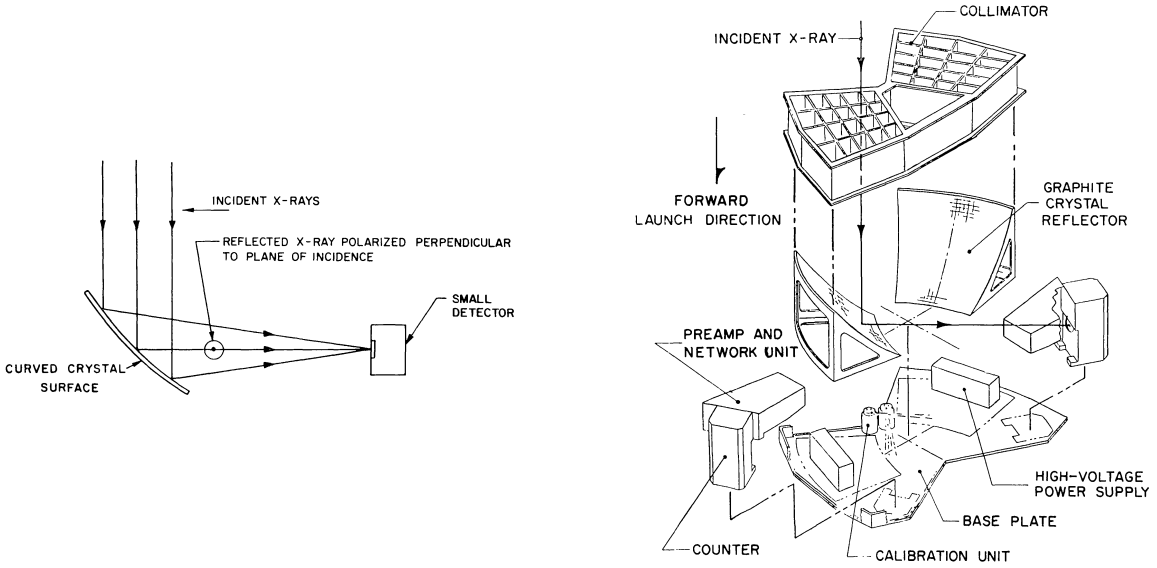

Figure. 1.2: Left: Concept diagram of focusing Bragg-crystal polarimeters. Right: Exploded view of OSO-1 polarimeter assembly.

$$\frac{d\sigma}{d\Omega} = r_0^2 Z^5 \alpha^4 \left(\frac{m_e c^2}{h\nu}\right)^{7/2} \left[\frac{4\sqrt{2} sin^2\theta cos^2\phi}{(1-\beta cos\theta)^4}\right] \tag{1.4}$$

where r_0 is the classical electron radius, Z is the atomic number of the absorbing material, α is the fine-structure constant, m_e is the mass of the electron, c is the speed of light, θ is the polar emission angle of the electron, ϕ is the azimuthal angle of emission from the polarization plane and $\beta = v/c$ with v being the final velocity of the emitted electron. When $\phi = 0$ or 180, $\frac{d\sigma}{d\Omega}$ in equation (1.4) becomes largest, and the direction of emission is peaked around the same direction of polarization angle (Fig.1.3 [8]).

Therefore, by measuring the azimuthal distribution of emitted electrons, the polarization of the incident radiation can be measured.

1.2.3 Compton scattering

In the Compton scattering, an incident photon is scattered off an atomic electron, and gives some of the energy to the electron. The scattering angle θ of the incident photon is defined as figure 1.4.

The energy of the scattered photon is given by equation (1.5).

$$E_1 = \frac{mc^2 E_0}{E_0(1 - cos\ \theta) + mc^2} \tag{1.5}$$

where $E_0 = h\nu$ is the energy of the incident photon (Fig. 1.4).

The Compton process follows the Klein-Nishina formula [9] [5], which gives the differential cross-section for a photon to scatter toward the direction of a polar angle θ relative to the direction of incidence and azimuthal angle ϕ relative to the polarization vector which is written in equation (1.6).

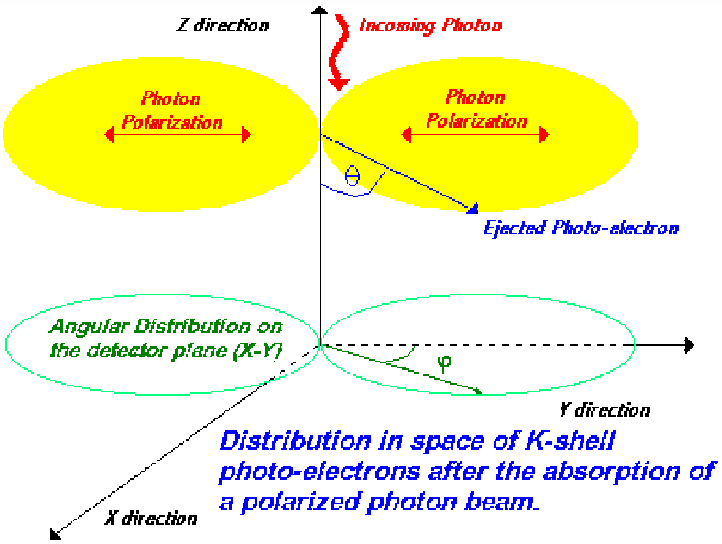

Figure. 1.3: Distribution in space of K-shell photo-electrons after the absorption of a polarized photo beam.[8]

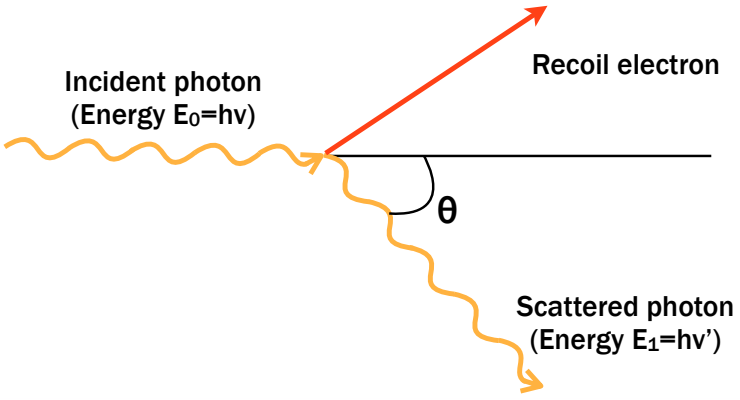

Figure. 1.4: Geometry of the Compton scattering process.

$$\frac{d\sigma}{d\Omega} = \frac{1}{2} r_e^2 \frac{k^2}{k_0^2} \left(\frac{k}{k_0} + \frac{k_0}{k} - 2\ sin^2\theta cos^2\phi \right) \tag{1.6}$$

where k_0 and k are the momenta of the incident and scattered photon, respectively (Fig. 1.5).

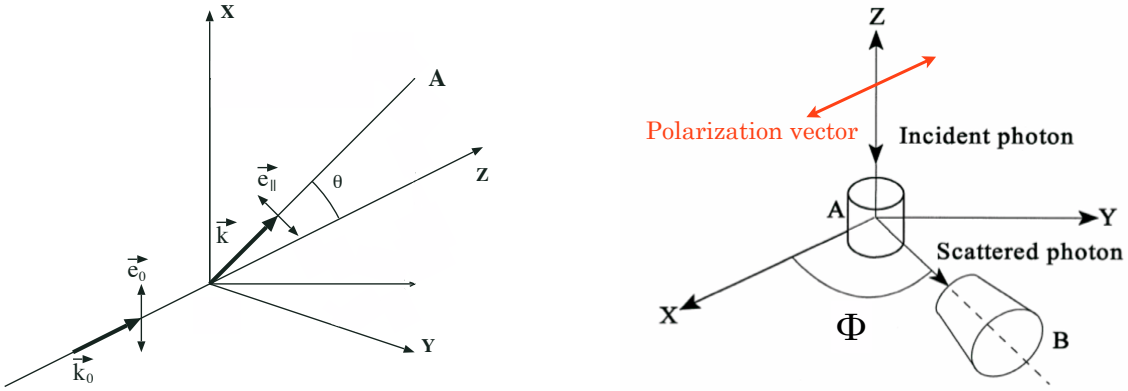

Figure. 1.5: Three-dimensional geometry of the Compton scattering process. Left: The incident photon has momentum k_0 and polarization $\vec{e_0}$ along the z-axis and x-axis, respectively. It scatter toward the direction of a polar angle θ relative to the z-axis, whereafter it retains momentum $\vec{k_0}$. Right: ϕ is the azimuthal angle of the scattered photon with respect to the polarization vector of the incident photon.

When $\phi = 90$ or 270, $\frac{d\sigma}{d\Omega}$ in equation (1.6) becomes largest, and polarized photon tends to scatter toward the perpendicular direction respect to polarization vector.

1.2.4 Pair production

In the pair production process, an incident photon interact with the Coulomb field of an atom and is transformed into an electron-positron pair [10] [11](Fig. 1.6).

The incident photon must have an energy exceeding the $2m_ec^2 = 1022$ keV for the pair production, and a close proximity to an atom is needed for the conservation of momentum. The process tends to be co-planar ($\phi = 180$ degree) i.e. the electron-positron pair is mostly in the same plane as the momentum of the incident photon (vector k in Fig. 1.6). When Ψ is defined as an angle between the polarization vector of the incident photon and the plane of the produced electron-positron pair, the differential cross-section of this process is given in equation (1.7) [10].

$$\frac{d\sigma}{d\Psi} = A(1 - \lambda cos^2\Psi) \tag{1.7}$$

where an asymmetric factor which represents a ratio of A ≈ 0.8 (ratio between number of pairs produced in the plane of polarization and number of pairs produced in the plane perpendicular to the polarization, i.e. 80% events of all are produced in that plane) and $\lambda \approx 0.2$ is the degree of asymmetry in the distribution and is approximately constant at high energy. Therefore, since the electron-positron pair plane has a higher probability to be oriented perpendicular to the polarization vector ($\psi = 90$ degree), the

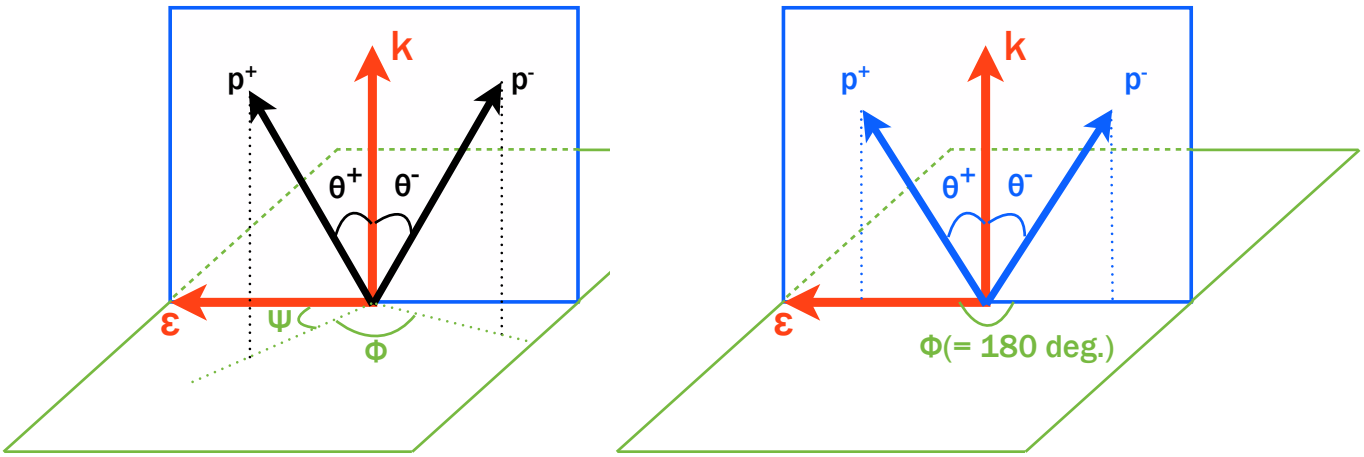

Figure. 1.6: The geometry of the pair production process [10]. Left: This is a general case for pair production. Vectors k, p^+ and p^- indicate the momenta of the incident photon, positron and electron, respectively. Angles θ^+ and θ^- are the polar angles of the positron and electron respect to the direction of incident photon (vector k). The polarization direction is indicated by ε, and Ψ is the angle between this direction and the projection of p^+ onto the plane perpendicular to the direction of the incident photon. Finally, ϕ is the angle between the projections of p^+ and p^- on this plane. Right: This is a special case ($\Phi = 180$ degree), but it is the most common ($\approx$80 %) in the co-planar case, i.e. the electron-positron pair is in the same plane as the incident photon.

process will be modulated by the polarization of the incident radiation and pair production can therefore be used for polarimetry [10].

1.2.5 Modulation factor

As described above, momentum directions of electrons or positrons emitted by polarized X-rays or gamma-rays are not uniform and thus modulated (anisotropic) (Fig. 1.7).

The modulation factor (MF) is an indicator characterizing a performance of X-ray and gamma-ray polarimeters and defined as a ratio between the amplitude A and the mean value B of a modulation curve. That is, MF is given in the equation (1.8).

$$MF = \frac{A}{B} = \frac{N_{max} - N_{min}}{N_{max} + N_{min}} \tag{1.8}$$

where N_{max} and N_{min} are the maximum and minimum numbers of events of the angular distribution (Fig. 1.7).

Polarized radiation is characterized by two parameters: polarization degree and polarization angle. Polarization degree is a fraction of the radiation with polarization aligned in a certain direction. Polarization angle is a rotation between a chosen frame of reference and the polarization direction. These parameters are able to be deduced from the modulation curves. The intrinsic polarization degree of P

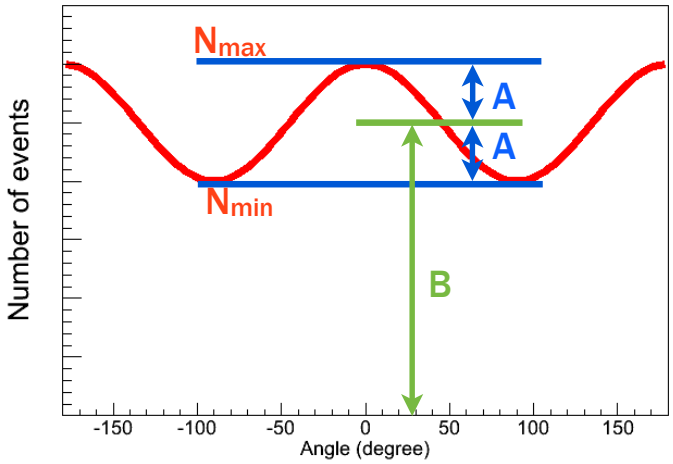

Figure. 1.7: An example of polarization-induced modulation. The the horizontal axis is azimuthal angle. A is an Amplitude of this curve, and B is a mean value of a fitted sinusoidal modulation curve.

from the target is written in equation (1.9)

$$P = \frac{M}{M_{100}} \tag{1.9}$$

where M is the observed modulation and M_{100} is the modulation for observing a 100% polarized beam. To obtain M_{100}, there is a need to simulate and/or measure a beam with a known polarization degree. The intrinsic modulation from the celestial object is affected by the efficiency of the instrument. If there is a perfect instrument, the M_{100} becomes 1, and the observing modulation is equal to the intrinsic modulation. Worse performances of the instruments, i.e. low M_{100}, will lead to a large uncertainty of polarization measurement.

1.2.6 Minimum Detectable Polarization

Another indicator of performance of X-ray and gamma-ray polarimeters, which is called as MDP (Minimum Detectable Polarization), written in equation (1.10)

$$MDP = \frac{4.29}{M \times R_S}\sqrt{\frac{R_S + R_B}{T}} \tag{1.10}$$

where M is modulation factor, R_S is a signal rate, R_B is a background rate and T is exposure time. This represents the minimum polarization degree measured by the instrument. A large M, a large R_S, a small R_B, and a large T makes the MDP small. For a given source, a large R_S corresponds to a large effective area of the instrument. Therefore, in other words, instruments with a larger modulation factor, a larger effective area and a lower background rate can be a better polarimetry.

1.3 Target objects

1.3.1 Crab nebula

outline

The Crab nebula is a remnant of the historical supernova in 1054 A.D., located around 2 kpc away from the Earth. The supernova was recorded in Meigetsuki, which was a diary of a noble in Japan and remains now, and was visible during the daytime for three weeks, and was visible at night for 22 months. This celestial object is named "Crab nebula" after the characteristic filament structure in optical, and has been studied intensively in all wavelength from radio to gamma-ray since the early stage of astronomy (Fig.1.8). The Crab consists of a pulsar, a synchrotron nebula, a bright expanding shell of thermal gas [12]. We can also see a highly collimated bipolar outflow (jet), which is aligned to the spin axis of the pulsar, a circumstellar torus in X-ray, and high energy emission is brightest near the center of the nebula (Fig. 1.8).

Figure. 1.8: Color composite of the Crab nebula, blue: Chandra X-ray image, green: Hubble Space Telescope optical image, red: Very Large Array radio image.

The Crab pulsar considered as a neutron star with a radius 10 km, a mass 1.4 $M_{\odot}$, a rotation period P = 33 ms, $\dot{P} = 4.21\times\ 10^{-13}$, magnetic field B $\approx 10^{12}$ G, spin-down luminosity $L_s \approx 5 \times 10^{38}$ erg/s. The strong magnetic field and short rotation period produce a relativistic outflow of electron-positron pairs which is called pulsar wind. This ultrarelativistic pulsar wind is confined by the thermal ejecta from the explosion into which is expanding thermal ejecta of the supernova. There is a termination shock between the wind and the synchrotron nebula under the momentum balance, which corresponds to the inner ring (Fig. 1.9 left), and was reported to locate about 3×10^{17} cm from the pulsar. It is considered that pulsar

wind and possibly other particles are accelerated to as high energy as $\sim 10^{16}$ eV at the termination shock. High energy charged particles interact with magnetic field in the nebula ($\sim$ a few mG), and emit synchrotron radiation (Fig. 1.9 right). X-ray emission becomes softer toward the outer region owing to adiabatic and radiative losses. At the edge of the nebula, there are only low-energy radio-emitting electrons. The spectrum of X-ray and gamma-ray below 1 GeV for the Crab nebula is well described by synchrotron emission, and the inverse Compton scattering dominates above 1 GeV.

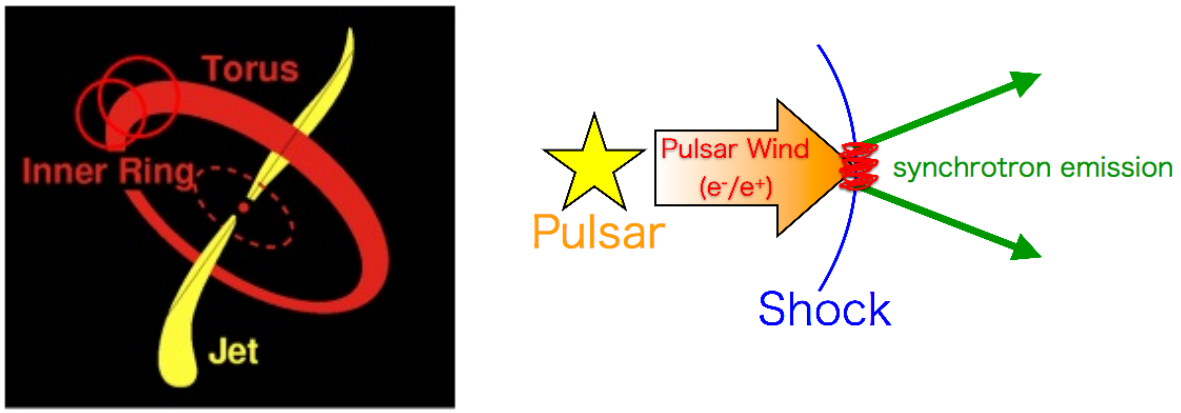

Figure. 1.9: Cartoons of the Crab. Left: a simple X-ray structure of the Crab pulsar, inner ring (termination shock), torus and jets [13]. Right: conceptual diagram of pulsar wind nebula, pulsar wind (electron-positron pair) is emitted by pulsar, are accelerated to high energy at the termination shock, and emit synchrotron radiation.

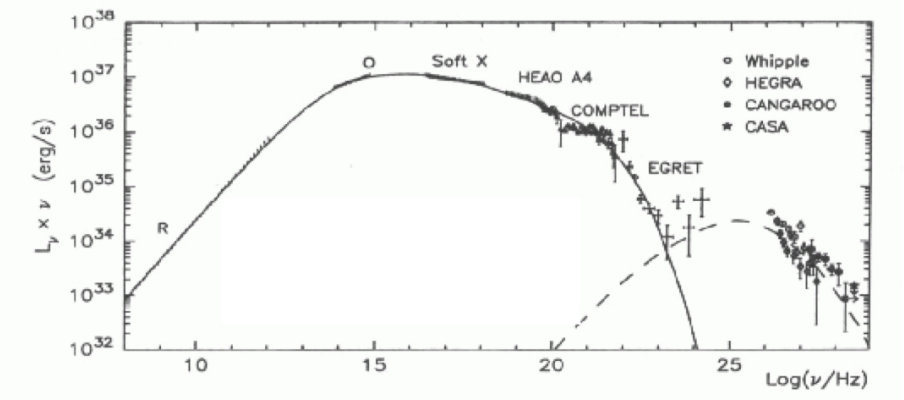

Figure. 1.10: The broad spectrum of the Crab nebula [14]. Below 1 GeV radiation is well described by synchrotron emission and above that due to inverse Compton scattering.

Past polarization measurements of Crab nebula

There is only a few polarization measurements of the Crab nebula in the X-ray and gamma-ray band, and they were performed by OSO-8 and INTEGRAL satellites.

Measurement by OSO-8 The OSO-8 satellite carried an X-ray polarimeter consisting of a panel of mosaic graphite crystals, which were utilized for Bragg reflection. The modulation factor achieved 0.93 and was able to measure X-ray linear polarization [15].

The polarization degree of Crab nebula observed by OSO-8 is 19.19% ± 0.97% with 156.36 ± 1.44 degree polarization angle in 2.6 keV, and 19.50% ± 2.77% polarization degree with 152.59 ± 4.04 polarization angle in 5.2 keV, these errors were in the 67% confidence contours, and these results agree with optical polarization measurement (Fig. 1.11) [15].

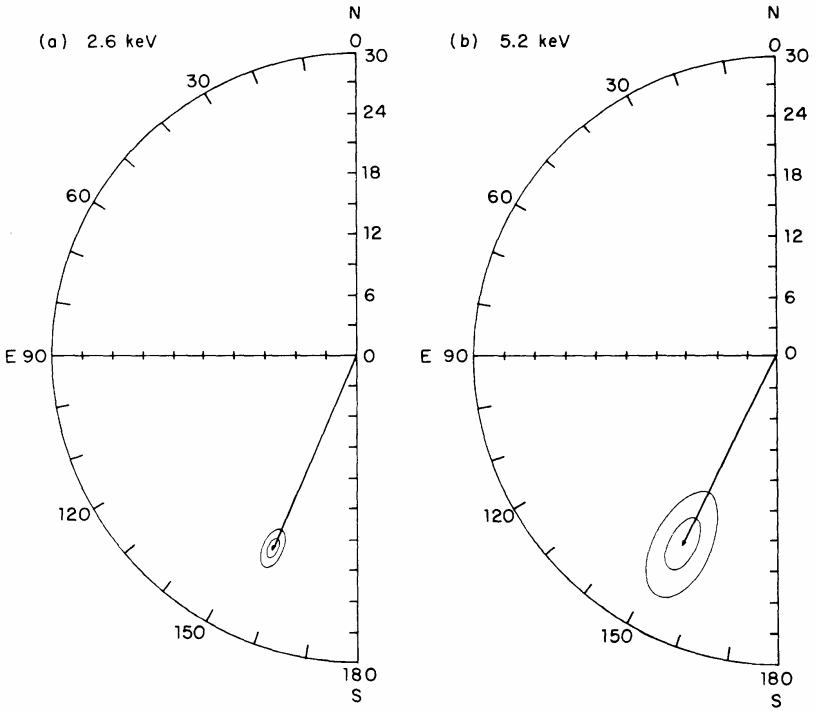

Figure. 1.11: The polarization vectors for the Crab Nebula at (a) 2.6 keV and (b) 5.2 keV. Surrounding vectors in the order of increasing size correspond to the 67% and 99% confidence contours [15].

Observation by INTEGRAL/SPI The SPI (spectrometer onboard INTEGRAL; International Gamma-Ray Astrophysics Laboratory) has a capability of polarization measurement by using Compton scattering, and has a modulation factor of 17–25% in 150–600 keV band (Fig. 1.12) [17].

Polarization measurement of the Crab nebula was performed with the data from February 2003 to April 2006, where only the events during the off-pulse fraction of the pulsar cycle were selected (Fig. 1.13 left).

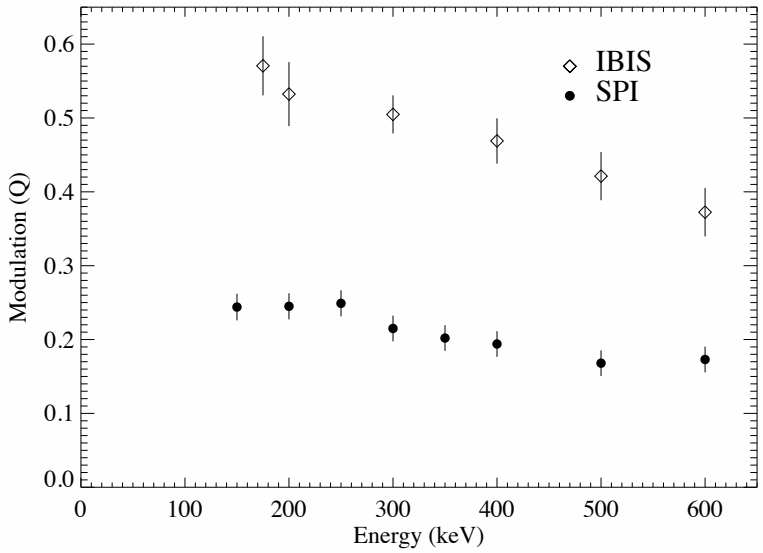

Figure. 1.12: The energy dependency of modulation factors for SPI and IBIS onboard INTEGRAL satellite [17].

The 46% ± 10% polarization degree with the polarization angle of 123 ± 11 degree was observed, which is closely aligned with the pulsar spin axis (124 ± 0.1 degree) (Fig. 1.13 right), the errors are dominated by non statistical effects. This result, the alignment of the polarization angle along the jet axis, suggests an orthogonal magnetic field configuration toward the jet axis if the soft gamma-ray emission was synchrotron emission. The observed polarization degree is quite high but lower than the maximum limit of polarization degree of the synchrotron radiation of ∼75%. [16]

Observation by INTEGRAL/IBIS The IBIS (imager on INTEGRAL) is also using Compton scattering for polarimetry and has the modulation factor 30% ± 2% for a Crab-like $E^{-2.2}$ spectrum between 200 and 800 keV [18]. There is also a report about the polarization of the Crab nebula by IBIS.

The results are shown with respect to each pulsar phase (Fig. 1.13 left), and the polarization degrees of off-pulse phase and "off-phase and bridge" are quite high (>72%) with the polarization angle along the jet axis (Table 1.1, Fig. 1.14). This result seems marginally consistent with INTEGARL/SPI result (polarization degree ∼46%) and close to the maximum physical limit. However, the lower limit of the INTEGRAL/IBIS results is computed for any value of the polarization angle. Then, the SPI and IBIS results are consistent at the 95% level, if the polarization angle are fixed at the SPI measured best-fit value. This results suggests that the off-pulse polarized emission recorded above 200 keV can come from the striped wind, jets, and/or the equatorial wind near the bright knot. The MHD models predict that polarization is strongest at the pulsar, in the knot, and along the jets and that it should be mostly parallel to the rotation axis [18].

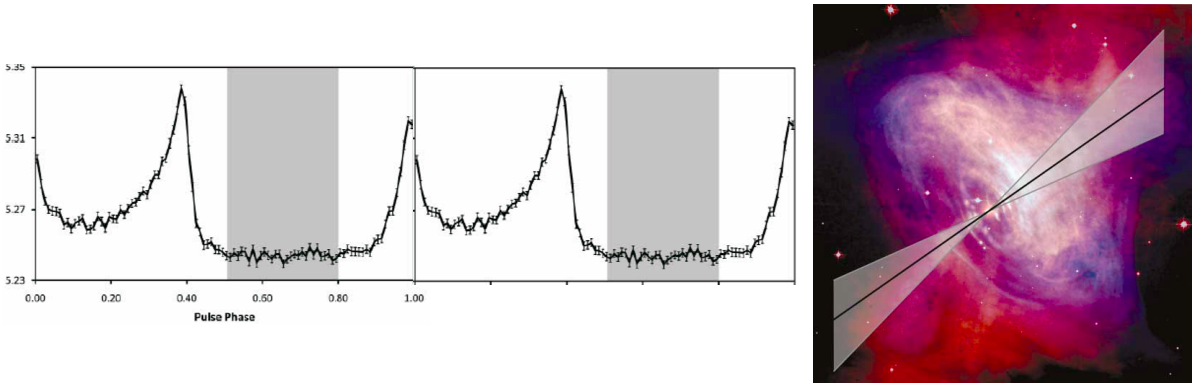

Figure. 1.13: Left: The light curve of the Crab pulsar. There are two pulse phases (0.88 $<\phi<$ 0.14 and 0.25 $<\phi<$ 0.52), off-pulse phase (0.52 $<\phi<$0.88), and last phase called as "Bridge" phase (0.14 $<\phi<$ 0.25). The data for polarization analysis for INTEGRAL/SPI is selected from within the phase interval from 0.5 to 0.8 of the pulsar period (shaded area) in 100–1000 keV. Right: The composite image of the Crab, blue: Chandra X-ray image, green: Hubble Space Telescope optical image, and the gamma-ray polarization vector is superimposed with the limits on the direction of the vector (shaded area). The direction of the polarization vector is along with the jet.

A brief summary of the past measurements of the Crab nebula are shown in table 1.2.

Table. 1.1: The polarization measurements of the Crab nebula observed by INTEGRAL/IBIS in 200–800 keV

Phase Interval of Crab Pulsar	Polarization angle (degree)	Polarization degree (%)
On-pulse (0.88 $<\phi<$ 0.14 and 0.25 $<\phi<$ 0.52)	70 ± 20	42^{+30}_{-16}
Off-pulse (0.52 $<\phi<$0.88)	120.6 ± 8.5	>72
Off-pulse and Bridge (0.52 $<\phi<$ 0.88 and 0.14 $<\phi<$ 0.25)	122.0 ± 7.7	>88
All	100 ± 11	47^{+19}_{-13}

1.3.2 Cyg X-1

outline

Cyg X-1 is one of the most famous black hole (BH) X-ray binaries in our Galaxy, located at 2.1 kpc away from the Earth, forming a binary system with a high-mass blue O star. It has been widely observed with many telescopes over the whole electromagnetic band, and it is well known that Cyg X-1 exhibits a transition between low/hard state and high/soft state in the X-ray band (Fig. 1.15). It radiates mainly in the X-ray and soft gamma-ray, and the X-ray emission is thought to be produced by accretion of the matter from the companion onto the BH [22]. Cyg X-1 is known to show a radio emision from the jet in the hard state, and the position angle of the jet orientations are around -20 or -25 degree from radio observations [23].

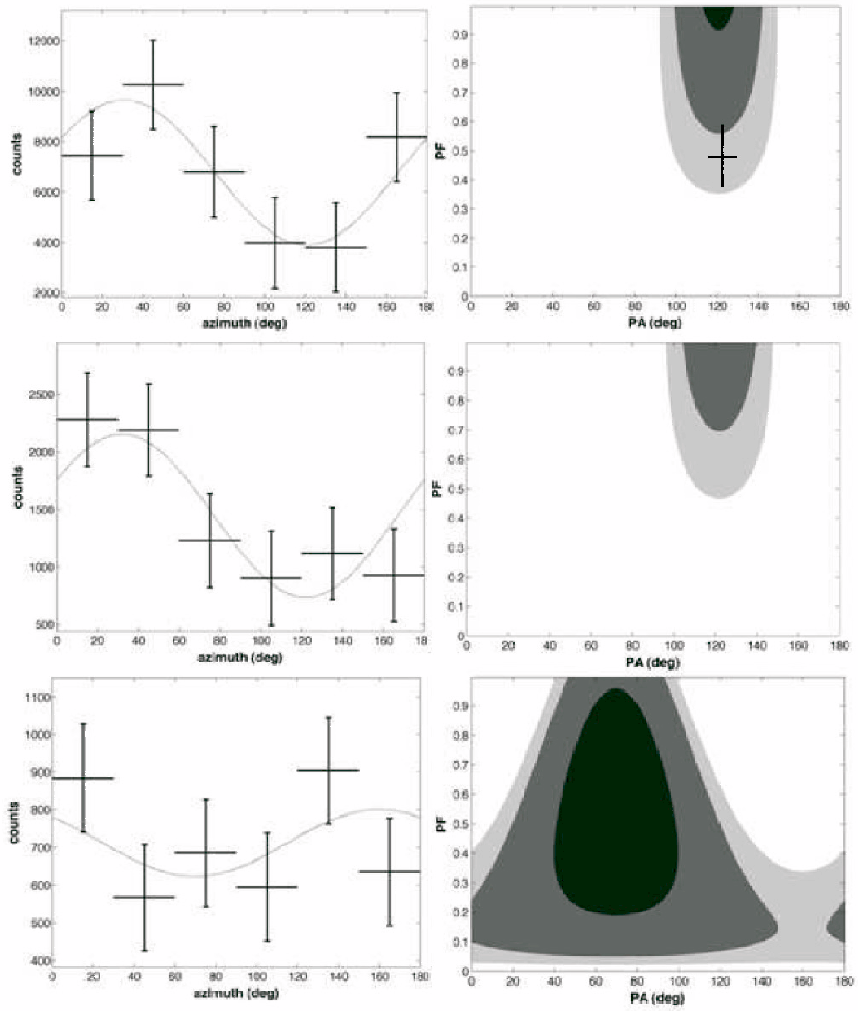

Figure. 1.14: The polarization of Crab nebula observed by INTEHRAL/IBIS. The polarization angle and polarization degree are measured for the Crab data between 200–800 keV, in the off-pulse (top), off-pulse and bridge (middle), and two-peak (bottom) phase intervals. The error bars for the profile are at 1σ. The 68%, 95%, and 99% confidence regions are shaded from dark to light gray. The SPI result [16] is indicated in the top figure by a cross [18].

Table. 1.2: Past measurements of Crab nebula

Satellite	OSO-8 (1976-78)		INTEGRAL(2002-)	
			SPI (Off-pulse phase)	IBIS (Off-pulse and Bridge phase)
Energy (keV)	2.6	5.2	100 – 1000	200 – 800
Polarization degree (%)	19.19 ± 0.97	19.50 ± 2.77	46 ± 10	>88
Polarization angle (degree)	156.36 ± 1.44	152.59 ± 4.04	123 ± 11	122.0 ± 7.7

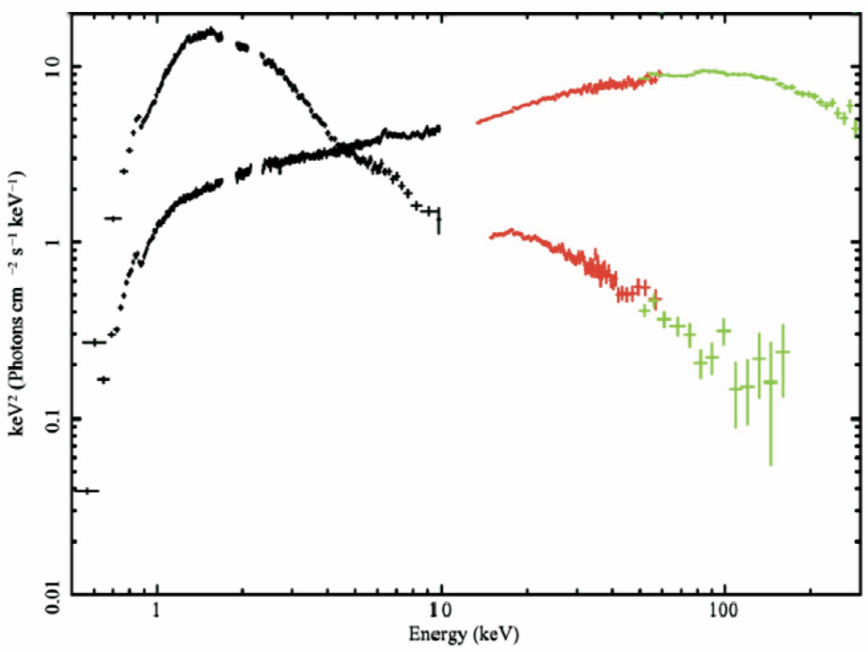

Figure. 1.15: The spectrum of Cyg X-1 observed by Suzaku satellite. Black: XIS (CCD), red: HXD-PIN, green: HXD-GSO. The spectrum in the high/soft state has a dominant soft emission below 10 keV while that in the low/hard state is dominated by higher energy component [19].

Past polarization measurement of Cyg X-1

The polarization modulation of Cyg X-1 also has been detected by only OSO-8 and INTEGRAL satellites.

Observation by OSO-8 OSO-8 observed Cyg X-1 three times in 1975, 1976 and 1977 (table 1.3). During the 1975 observation, Cyg X-1 was in the high/soft state, and in both 1976 and 1977, in the low/hard state. The averaged polarization degree and angle of these three measurements are 2.44% ± 1.07% and 162 ± 13 degree at 2.6 keV, and 5.3% ± 2.5% and 155 ± 14 degree at 5.2 keV.

These errors are in the 67% confidence level and contours at the 99% level are not well rescricted at a 99% level (Fig. 1.16) [20]. This result is consistent with a magnitude of the polarization from thermal disc emission, which is at most ∼10% [21].

Table. 1.3: Polarization measurements of Cyg X-1 observed by OSO-8

	Year	Observation Beginning – End (day: hour UT)	Polarization angle (degree)	Polarization degree (%)
2.6 keV	1975	312:00 – 314:21	174 ± 19	2.42 ± 1.47
	1976	305:23 – 313:02	162 ± 21	2.61 ± 1.74
	1977	305:16 – 314:05	163 ± 17	2.46 ± 1.49
	Average		162 ± 13	2.44 ± 1.07
5.2 keV	1975	312:00 – 314:21	105 ± 33	4.8 ± 4.4
	1976	305:23 – 313:02	146 ± 34	3.9 ± 3.6
	1977	305:16 – 314:05	162 ± 12	7.3 ± 2.0
	Average		155 ± 14	5.3 ± 2.5

Observation with INTEGRAL/IBIS The INTEGRAL/IBIS has observed two components in Cyg X-1 spectrum, a cutoff power-law in 20–400 keV and a power-law spectrum up to 2000 keV (Fig. 1.17). The observed polarization degree and angle were 67% ± 15% and 40 ± 15 degree, while the polarization in 250–400 keV could not be constrained with an upper limit of 20%.

This result of non-polarized lower energy part and highly polarized higher energy part, can be understood in terms of two emission mechanisms. The emission process radiating non-polarized photons would dominate in the lower energy band and the emission is cut off above 150 keV. This is explained by thermal Comptonization. The highly polarizated emission in the higher energy band shows a hard spectral shape up to 1000 keV, suggesting the synchrotron or inverse Compton emission from the jet already observed in the radio band, and the synchrotron process is the most probable way to produce such strongly polarized emission [22]. However, radio observations gave a polarization angle at 20–25 degree, which is different from the IBIS result by ∼60 degree. Therefore the results of INTAGRAL/IBIS are not totally understood [22].

Observation by INTEGRAL/SPI INTEGRAL/SPI also measured the polarization of Cyg X-1. The gamma-ray emission was detected in 22–2000 keV (Fig. 1.19). Events are classied into two categories, “standard (single) events“ and “multiple event“ when events are recorded in the detector. The “standard

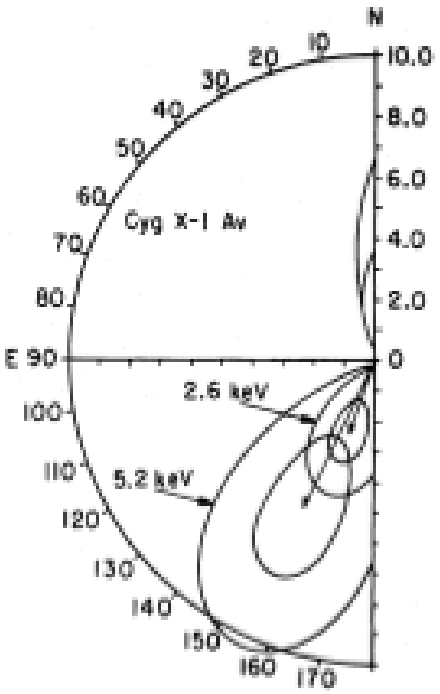

Figure. 1.16: The averaged polarization vectors for the Cyg X-1 at 2.6 keV and 5.2 keV [20].

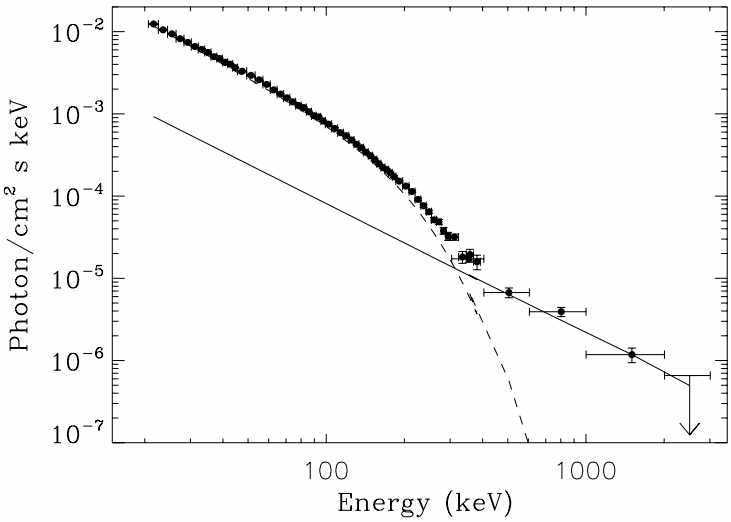

Figure. 1.17: The energy spectrum of Cyg X-1 observed by INREGARL/IBIS. The spectral shape of Cyg X-1 requires the presence of two components, a cutoff power-law in 20 – 400 keV and a power-law spectrum up to 2000 keV [22].

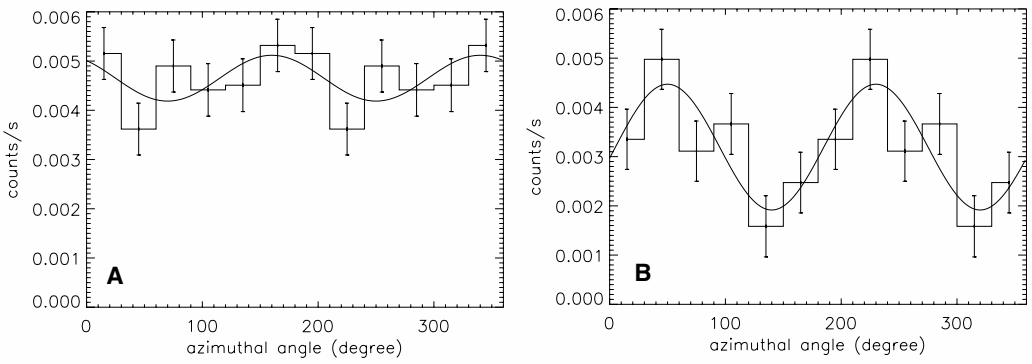

Figure. 1.18: The polarization of Cyg X-1 observed by INTEGRAL/IBIS. The polarization angle and polarization degree are measured in 250–400 keV (left), and in 400—2000 keV (right). These results show that upper limit of 20 % in 250–400 keV and 67% ± 15% polarization degree with 40 ± 15 degree polarization angle in 400–2000 keV. [22]

event“ deposits the energy within a single pixel, and “multiple event“ deposits energy within more than one pixel. The spectrum is fitted with two components model; a thermal Comptonization model for lower energy part, plus cut-off power-law model for high energy part. Because of limited significance, a photon index and a cut-off energy are poorly constrained to be ∼1.6 and ∼700 keV, respectively. The two components intersect around 240 keV, in agreement with a scheme where the polarized component dominates above this energy while the non-polarized one dominates below this energy [23].

INTEGRAL/SPI also reported that upper limit of 20% polarization in the low energy part (130–230 keV), and high polarization in the high energy part (230–850 keV) (Fig. 1.20, table. 1.4). There results suggest that Cyg X-1 has two components, as the INTEGRAL/IBIS result. It is also not consistent with radio observation because the direction of polarization angle measured by INTEGRAL/SPI is ∼40 degree, and ∼60 degree away from the radio jet direction [23]. Moreover, the polarization degree of 67% ± 30% is close to the maximum physical limit for the high linear polarization.

Here, I make a brief summary of the Past measurements of Cyg X-1 in table 1.4.

1.3.3 Short summary of past measurements

Only a few observations of polarization measurements have been performed in the X-ray and soft gamma-ray band, in spite that the polarization measurement is a powerful method to constrain the emission mechanisms and geometries of the celestial objects. In addition, the polarization measurement in the several tens keV band (hard X-ray band) has never been performed. Therefore, new observations in the 10–100 keV band and also above 100 keV band are needed for the Crab nebula and Cyg X-1. In both objects, the highly polarized X-rays and gamma-rays are expected to come from the jet, but this scenario is not yet conclusive.

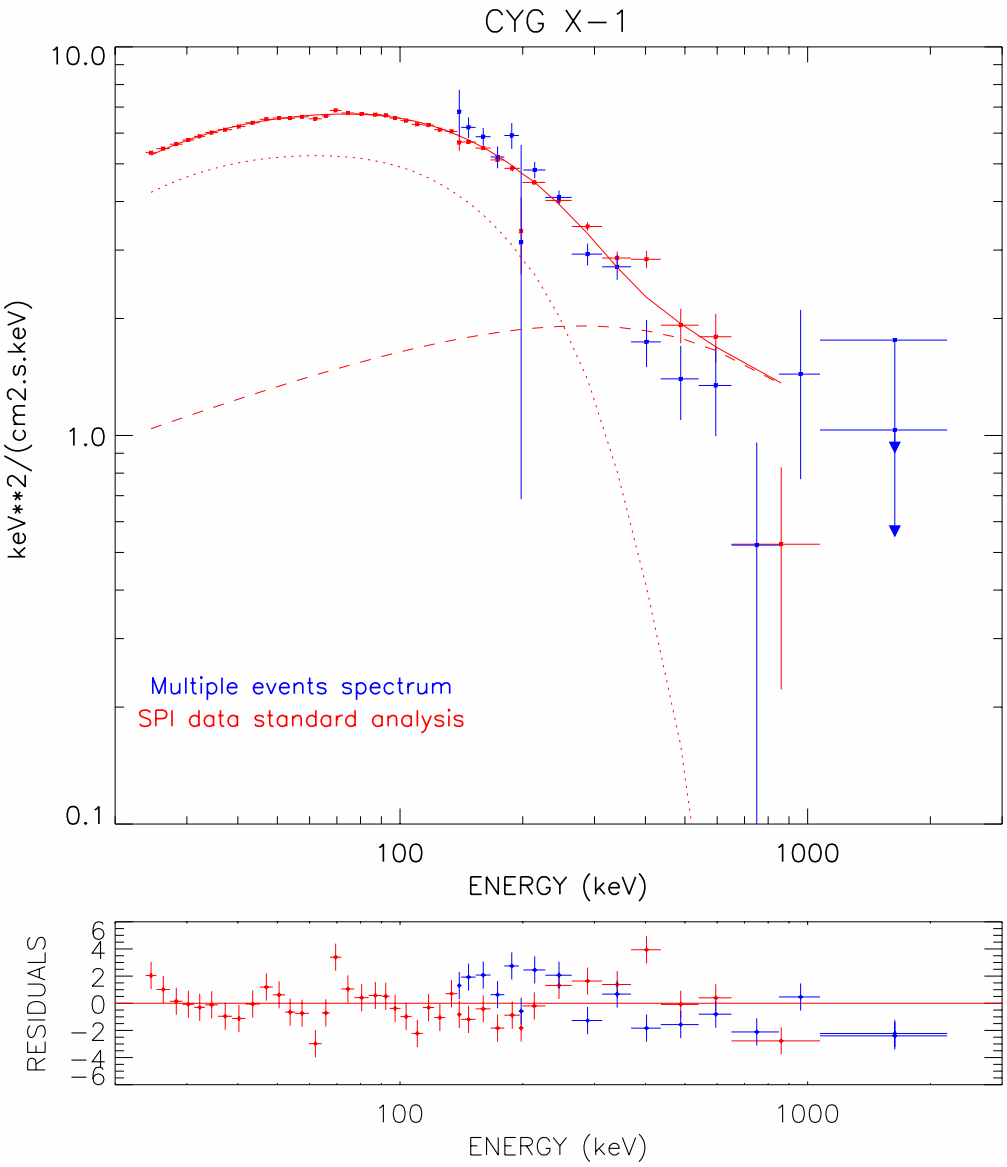

Figure. 1.19: The Cyg X-1 spectrum observed by INTEGRAL/SPI. Blue: "standard (single) events" in 22–2000 keV and "multiple event" in 130–2000 keV. The solid lines is the fit model composed of a thermal Comptonization plus a fixed cutoff power-law model (photon index = 1.6, E_{cut} = 700 keV; dashed line). 0.5% of systematic have been added to the data. [23]

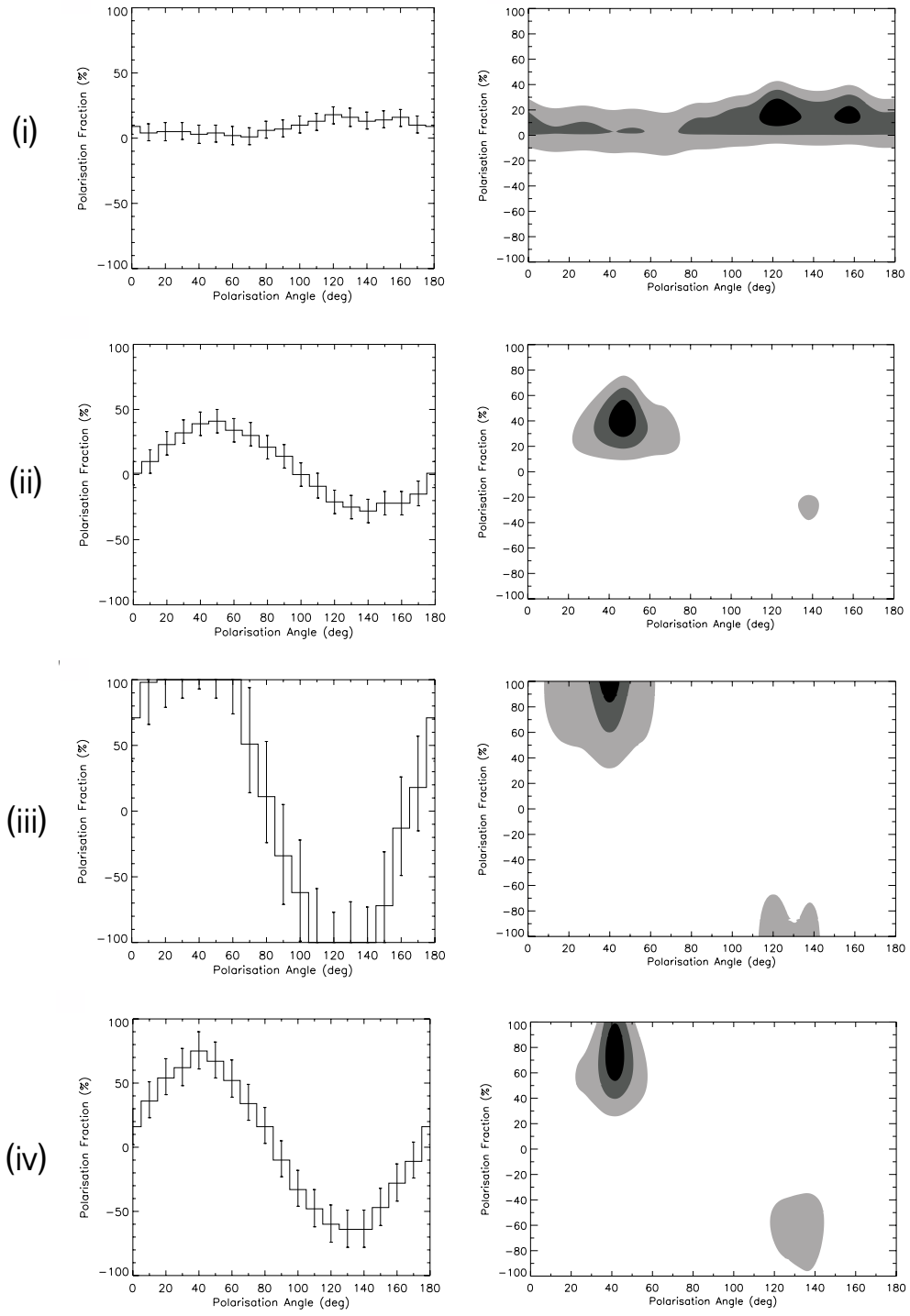

Figure. 1.20: The polarization of Cyg X-1 observed by INTEHRAL/SPI. Left columns are the polarization angle and polarization degree, and right columns are contours show that the confidence regions at 1σ, 2σ and 3σ, are shaded from dark to light gray. (i) to (iv) are in 130–230 keV, 230–370 keV, 370–850 keV, and 230–850 keV, respectively. [23]

Table. 1.4: Past measurements of Cyg X-1

	Energy (keV)	Instrument	Polarization angle (degree)	Polarization degree (%)
Radio			-20 $\sim$ -25	
Soft X-ray	2.6	OSO-8	2.44 $\pm$ 1.07	162 $\pm$ 13
	5.2	OSO-8	5.3 $\pm$ 2.5	155 $\pm$ 14
130 – 400 keV	130 – 230	INTEGRAL/SPI	<20	
	200 – 400	INTEGRAL/IBIS	<20	
230 – 2000 keV	230 – 370	INTEGRAL/SPI	41 $\pm$ 9	47 $\pm$ 4
	370 – 850	INTEGRAL/SPI	>75	39 $\pm$ 3
	230 – 850	INTEGRAL/SPI	76 $\pm$ 15	42 $\pm$ 3
	400 – 2000	INTEGRAL/IBIS	67 $\pm$ 30	40 $\pm$ 15

Chap.2 The PoGOLite experiment

2.1 Overview of the PoGOLite

The PoGOLite (Polarized Gamma-ray Observer Light-weight version) is a balloon-borne polarimeter, using Compton scattering for polarimetry, measures the polarization of hard X-rays/soft gamma-ray from celestial objects in the energy range of 25—80 keV. This energy band has not been observed in the past. The general informations about PoGOLite is well described in Doctoral Thesis by Mózsi Kiss, Royal Institute of Technology[1]. There are some target objects for PoGOLite: Crab nebula, Cyg X-1 and so on, and PoGOLite has a ability to detect 10% liner polarization from the Crab nebula for 15 hours exposure time with above 99% confidence. It is optimized for point sources, with a narrow field of view of $\sim$1.25 msr (2.0 $\times$ 2.0 degree), and the accuracy of pointing observation is better than 0.1 degree. Because radiation from the sources, which spectrum is absorbed in the atmosphere follows an inverse power-law, the high float altitude of the instrument ($\sim$40 km) and sensitivity extending as low as possible are crucial, and allow data to be collected with good statistics even in a limited duration flight. The operation is international, involving institutes and universities from Japan[1], Sweden[2] and the United States[3].

The original version of PoGO consists of 397 detector cells, but evaluate backgrounds, cost estimates, prototype tests and Monte Carlo simulations demonstrated that a comparable performance could be achieved using a smaller detector array, consisting of 217 units. Such a “light-weight” instrument could reach a float altitude of up to 40 km and be able to measure a polarization degree as low as 10% from a 200 mCrab source in a six-hour flight [3]. The 61 PDC-unit version of PoGOLite “Pathfinder”, is prepared for a maiden-flight from northern Sweden in 2011 and 2013. In this thesis, I simply call "PoGOLite Pathfinder" as "PoGOLite". At July 6th, 2011 (UTC), there was a launch at Kiruna, Sweden. The flight was planned toward Canada (duration $\sim$5 days). However, there was He-leak from the balloon, and the gondola was returned to ground after $\sim$5 hours. At July, 2012, the gondola became flight ready at Kiruna for 2-week circumpolar flight. However, the weather was so bad that the flight was cancelled. Finally, PoGOLite was successfully launched from Kiruna, Sweden to Norilsk, Russia on July 12th at 0818 UT in 2013 (Fig. 2.1), using a 1.1 million cubic meter helium-filled balloon. A pioneering circumpolar flight was possible thanks to permission received from Russian authorities. The flight ended on July 26th when the gondola touched down close to the Siberian city of Norilsk ($\sim$3000 km to the East of Moscow) at 0015 UT. At mid-September the gondola has been transported from the tundra to an aircraft hangar

[1]Hiroshima University, Tokyo Institute of Technology, Yamagata University, Japan Aerospace Exploration Agency (JAXA).

[2]Royal Institute of Technology (KTH), Stockholm University (SU).

[3]Stanford Linear Accelerator Center (SLAC), Kavli Institute for Particle Astrophysics and Cosmology (KIPAC), University of Hawaii.

at Norilsk airport, and customs formalities are performed to secure further transport towards Sweden, PoGOLite has been transported to Kiruna in Sweden at mid-December and finally returned to Royal Institute of Technology at mid-January in 2014.

Figure. 2.1: The launch of PoGOLite from Esrange on July 12th 2013, 0818 UT. The distance from the top of the balloon to the gondola is ∼300 m.

2.2 Main detector of PoGOLite

There is a high rate bakcground in the region of aviation altitude (∼40 km). So there is need to reduce background, and we adopted well-type phoswich detector and BGO active shield for the main detector. The main detector consists of 61 well-type phoswich detector cells (PDCs), and 30 side anti-coincidence shields (SASs) with BGO (Fig. 2.2 left). Each PDC consists of three active components: a hollow "slow" plastic scintillator (60 cm long), a solid "fast" plastic scintillator (20 cm) and a BGO (bismuth

germanate oxide, $Bi_4Ge_3O_{12}$) crystal (4 cm). The three components are glued together using an optically transparent polyurethane-based adhesive (Fig. 2.2 right).

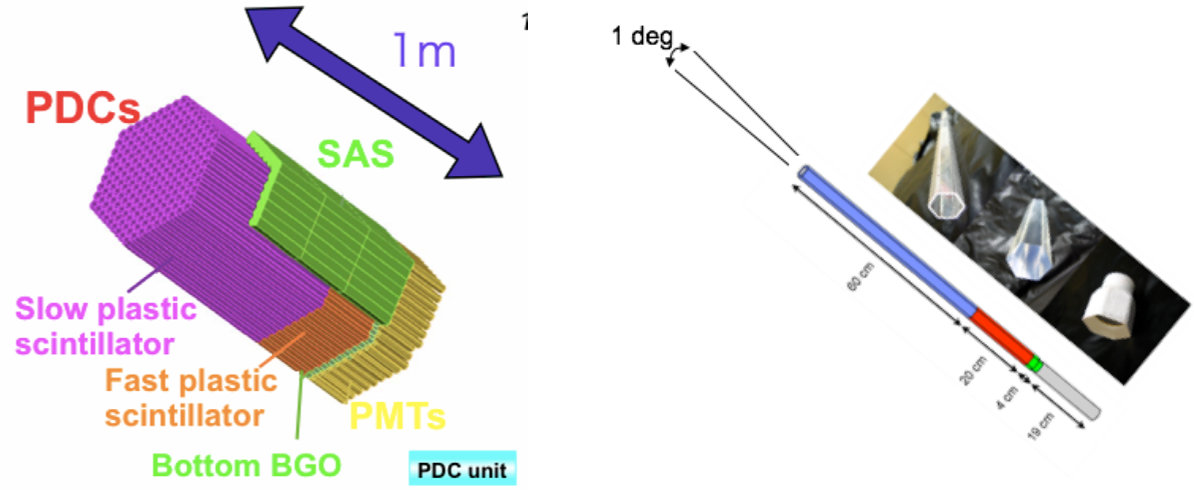

Figure. 2.2: Left: The main detector consists of 61well-type phoswich detector cells (PDCs) and 30 side anti-coincidence shields (SASs) with BGO for PoGOLite. Right: One of phoswich detector cells (PDCs), which is consisting of a hollow "slow" plastic scintillator (60 cm long), a solid "fast" plastic scintillator (20 cm) and a BGO (bismuth germanate oxide, $Bi_4Ge_3O_{12}$) crystal (4 cm).

Each scintillator has difference decay times, and the output from the charge-sensitive amplifier has different rise times (Fig. 2.3) — short (∼2 ns) for signals in the fast scintillator and longer (∼300 ns) for signals from the slow scintillator or the bottom BGO crystal —, and we can recognize reaction locus, and subtract background events. The PDC units are hexagonal so they can be tightly packed in a honey-comb structure, while surrounding SAS segments have two different pentagonal shapes to fit closely around detector array (Fig. 2.4).

2.3 Detection method of polarization

As indicated above, the PoGOLite instrument is using Compton scattering for polarimetry. Actual analysis procedures are followings (Fig. 2.5):

- Incident X-ray scatter in one of the PDC detectors.
- Scattered X-ray will scatter or be absorbed on another PDC.
- Tracking scattering event and detect scattering angle.

Because polarized photon tends to scatter toward the perpendicular direction (as mentioned in §1.2.3), tracking individual photons through coincident detection of Compton scattering and photoelectric absorption in a segmented detector volume of PDCs, can determine the polarization from celestial objects.

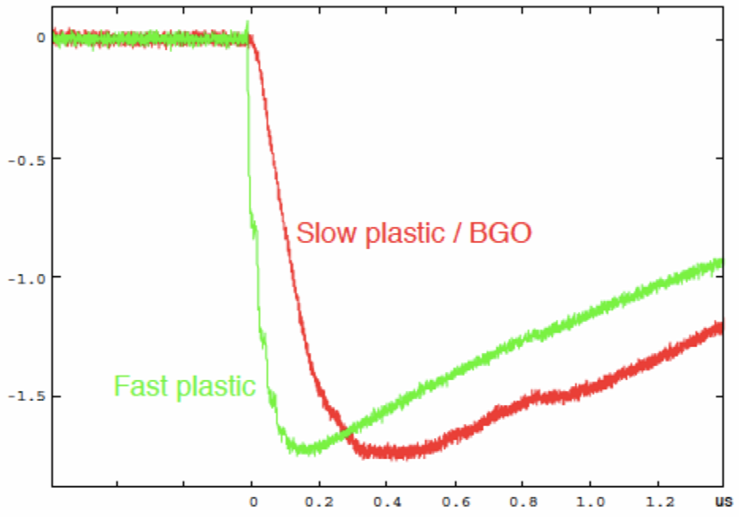

Figure. 2.3: Output from the charge-sensitive amplifier (shown with a negative polarity). The rise time is shorter for a signal from the fast plastic scintillator than for one from the slow scintillator or BGO crystal.

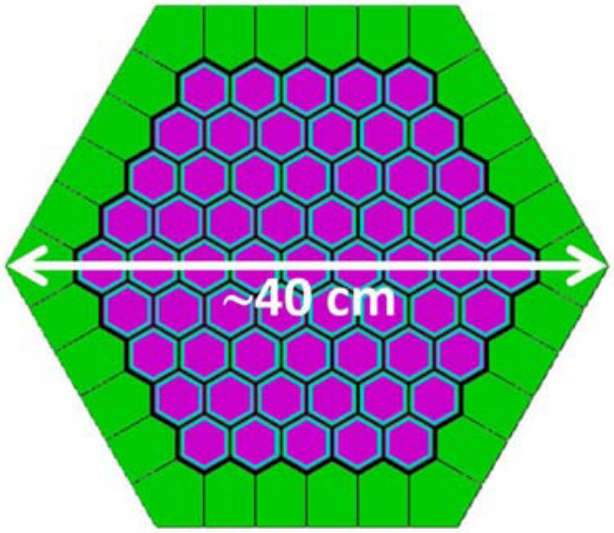

Figure. 2.4: Computer-generated top view of a 61-unit detector array. The PDCs (purple) are surrounded by a segmented side anti-coincidence shield (green).

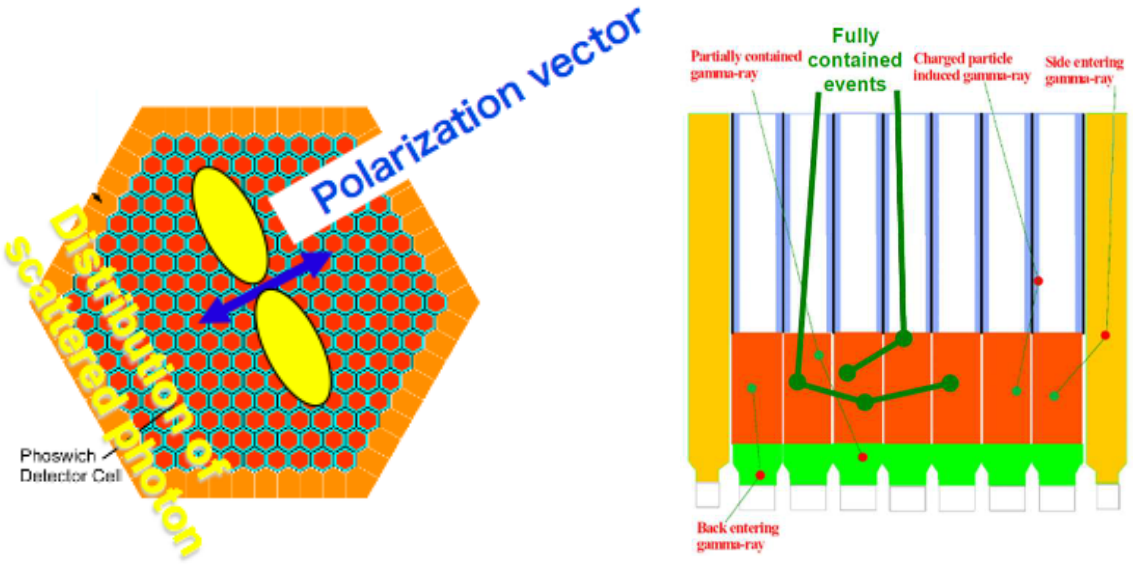

Figure. 2.5: The detection method of polarization. Left: Top view of the detector, polarization vector and distribution of scattered photon make perpendicular direction. Right: Cross section of the detector, tracking both of scattering and absorption position of X-rays. There are other background signals shown together.

2.4 The ground calibration with prototype detector

The detector response is indispensable to measure polarization. To make the accurate response, Geant4 simulation and good statistic ground calibration are needed, and the simulation must be consistent with the calibration.

To examine the capability of PoGOLite, a beam test of a simplified prototype detector array was conducted at KEK (高エネルギー加速器研究機構) in 2008, and this results is reported in H. Yoshida, Master thesis (Hiroshima Univ. 2009) [4]. The detector array consisted of 19 PDCs, and was irradiated by 90% polarized pencil beams of 50 keV. The data showed a clear polarization signal, with a measured modulation factor of 34% $\pm$ 5%. This was successfully reproduced at the $\sim$5% level by the computer simulation package Geant4 after modifications to its implementation of polarized Compton/Rayleigh scattering. To examine the capability of the PoGOLite flight detector, we have performed ground calibration with a radioisotope at Esrange Space Center (Sweden/Kiruna) in 2012–2013. The next chapter will be devoted to describing the ground calibration with the PoGOLite flight detector.

Detail about subtracting background events, threshold settings, attitude control system, instrument pointing, gondola and supplementary systems is written in Doctoral Thesis by Mózsi Kiss, Royal Institute of Technology [1].

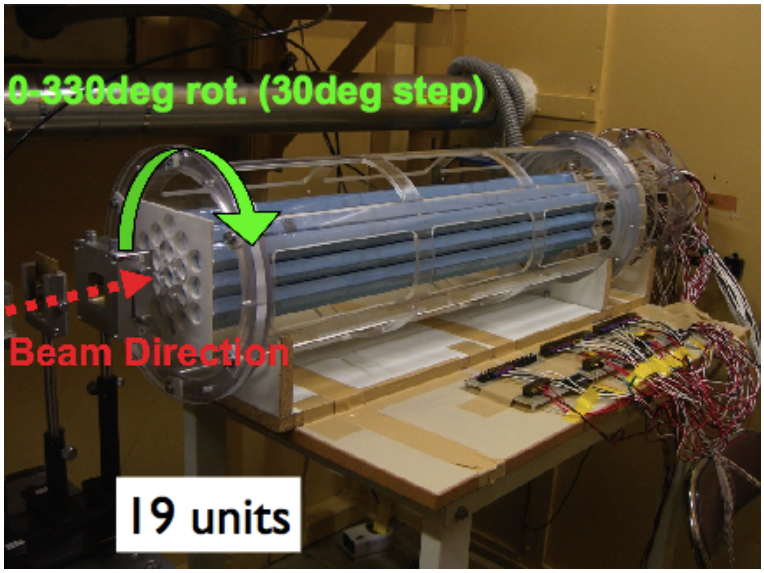

Figure. 2.6: A photograph of the PoGO prototype mounted on the rotation stage attached to the experiment table.

Chap.3 Ground calibration

3.1 Requirement of the ground calibration

There are requirements for PoGOLite detector to detect polarization from celestial objects, and some tests have been done on ground.

Gain of each PDC: To know the gain and energy resolution of each PDC, ground calibration for all PDCs has been done. 59.5 keV gamma-rays from ^{241}Am were irradiated to each PDC for 60 seconds, and the peak of 59.5 keV is corrected at 1200 ADC channel with adjusting the high voltage of the PMT.

Angular response: Since we need to decide the flux of celestial objects, angular response of the detector has been measured. There is a also need to recognize the component which has a periodic wave of 360 degree in the modulation factor caused by the miss alignment between on-axis of the detector and direction of the celestial object. Fixing the elevation and changing azimuth of the detector, we have irradiated 59.5 keV gamma-rays from ^{241}Am, and we have measured angular response of the detector.

Time resolution: There is a also need to measure time resolution of the detector, since we observe the Crab pulsar in the Crab nebula, whose period is 33 milli seconds, and we want to resolve the pulse with 128 bins. Therefore we need the time resolution of $\sim$26 μs. Using cosmic muons and GPS signal, we have evaluated the time resolution of the detector, and confirmed that the time resolution is better than $\sim$1 μs.

Modulation factor: As mentioned above, the ground calibration with prototype detector has carried out in KEK, Japan, and it is consistent with simulation. We also calibrate the flight-detector. For non-polarized gamma-ray, we need to suppress the MF caused by systematic error less than $\sim$1% (flat) in order to observe the modulation of the celestial objects. For polarized gamma-ray, we also need to determine the MF with the statistics better than $\sim$1%. To achieve the requirement, we have carried out over 150-hour calibration with scatter piece and ^{241}Am source for several setups (Table. 3.1).

Following sections, I show results of spectrum, modulation curve, event distribution among 61 PDCs and so on.

3.2 The ground calibration with the flight detector of PoGOLite

3.2.1 Setup of the calibration

For the ground calibration, we irradiated the detector with 59.5 keV gamma-ray from the radioisotope of ^{241}Am (Fig. 3.1). With setting the scatter piece by the radioactive source, the gamma-ray will be polarized (∼90% polarization) at the scattering. Without the scatter piece, we irradiate non-polarized gamma-ray. The geometry between the radioactive source, the scatter piece, the scattered photon and the polarization angle is showed in figure 3.2. In upper left of figure 3.2, we irradiate polarized gamma-ray with 90/270 polarization angle. In upper right of figure 3.2 , we irradiate polarized gamma-ray with 0/180 polarization angle.

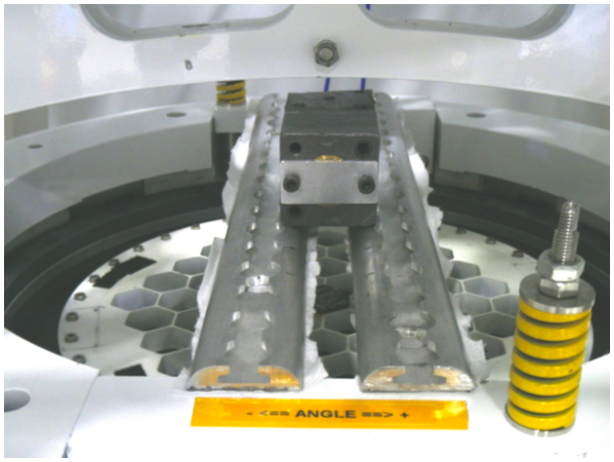

Figure. 3.1: A photograph of the ground calibration with ^{241}Am and PoGOLite flight detector.

We use a "fast" plastic scintillator or a polyethylene as a scatter, and the source and the scatter are covered with lead blocks with the hole size of 5 mm diameter. In 2012, we used a "fast" plastic scintillator and acrylic cover as a scatter, and the scattering scintillator was unintentionally rotated, so when the beam comes into the scatterer from the source, it is not going through the groove that it is supposed to go through, but rather irradiating at least some part of the acrylic holder itself. Furthermore, even if the beam goes through the groove, it can scatter in the holder itself (after passing through the scattering scintillator without interacting). This means that the beam is not as uniform as previously expected and the beam might be shifted relative to the central this position (a order of a few mm). Therefore we have changed the scatter piece for a polyethylene in 2013 (Fig. 3.3).

From the simulation and actual measurement described below, we found that the difference of these scatter pieces do not cause significant differences in the current configurations (c.f. §3.3.2).

When the detector is measuring some modulations, instrument uniformly rotate with a period of five minutes to cancel systematic error. Moving the source from Center PDC to Ring4 of the detector, we irradiate every part of the detector using the instrument rotation (Fig. 3.4). We have operated ground calibration experiment all-day long continuously for over 150 hours (Table. 3.1).

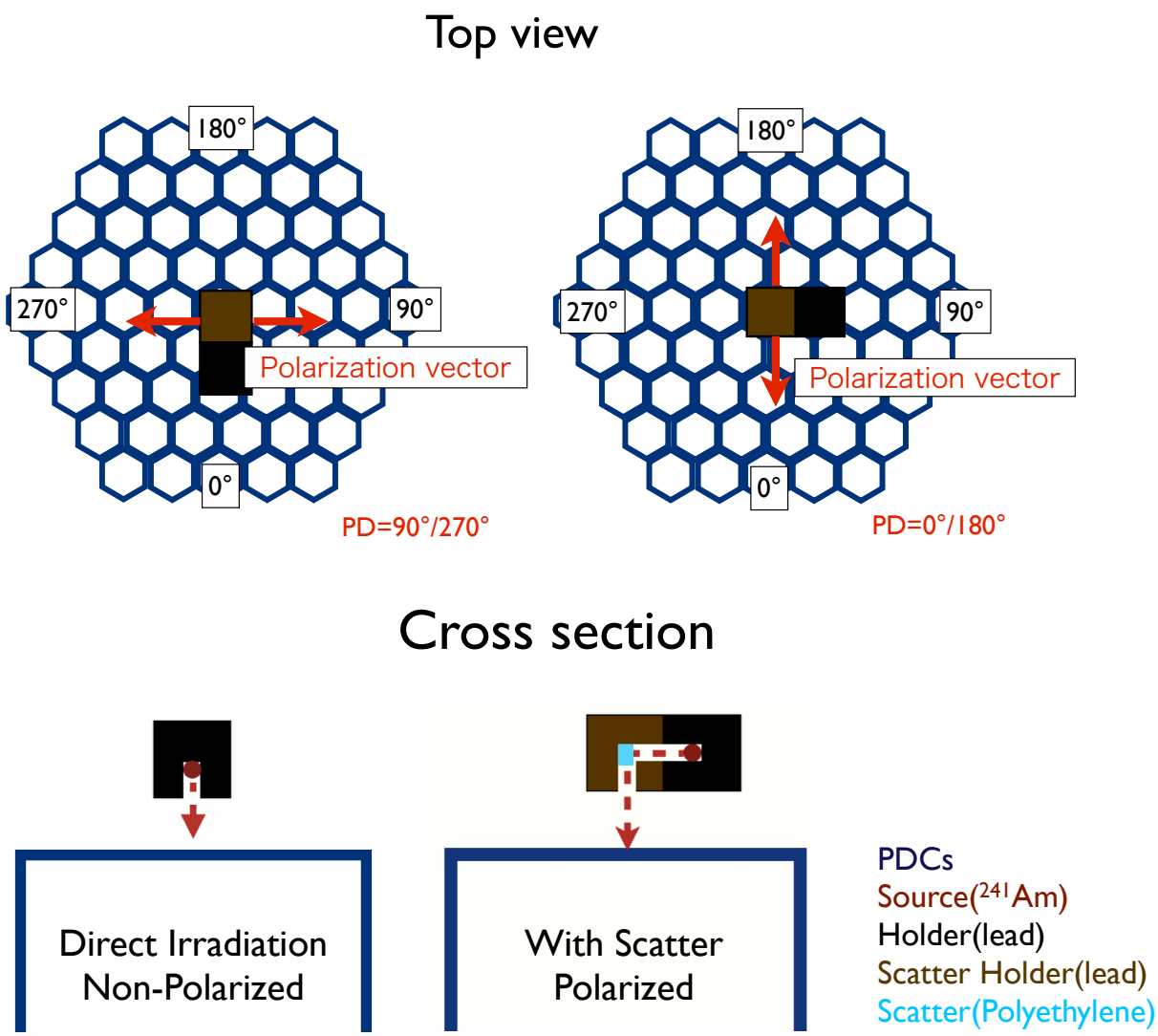

Figure. 3.2: Cartoons of the ground calibration setup. Upper: Top view. Lower: Cross section.

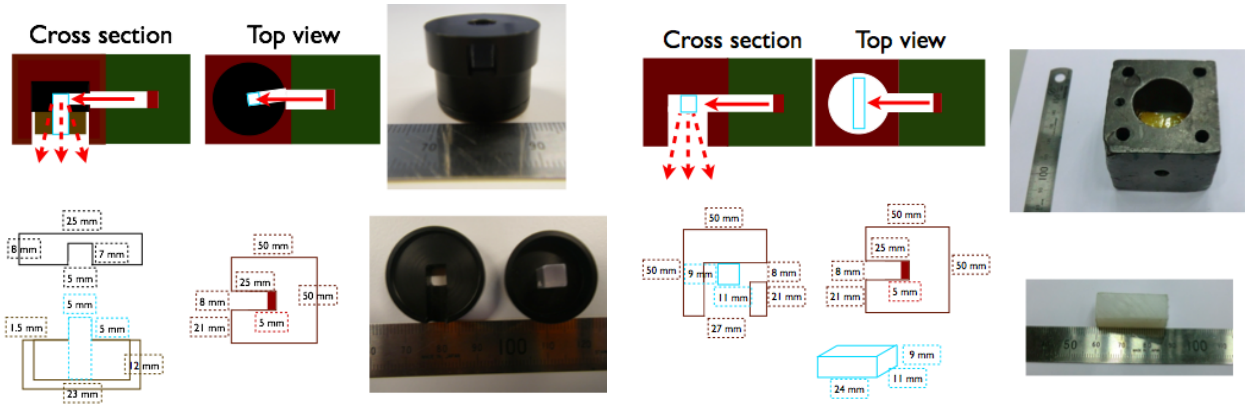

Figure. 3.3: Photograph and cartoon of scattering piece. Left: 2012, Right: 2013.

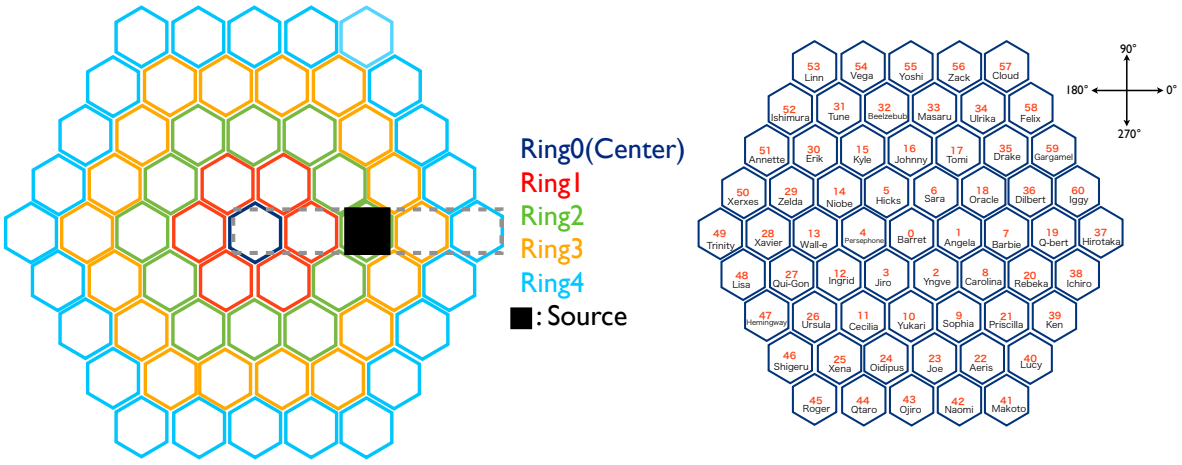

Figure. 3.4: Definition of the Ring0-4, PDC number, PDC name of the detector. Left: Position of the scattering piece from the center to the Ring4 to irradiate every ring of the detector. Right: Definition of PDC number (0-60) and name.

Table. 3.1: The list of ground calibration measurements

2012			
Source position/background	Polarized (90/270 degree)	Polarized (0/180 degree)	Non-polarized
Center	1440 min	600 min	30 min
Ring1	505 min	610 min	30 min
Ring2	625 min	570 min	30 min
Ring3	600 min	-	30 min
Ring4	925 min	-	30 min
Room background with plastic cover	30 min		
Room background without plastic cover	200 min		
"New" background with lead sheet	250 min		
"New" background with lead block	250 min		

2013			
Source position/background	Polarized (90/270 degree)	Polarized (0/180 degree)	Non-polarized
Center ("fast" plastic)	500 min	-	-
Center (polyethylene)	750 min	-	-
Center (with rotation)	-	-	30 min
Center (without rotation)	-	-	15 min
Ring1	275 min	-	20 min
Room background without plastic cover	300 min		
"New" background with lead sheet	295 min		
others	Center irradiating, with collimator (1.25 cm length, 2.0 mm phi), 5 min		
	Center irradiating, with collimator (1.25 cm length, 2.5 mm phi), 5 min		
	Center irradiating, with collimator (1.25 cm length, 3 mm phi), 5 min		
	Center irradiating, with collimator (2.5 cm length, 2.0 mm phi), 5 min		
	Center irradiating, with collimator (3.75 cm length, 2.0 mm phi), 5 min		
	Center irradiating, with collimator (5.0 cm length, 2.0 mm phi), 10 min		
	Center irradiating, with collimator (6.25 cm length, 2.0 mm phi), 5 min		
	Center irradiating, with collimator (7.5 cm length, 2.0 mm phi), 5 min		
	Center irradiating, with collimator (7.5 cm length, 2.0 mm phi), 5 min		
	Barbie irradiating, without collimator, 5 min		
	Barbie irradiating, with collimator (2.5 cm length, 2.0 mm phi), 5 min		
	Wall-e irradiating, without collimator, 5 min		
	Wall-e irradiating, with collimator (2.5 cm length, 2.0 mm phi), 15 min		
	Wall-e irradiating, with collimator (5.0 cm length, 2.0 mm phi), 5 min		
	Wall-e irradiating, with collimator (7.5 cm length, 2.0 mm phi), 5 min		
	Wall-e irradiating, with collimator (10.0 cm length, 2.0 mm phi), 5 min		

3.2.2 The techniques to make modulation curve

Event selections

We apply some event selections to measure the MF performance of the detector. Here, we select only 2-hit events which mean that a gamma-ray scatter at one PDC and then absorbed at another site. There are three parameters to define one set of the event selection: irradiation site, scattering site, and absorption site. For example, irradiating gamma-ray at Center PDC, scattering site is any PDC among 61 and absorption site is also any PDC, we call with events with this selection as Center irradiating any scattering any absorption event. Similarly, irradiating at Center PDC, scattering site is restricted only at Center PDC, while absorption site is any PDC, we call the event as Center irradiating Center scattering any absorption event. In addition, irradiating at Center PDC, scattering site is also Center and absorption site is limited at one of the 6 PDCs in Ring1, we call the event as Center irradiating Center scattering Ring1 Absorption event. Using a similar method, we define event selections in figure 3.5.

"Any scattering any absorption" events independent from the source position are also called as "All-2hit" events since we choose all the 2-hit events. "Center irradiating Center scattering Any absorption" is often used and sometimes called as "CenterCentral" event.

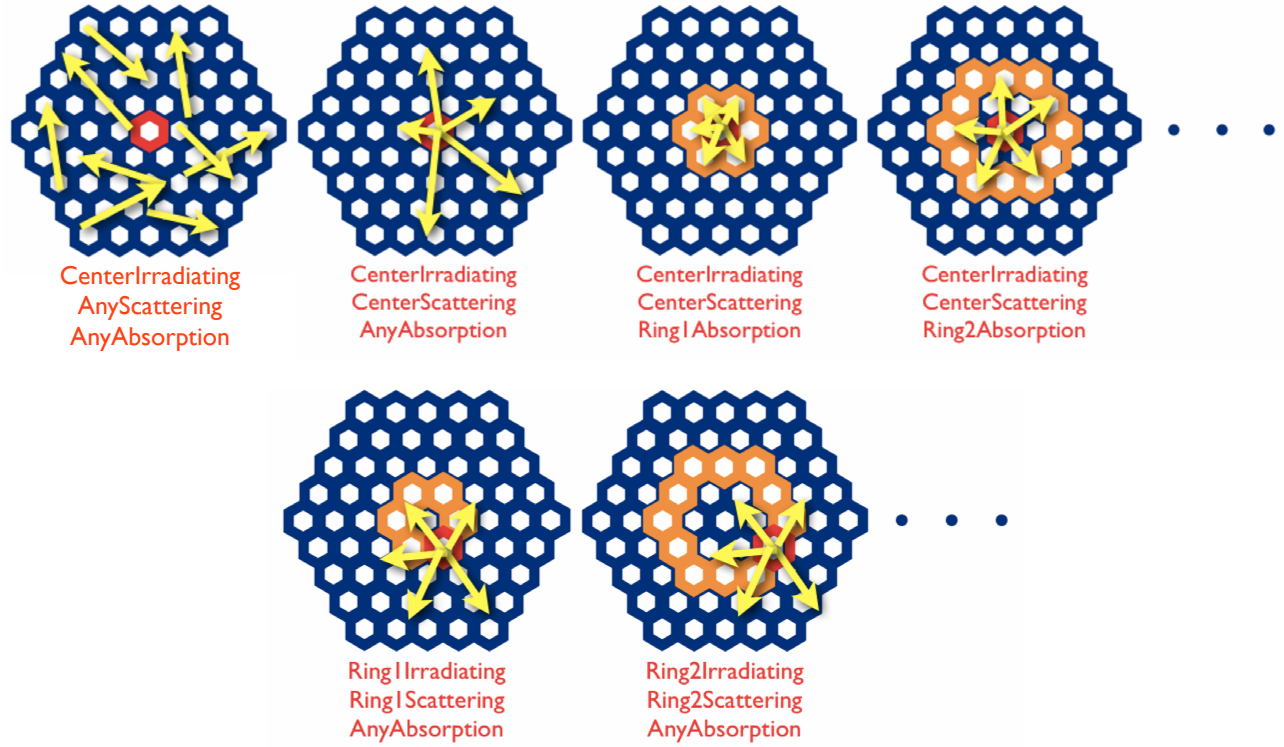

Figure. 3.5: The definition of some event selections of 2-hit events. There are three parameters to define one event selection, irradiation site, scattering site and absorption site.

Fitting functions

To evolute a modulation curve (c.f. Fig. 1.7), we use two factions to fit the curve in the following way:

$$f_1(x) = P_0[1 + P_0 cos(2(x - P_2))] \quad (3.1)$$

$$f_2(x) = P_0[1 + P_0 cos(2(x - P_2))] + P_3 cos(x - P_4) \quad (3.2)$$

where x is azimuthal angle, and P_2 is polarization angle of the source, equation (3.1) is the function for "normal" modulation curve fitting with the azimuthal-angle period of 180 degrees. Equation (3.2) is equation (3.1) and the asymmetric background, which is represented with the period of 360 degree.

Randomization

There is a special technique to make a modulation curve, which we call as "Randomization". Randomization is studied in Doctoral Thesis by Cecilia Marini Bettolo, Royal Institute of Technology [2]. When reconstructing the azimuthal angle of the real data, there is no positional information of where the energy is deposited within the scintillator. With the simulated data, this information is available, but the same conditions as with real data are used here. When a photon undergoes Compton scattering in a PDC and is photo-absorbed in a second PDC, there is an uncertainty of where exactly both events take place.

The reconstructed azimuth angle is the one obtained by connecting the two centers of the PDCs even though the events are not centered in the PDCs, so 2-hit events with two different angles are reconstructed as having the same azimuthal scattering angle (Fig. 3.6). In order to take into account this effect, the azimuth angle distribution is smeared out. This is done by choosing randomly the azimuthal scattering angle from a Gaussian distribution, so we call this technique as "Randomization". The standard deviation width, σ, is obtained by fitting the distribution of the simulated events in the PDCs with a Gaussian centered around the center-to-center angle. If the hits are not in adjacent PDCs cells, the σ will be smaller. The value of σ has been found to depend on d, the separation between Compton and photo-absorption site as shown in equation (3.3).

$$\sigma = 11.09 \times \left(\frac{1}{d + 0.356} + \frac{1}{d - 0.356}\right) \; [degree] \quad (3.3)$$

where d is given in units of numbers of PDCs. The smearing reorders statistically the scattering angles, and this is enough to remove the uncertainty on the azimuth angle.

It is shown that the azimuthal scattering distribution, both in the case of with Randomization and without Randomization for a 100% polarized signal with 0 polarization angle (Fig. 3.7). The modulation curve has been fitted with a equation (3.1). The fit of the with Randomization data (Fig. 3.7: green curve) gives a modulation factor of 20.3% ± 0.7% with 178.7 ± 1.8 polarization angle. The fit of the without Randomization data (Fig. 3.7: red curve) gives a modulation factor of 50.3% ± 0.6% with 135.2 ± 0.3 polarization angle. This shows that if the data are not randomized, polarization angle is away

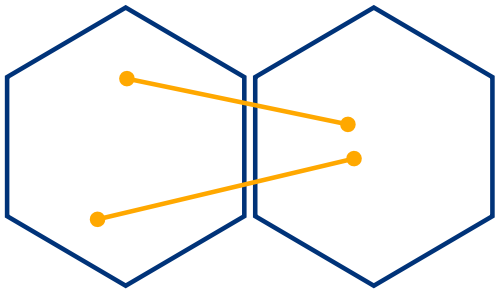

Figure. 3.6: Example of azimuth scattering angle reconstruction, and example of how two events with two different angles are reconstructed the same angle. In order to take into account this effect the azimuth angle distribution can be smeared out. [2]

from the actual angle, and modulation factor is higher than randomized one. If the analysis would be performed on each ring of PDCs separately, then the Randomization would not be needed. We can get modulation curves for each ring of PDCs around the Compton scattering center. The Randomization allows to reconstruct angles smaller than 60 degree, thus the number of bins when reconstructing the azimuthal distribution can be increased.

In the case of PoGOLite, Randomization is not needed, since the instrument is rotating during observations as mentioned §3.2.1, so inherently, there are a lot of bins. [2]

3.3 The results of the calibration

I have analyzed all calibration data and made spectra, 2-hit event distribution among 61 PDCs, and modulation curves. I have also estimated the modulation factor of PoGOLite detector. These results are compared with results of simulation.

3.3.1 Energy spectra

Irradiating non-polarized gamma-ray from ^{241}Am at the central PDC, I selected all the event detected at the PDC (Fig. 3.8), where the hit threshold and trigger threshold were 10 ADC channel (corresponding to 0.97 keV) and 300 ADC channel (corresponding to 14.4 keV), respectively. Since the gain is adjusted by the high voltage, the 59.5 keV peak appears at ∼1200 ADC channel. The number of events below trigger threshold of 300 ADC channel is small because these events are stored only when other PDC issues the trigger simultaneously.

3.3.2 Distribution of the interaction site among 61 PDCs

Using 2012 data, I have made distributions of 2-hit events for 61 PDCs with statistical errors, and all data are normalized per one minute (Fig. 3.10). The data sets are two sets of the ^{241}Am polarized

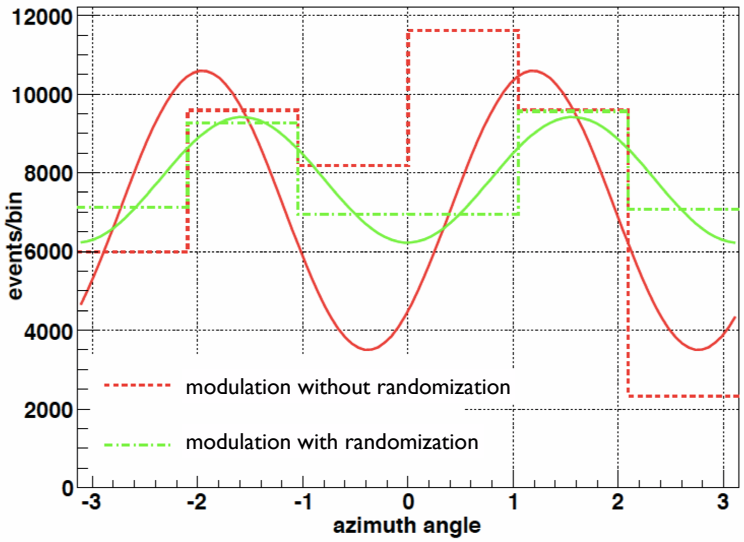

Figure. 3.7: Comparison between with Randomization and without Randomization data: the distribution of the with Randomization data (green histogram) are fitted with the (green) modulation curve. The without Randomization data (red histogram) are fitted with the modulation (red) curve. The fit of the with Randomization data gives a modulation factor of 20.3% ± 0.7% with 178.7 ± 1.8 polarization angle. The fit of the without Randomization data gives a modulation factor of 50.3% ± 0.6% with 135.2 ± 0.3 polarization angle. [2]

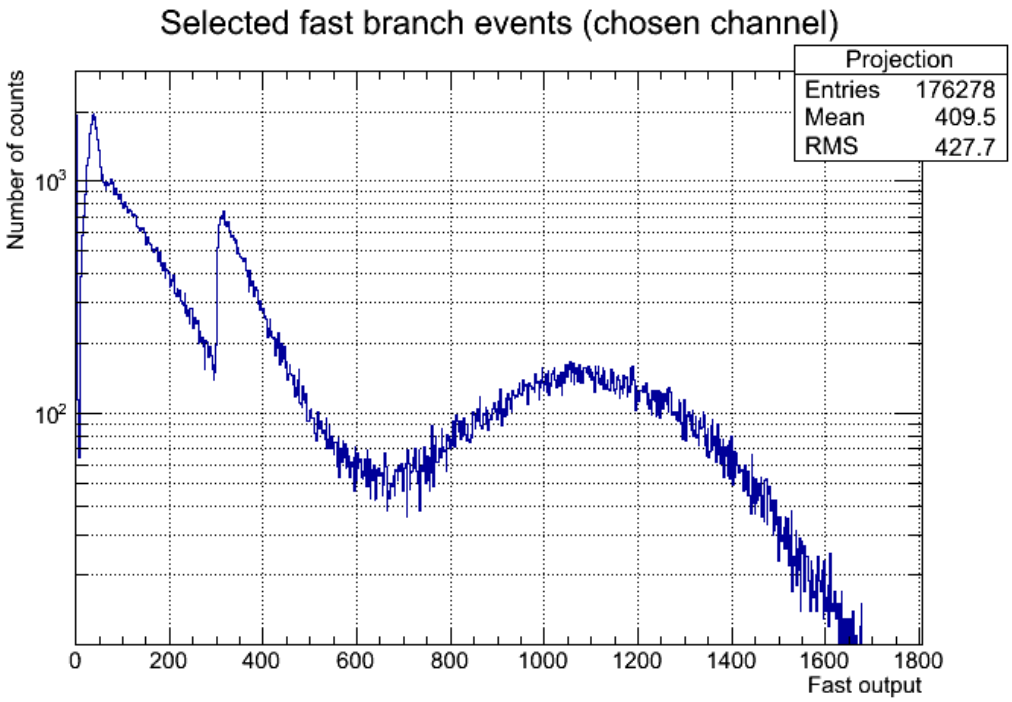

Figure. 3.8: The spectrum of ^{241}Am measured by the central PDC, with irradiating gamma-ray at the central PDC.

gamma-ray irradiating the central PDC with the different polarization angles of 0/180 and 90/270, room background and "new" background, where "new" background is estimated with the special setup using ^{241}Am and a lead sheet or a lead block (Fig. 3.9). Selecting all 2-hit events, I plotted scattering site.

In the figure 3.10, "new" background with the lead sheet (Fig.3.9 (2)) and "new" background with the lead block (Fig.3.9 (3)) have the same event rate, and can explain almost all events for polarization measurements of Ring3 and Ring4. Therefore, we think almost all scattering events at Ring3 or Ring4 are background, and the number of the events is twice larger than that of the room background. Following sections, I simply say "new" background with the lead sheet as "new" background, because there is no difference between sheet and block. We can also see the direction of the polarization degree does not effect the distribution of the interaction site.

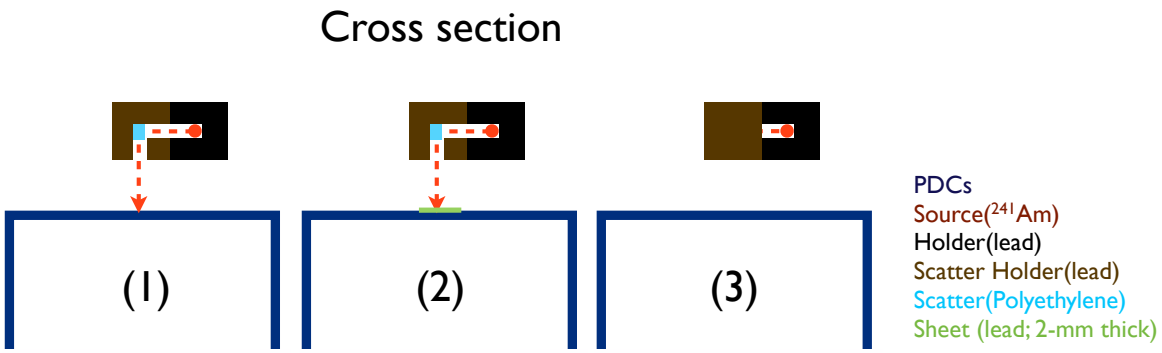

Figure. 3.9: The setup of "new" background compared with (1): Normal polarized irradiation, (2): The center PDC is covered with a 2-mm thick lead sheet, and (3): The lead block of scatter holder is rotated by 90 degree, and the ^{241}Am source is blocked.

Subtracting "new" background from the polarization measurements, we can obtain more accurate distribution (Fig. 3.11). In the figure, we can see less events in the polarization measurement than that in the room background one in Ring3 and Ring4.

To check the difference caused by changing scatter piece from 2012 to 2013, I have compared four data: (1) 2012 Center irradiating polarized gamma-ray with 90/270 polarization angle for 1440 minutes after subtracting "new" background of 2012, (2) 2012 Center irradiating non-polarized (without the scatter piece) for 30 minutes, (3) 2013 Center irradiating polarized gamma-ray with 90/270 polarization angle for 750 minutes after subtracting "new" background of 2013, and (4) 2013 Center irradiating non-polarized (without the scatter piece) gamma-ray for 30 minutes (Fig. 3.12). In this figure, it is normalized that the number of events in Center PDC becomes 1, Therefore, I concluded that there are no significant effects by different scatter pieces, and that the high statistical data obtained in 2012 are better to be analyzed and compared with simulation in detail. Here, the number of non-polarized events is much higher than that of background events, and there is no need to subtract background. Jiro (PDC number = 3, c.f. Fig. 3.4) always has lower number of events in Ring1. This is discussed later.

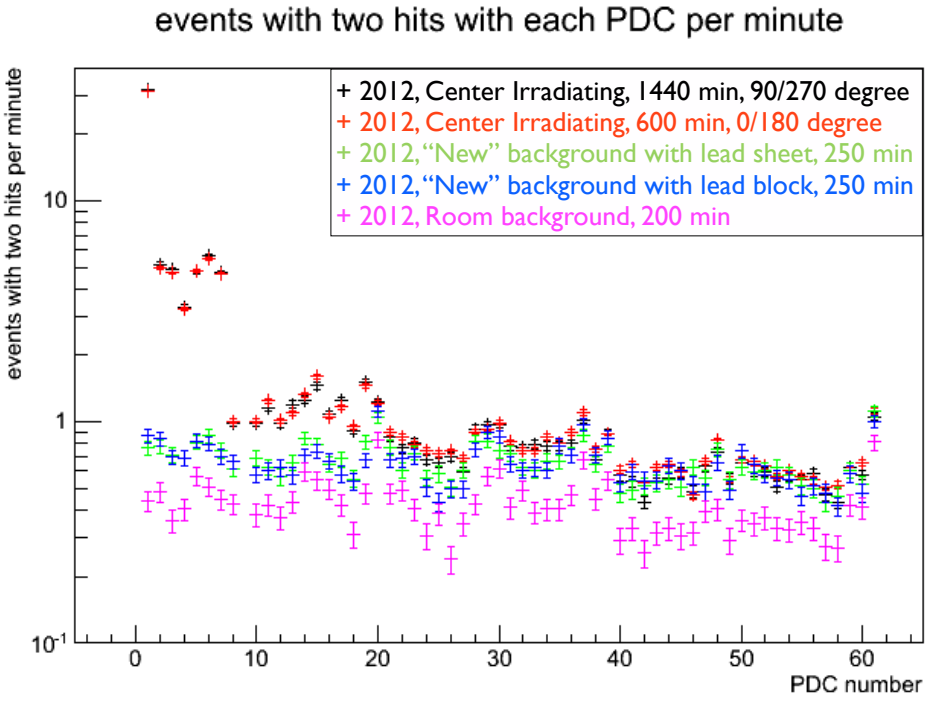

Figure. 3.10: The distribution of the interaction site among 61 PDCs in 2012.. Black: Center irradiating polarized gamma-ray with 90/270 polarization angle for 1440 minutes. Red: Center irradiating polarized gamma-ray with 0/180 polarization angle for 600 minutes. Green: "New" background with lead sheet for 250 minutes (Fig. 3.9 (2)). Blue: "New" background with lead block for 250 minutes (Fig. 3.9 (3)). Magenta: Room background for 200 minutes.

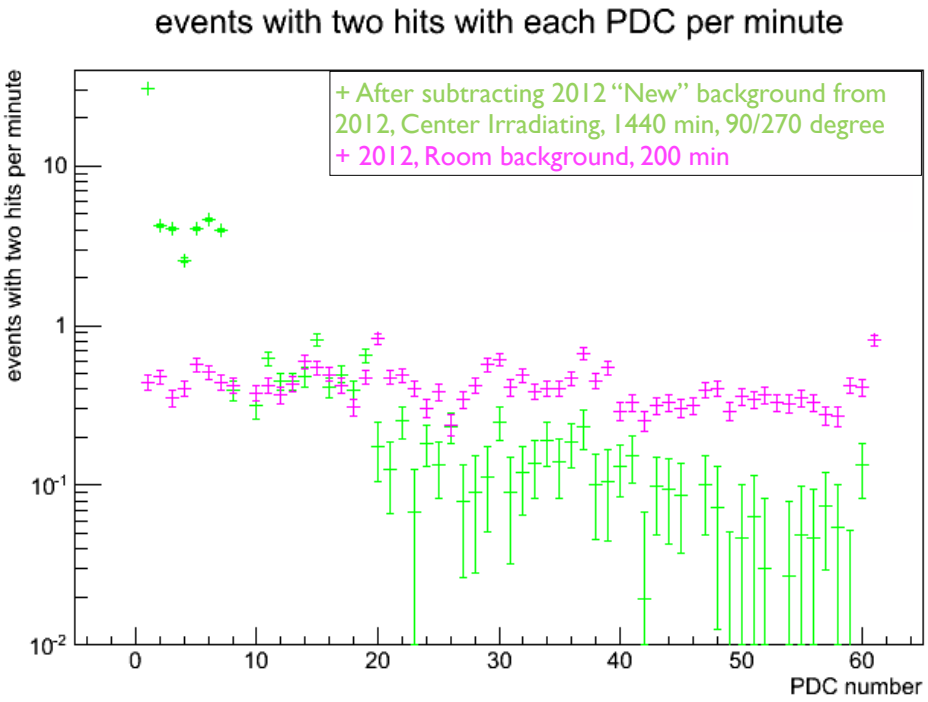

Figure. 3.11: The distribution of the interaction site among 61 PDCs in 2012. Green: After subtracting "new" background from Center irradiating polarized gamma-ray with 90/270 polarization angle for 1440 minutes. Magenta: Room background for 200 minutes.

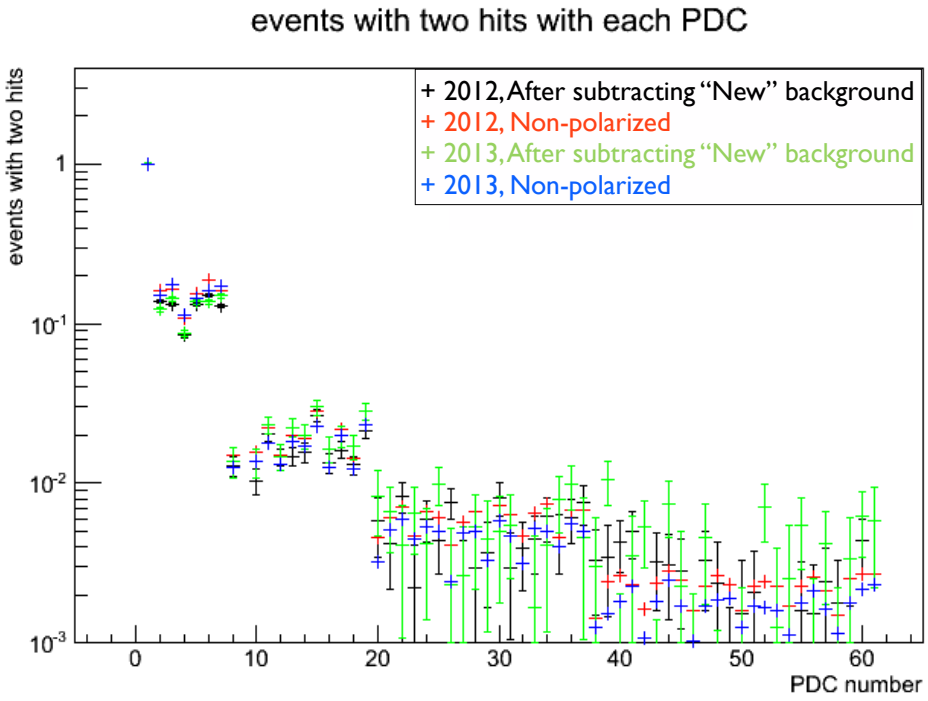

Figure. 3.12: The same as figure 3.11 but for the comparison between different scatter pieces and with out the scatter piece. Black: 2012 Center irradiating polarized gamma-ray with 90/270 polarization angle for 1440 minutes after subtracting "new" background of 2012. Red: 2012 Center irradiating non-polarized (without the scatter piece) gamma-ray for 30 minutes. Green: 2013 Center irradiating polarized gamma-ray with 90/270 polarization angle for 750 minutes after subtracting "new" background of 2013. Blue: 2013 Center irradiating non-polarized (without the scatter piece) gamma-ray for 30 minutes.

3.3.3 Modulations curves

I created many modulation curves with changing the selection way, and show some results here. Others are in Appendix A.

The data sets shown here are measured in 2012 as irradiating polarized/non-polarized gamma-ray (polarization angle is 90/270 or 0/180) at Center PDC, and "new" background. Event selections are "All-2hit" event (Fig. 3.13) and "CenterCentral" event (Fig. 3.14). We can estimate MF from these figures. After subtracting "new" background, we can obtain more accurate MF. These modulation curves are fitted with equation (3.2), and the results are listed in table 3.2 and table 3.3.

If polarization angle is 90/270 degree, scattered gamma-rays tend to take a scattering angle of 0/180 degree (c.f. §1.2.3). In these figures, we can see clear sinusoidal modulation curves. Modulation curves without Randomization have higher MF than those with Randomization. The MFs after subtracting "new" background are roughly 22% for "All-2hit" event, and 35% for "CenterCentral" event. The systematical error can be shown as MF of non-polarized gamma-ray, and is better than ∼1 %. Therefore the requirement of the ground calibration has been achieved.

Table. 3.2: The list of parameters of the modulation curves using Center irradiating data with "All-2hit event"

"All-2hit" event	Exposure time (minutes)	Entries	MF before subtracting "new" background (%)		MF after subtracting "new" background (%)	
			without Randomization	with Randomization	without Randomization	with Randomization
90/270 degree	1440	148565	13.66±0.37	11.81±0.37	22.2±0.59	18.8±0.58
0/180 degree	600	61460	13.18±0.57	11.11±0.57	21.1±0.91	17.8±0.91
Non polarized	30	274746	0.067±0.27	0.24±0.27	0.067±0.27	0.24±0.27
"New" background	250	9902	2.5±1.4	2.2±1.4	-	-

Table. 3.3: The list of parameters of the modulation curves using Center irradiating data with "Center-Central" event

"Center Central event"	Exposure time (minutes)	Entries	MF before subtracting "new" background (%)		MF after subtracting "new" background (%)	
			without Randomization	with Randomization	without Randomization	with Randomization
90/270 degree	1440	45184	33.84±0.64	29.89±0.64	34.7±0.70	31.5±0.68
0/180 degree	600	19102	32.15±0.99	28.59±1.00	33.0±1.05	30.2±1.1
Non polarized	30	118789	0.49±0.41	0.40±0.41	0.49±0.41	0.40±0.41
"New" background	250	191	6.3±11	3.3±11	-	-

3.3.4 Comparison with the simulation

In this section, I compare the results of the ground calibration with Geant4 simulation. The simulation has been performed by the PoGOLite team.

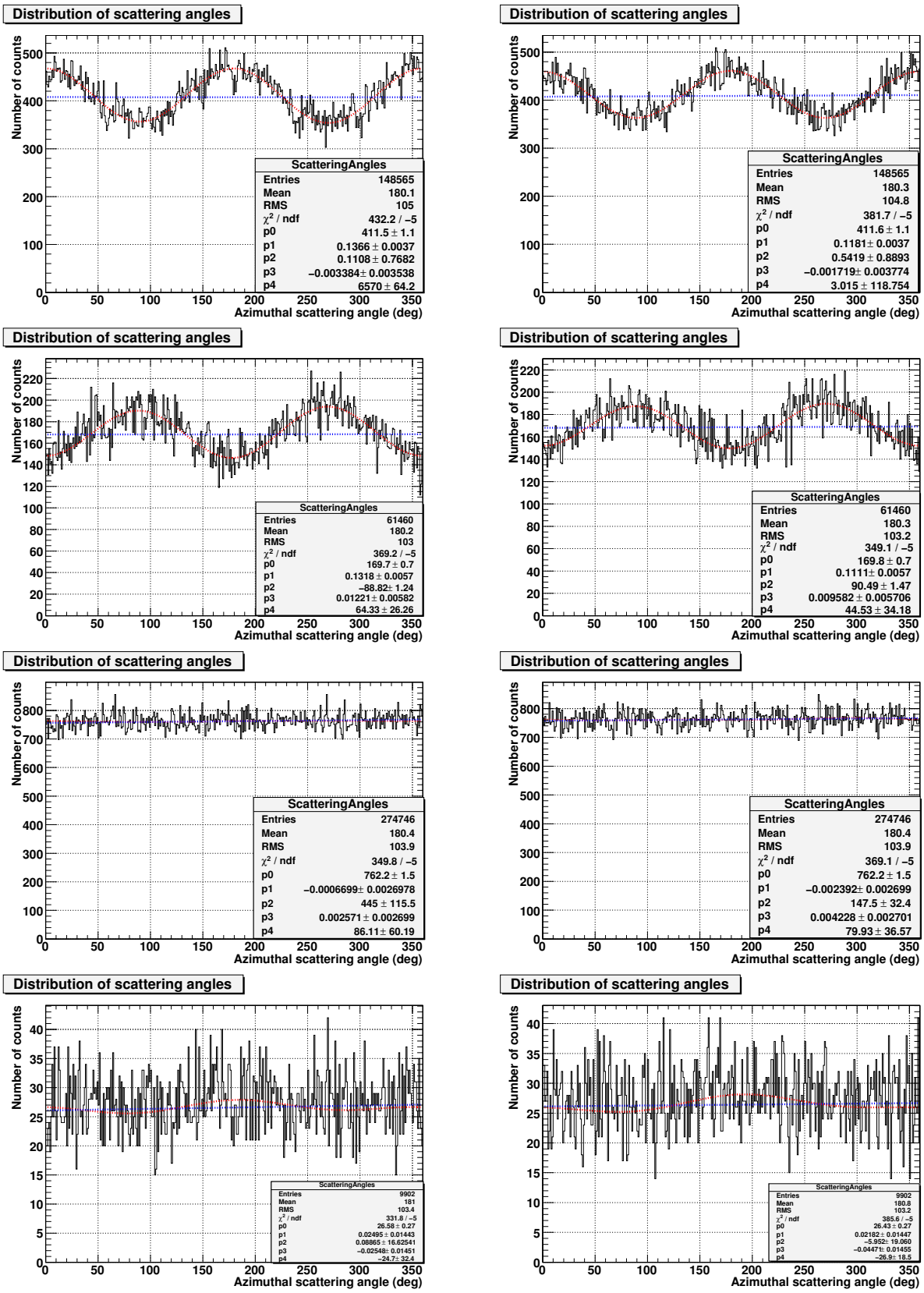

Figure. 3.13: Modulation curves with irradiating polarized/non-polarized gamma-ray at the Center PDC. The event selection is "All-2hit" event. Upper left: Polarization angle is 90/270 degree without Randomization. Upper right: Polarization angle is 90/270 degree with Randomization. Upper middle left: Polarization angle is 0/180 degree without Randomization. Upper middle right: Polarization angle is 0/180 degree with Randomization. Lower middle left: Non-polarized gamma-ray without Randomization. Lower middle right: Non-polarized gamma-ray with Randomization. Lower left: "New" background without Randomization. Lower right: New" background with Randomization.

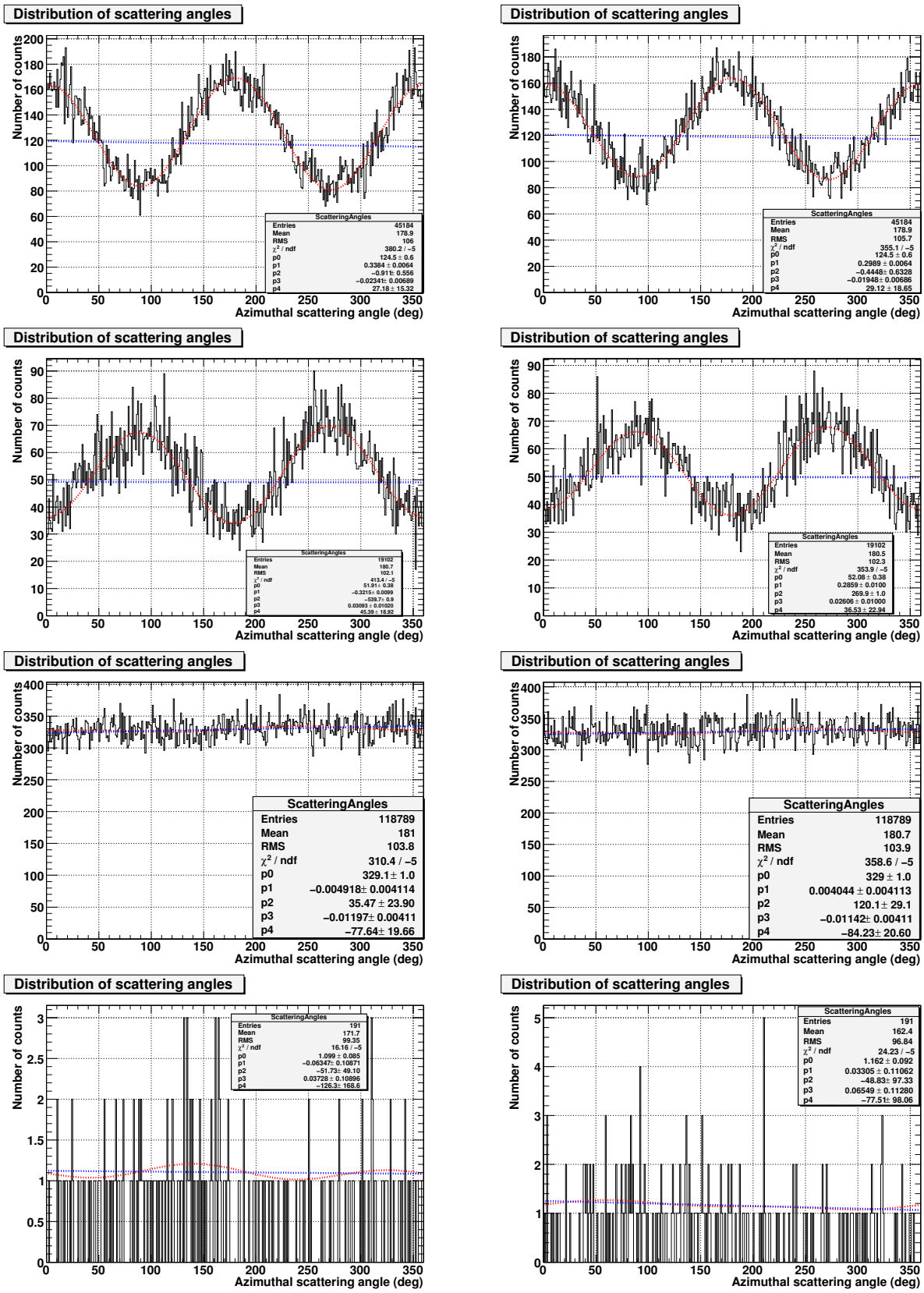

Figure. 3.14: The same as those is figure 3.13 but for the event selection of "CenterCentral" event.

Comparison of the distribution of the interaction site

I compared the results of the distribution of the interaction site among 61 PDCs between ground calibration and Geant4 simulation (Fig. 3.15). In this figure, it is normalized that the number of events in Center PDC becomes 1, and both data show almost the same events in Ring2, Ring3 and Ring4. However, in the ground calibration, there are twice higher events is in the Ring1 than that of the Geant4 simulation.

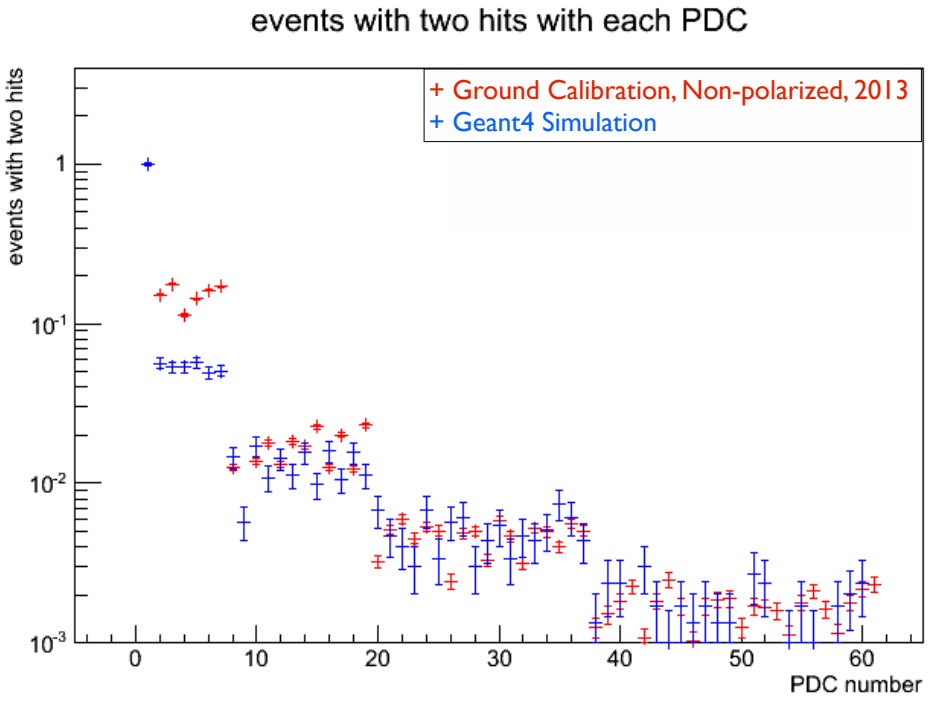

Figure. 3.15: Comparison between ground calibration and Geant4 simulation of the distribution of the interaction site among 61 PDCs. Red: The ground calibration, irradiating non-polarized gamma-ray at Center PDC in 2013. Blue: The Geant4 simulation with the same setup for as ground calibration.

Comparison of the MFs

I also compared the modulation curves of the ground calibration and the Geant4 simulation (Fig. 3.17). For the ground calibration, the data of irradiating polarized gamma-ray with 90/270 polarization angle at Center for 1440 minutes are used. These modulation curves for the ground calibration are after subtracting "new" background. The setup of the Geant4 simulation is realistic to reproduce the ground calibration: the scatter piece is made of a polyethylene and has the same size of 2013, the energy of irradiated beam is 59.5 keV, rotation of the polarimeter is over 360 degrees by 0.1 degree step. Both analysis does not apply Randomization. However, the irradiating site of gamma-ray is somewhat

different between the ground calibration and the Geant4 simulation (table. 3.4, Fig. 3.16). These results of modulation curves are listed in table 3.5. In this table, ratios of entries to that of "CentreCentral" event are listed to compare between ground calibration and Geant4 simulation. Additionally, the entries of "new" background and their ratios are listed together, which ratios are normalized with the observation time and entries of "CentreCentral" event of the polarized gamma-ray. The ratio of entries of the Geant4 simulation should be consistent with background-subtracted ratio of the ground calibration (the ratio of "entries of Center Irradiating polarized gamma-ray" minus "normalized entries of "new" background"). Almost all results of the ratio of the ground calibration are roughly consistent with the ratio of the Geant4 simulation. However, there are large difference in "All-2hit" event and Ring1Scattering AnyAbsorption event.

Table. 3.4: The positions of the scatter piece (x, y) mm

	Center	Ring1	Ring2	Ring3	Ring4
Gound calibration	(0.0, 0.0)	(0.0, 30.0)	(0.0, 60.0)	(0.0, 79.5)	(0.0, 108)
Geant4 simulation	(0.0, 0.0)	(0.0, 30.0)	(0.0, 56.0)	(0.0, 83.0)	(0.0, 110)

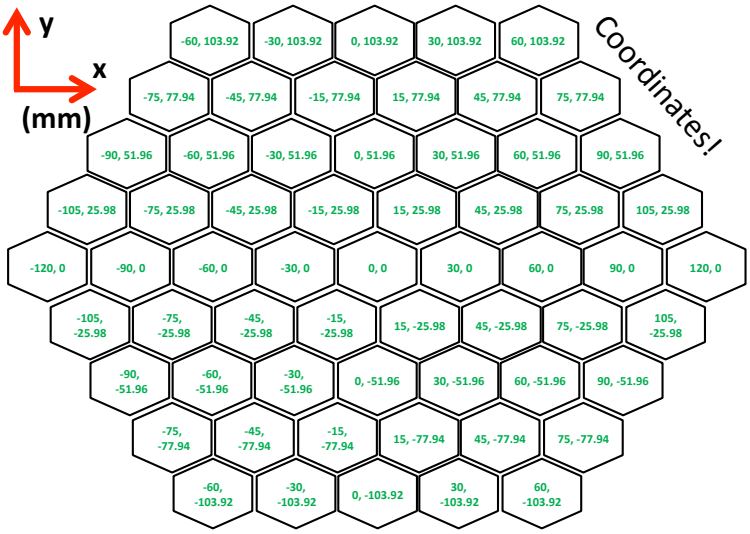

Figure. 3.16: The coordinate of the detector

The simulated source and scatterer are rotated by 90 degrees relative to the measurement setup. This causes a 90-degree shift between the measured and simulated modulation curves, but should not affect the final results of MF. For the setups where the instrument is irradiated off-center (irradiation in Ring1, Ring2, Ring3 or Ring4), the simulated source position is shifted in a direction offset by 90 degrees relative to the direction of the shift in the measurement. This causes any simulated 360-degree component to be shifted by 90 degrees relative to its measured counterpart. However, this should not affect the final results.

As expected, the modulation factor increases with increasing separation between the scattering site and the absorption site, due to the improved angular resolution. On the other hand, the number of events decreases. In the simulation, when irradiating the central unit and requiring scattering in Ring1,Ring 2, Ring3 or Ring4, the number of events decrease with increasing distance from the central unit to the scattering point, as expected. For the measurement, the number of events is essentially unchanged when irradiating the central unit and scattering in Ring3 or in Ring4. This is probably due to the fact that there are more PDCs in Ring4 than in Ring3. The number of events per PDC decreases, as expected. MFs of the event selections of CenterIrradiating CenterScattering Ring1, Ring2, Ring3 or Ring4 Absorption are roughly consistent between ground calibration and Geant4 simulation. However, there are large difference between them in the event selections of CenterIrradiating "All-2hit" and CenterIrradiating Ring1Scattering AnyAbsorption, as entries.

Table. 3.5: The list of parameters of the modulation curves of the ground calibration and the Geant4 simulation

Center Irradiating polarized gamma-ray	Ground calibration			Geant4 simulation		
	Entries	MF (%)	Ratio of entries (%)	Entries	MF (%)	Ratio of entries (%)
All-2hit	148565	22.2±0.59	328.8	14220	31.4±1.16	154.0
CentreCentral	45184	34.7±0.66	100.0	9234	38.7±1.4	100.0
CenterScatteringRing1Absorption	23115	28.0±0.95	51.16	4237	33.1±2.2	45.88
CenterScatteringRing2Absorption	10534	40.0±1.3	23.31	2415	43.7±2.9	26.15
CenterScatteringRing3Absorption	7078	48.1±1.6	15.66	1687	47.1±3.6	18.27
CenterScatteringRing4Absorption	4457	49.9±2.1	9.86	1016	32.3±5.1	11.00
Ring1ScatteringAnyAbsorption	40267	9.7±0.8	89.12	2809	33.4±2.7	30.42
Ring2ScatteringAnyAbsorption	18648	10.1±2.6	41.27	1108	19.8±4.9	12.00
Ring3ScatteringAnyAbsorption	22234	21.1±5.7	49.21	664	11.6±6.3	7.19
Ring4ScatteringAnyAbsorption	22232	15.1±14.6	49.20	351	7.5±8.5	3.80

"new" background	Ground calibration		Background-subtracted ratio
	Entries	Ratio of entries (%)	of the ground calibration (%)
All-2hit	9902	126.2	207.63
CentreCentral	191	2.43	100.00
CenterScatteringRing1Absorption	130	1.66	50.74
CenterScatteringRing2Absorption	25	0.32	23.57
CenterScatteringRing3Absorption	20	0.25	15.79
CenterScatteringRing4Absorption	16	0.20	9.90
Ring1ScatteringAnyAbsorption	1146	14.61	76.37
Ring2ScatteringAnyAbsorption	1866	23.79	17.92
Ring3ScatteringAnyAbsorption	3158	40.26	9.17
Ring4ScatteringAnyAbsorption	3541	45.14	4.16

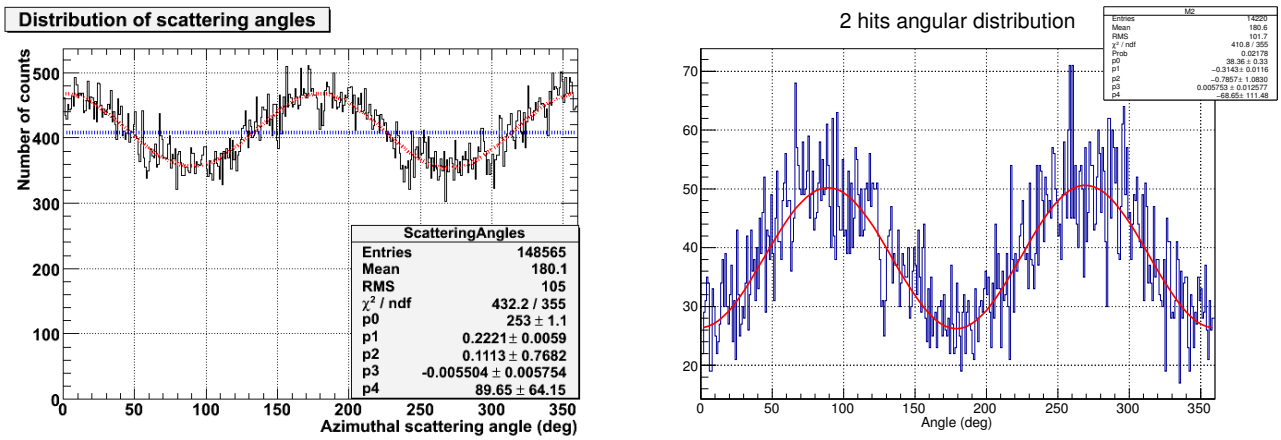

CenterIrradiating AnyScattering AnyAbsorption

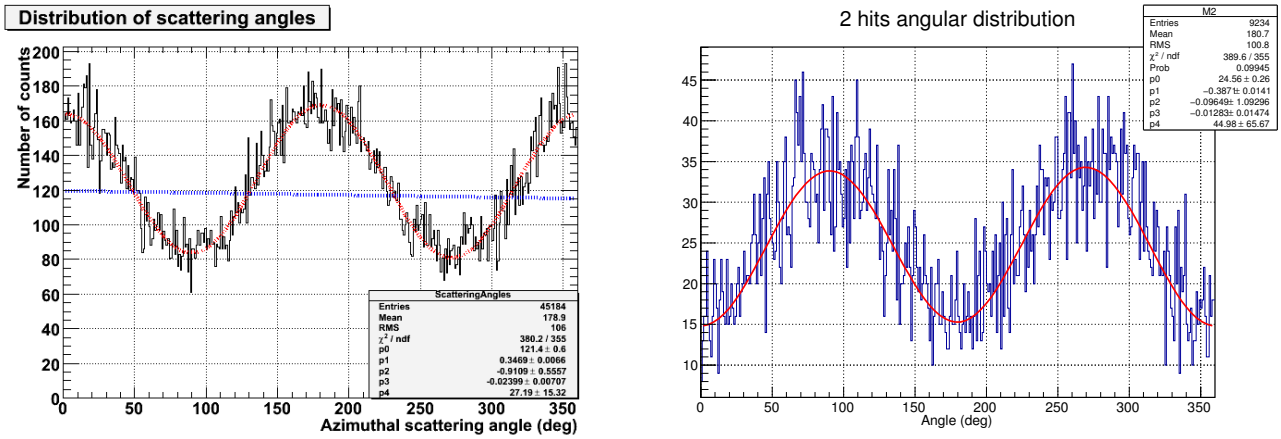

CenterIrradiating CenterScattering AnyAbsorption

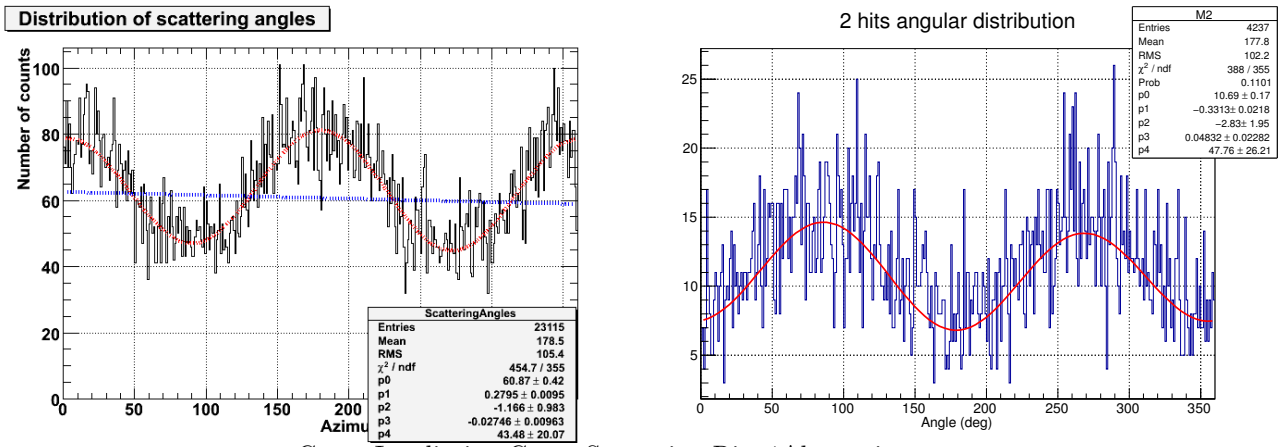

CenterIrradiating CenterScattering Ring1Absorption

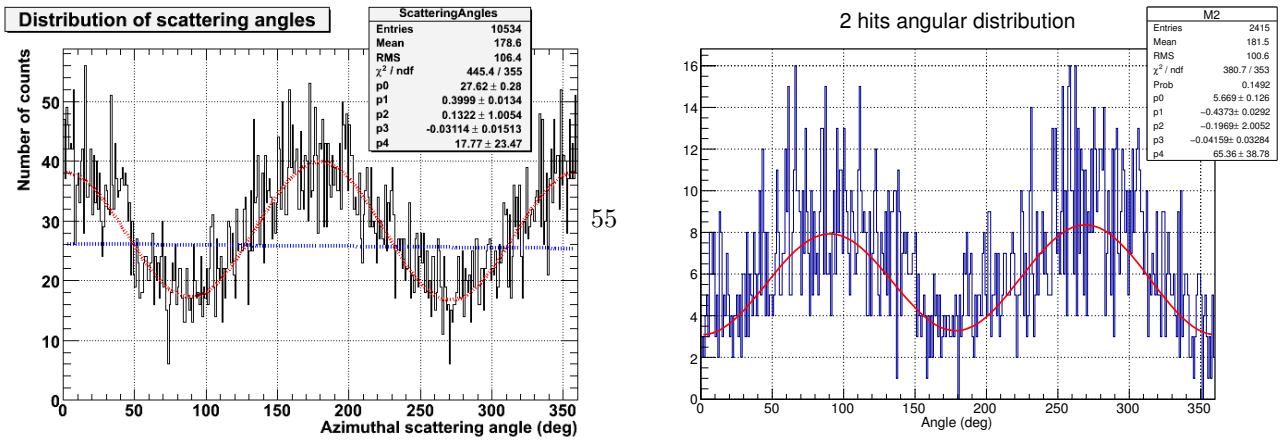

CenterIrradiating CenterScattering Ring2Absorption

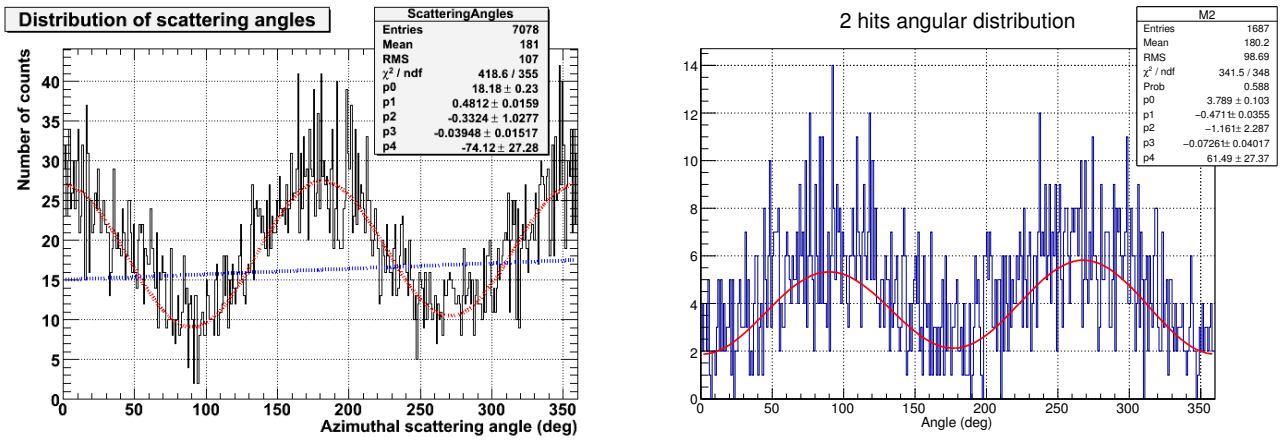

CenterIrradiating CenterScattering Ring3Absorption

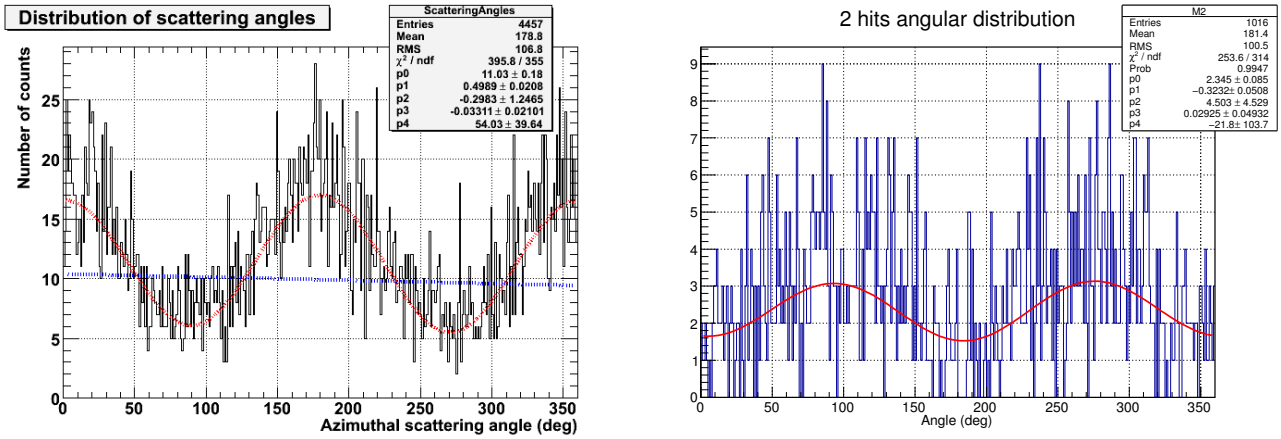

CenterIrradiating CenterScattering Ring4Absorption

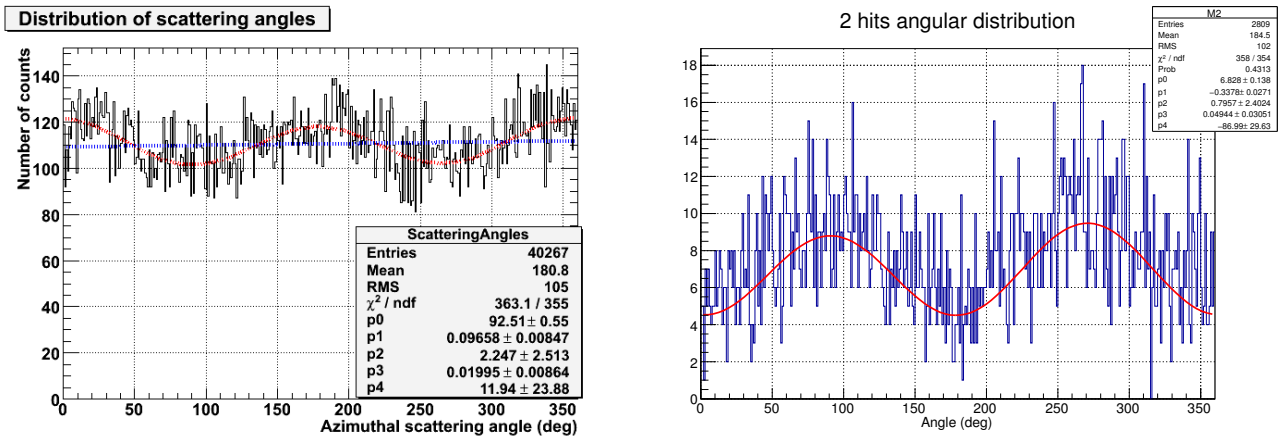

CenterIrradiating Ring1Scattering AnyAbsorption

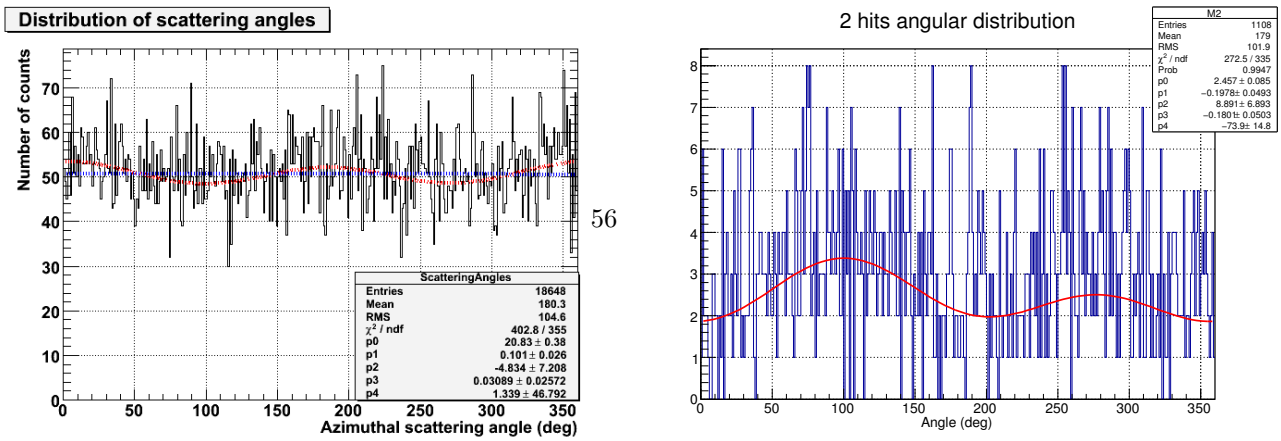

CenterIrradiating Ring2Scattering AnyAbsorption

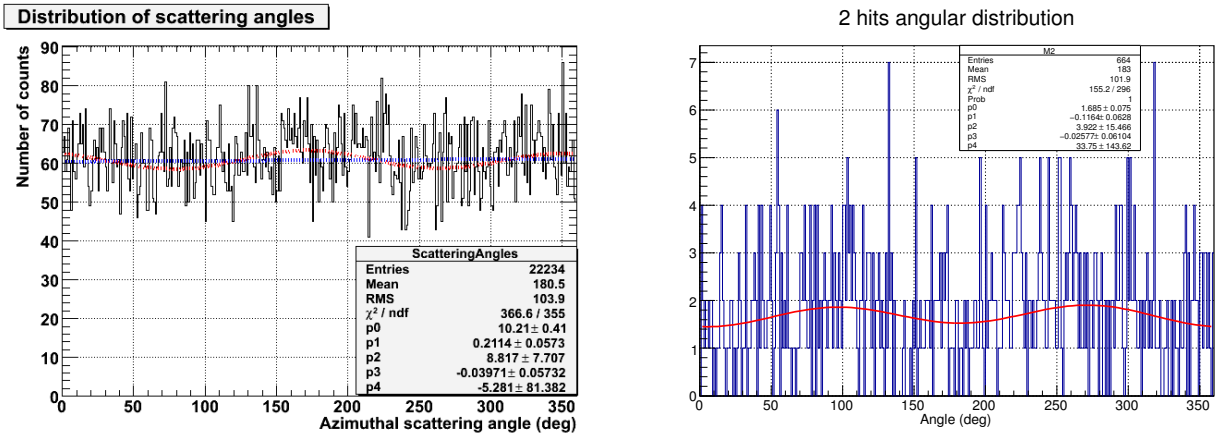

CenterIrradiating Ring3Scattering AnyAbsorption

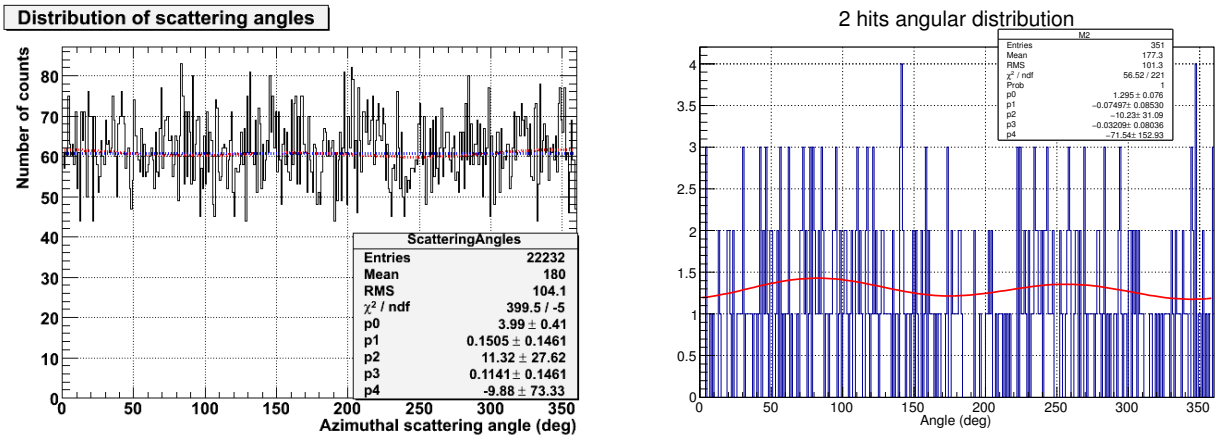

CenterIrradiating Ring4Scattering AnyAbsorption

Figure. 3.17: Comparison the modulation curves between the ground calibration (left) and the Geant4 simulation (right).

3.3.5 Changing threshold

Between ground calibration and Geant4 simulation, there is a factor 2 difference in Ring1 about the entry in the distribution of the interaction site among 61 PDCs. This discrepancy also make the difference of MFs in the event selections of CenterIrradiating "All-2hit" and CenterIrradiating Ring1Scattering AnyAbsorption. After considerations, we suspect that there could be light leakage among PDCs.

To test the possibility if there is light leakage or not, I have analyzed the ground calibration data with raising up the threshold of scattering energy, since the leaking photon should have very low energy and higher threshold might reduce that. Here, I note that in Geant4 simulation, the threshold is corresponding to 10 ADC channel, the same as the hit threshold in the detector.

I used the data of irradiating non-polarized gamma-ray at Center PDC in 2012 with selecting "All-

2hit" event, and ploted the distribution of the scattering site. The results are shown with the different threshold of scattering energy (Fig. 3.18). It shows that the number of events in Ring1 is getting small more efficiently than other Ring, and threshold of 60 ADC channel (corresponding to ∼5 keV) is roughly consistent with Geant4 simulation (Table 3.6). Specially, the deviation between Jiro and other PDCs in Ring1 becomes small.

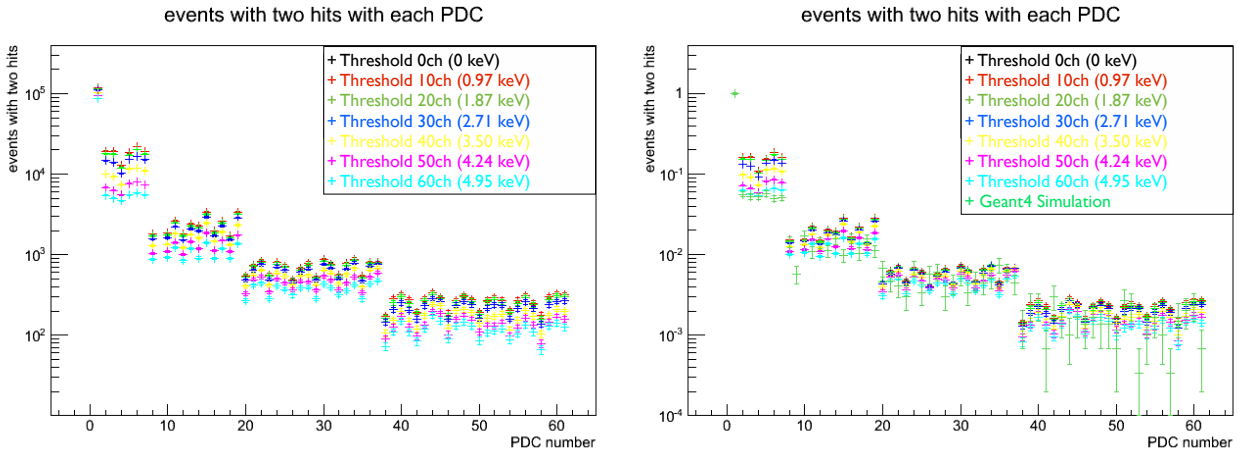

Figure. 3.18: The distribution of the interaction site among 61 PDCs with raising up the threshold of the scattering energy from 0 to 60 ADC channel, corresponding from 0 to 4.95 keV. Left: The raw data. Right: The normalized at the central PDC.

Table. 3.6: Entry ratios of each Ring with raising up the threshold of the scattering energy from 0 to 60 ADC channel, corresponding from 0 to 4.95 keV.

Threshold	Center	Ring1	Ring2	Ring3	Ring4
0 ch (0 keV)	1	0.156	0.0197	0.00592	0.00224
10 ch (0.97 keV)	1	0.156	0.0197	0.00592	0.00224
20 ch (1.87 keV)	1	0.148	0.0191	0.00581	0.00214
30 ch (2.71 keV)	1	0.130	0.0183	0.00563	0.00197
40 ch (3.50 keV)	1	0.100	0.0166	0.00530	0.00167
50 ch (4.24 keV)	1	0.0740	0.0141	0.00478	0.00146
60 ch (4.95 keV)	1	0.0610	0.0122	0.00423	0.00132
Geant4 Simulation	1	0.0533	0.0128	0.00532	0.00169

I have also analyzed two data sets with making spectra between scattering and absorption sites, and their 2-D histogram with several combinations of the threshold. One data set is irradiating non-polarized gamma-ray at Center PDC, and I plotted the spectra with the scattering site of one PDC in Ring1 and absorption site of any PDC (Fig. 3.19). The another is irradiating non-polarized gamma-ray at Center PDC with the scattering site of Center PDC and absorption site of one PDC in Ring1 (Fig. 3.20). Both are plotted with the thresholds from 0 to 60 ADC channels. In these 2-D histograms, the horizontal axis shows energy of the scattering site, and the vertical axis shows energy of the absorption site. Here, I

show only 0 and 60 ADC channel for Jiro (PDC number =3) and Hicks (PDC number = 5), and others are in Appendix B.

In figure 3.19, there is a large difference around the events of the scattering site with a few keV and the absorption site with 40–80 keV, between two PDCs with threshold of 0 ADC channel, while it decreases with threshold 60 ch. It might suggest that there is light leakage next (Ring1) to the irradiation position (Center) and higher threshold (∼5 keV) can reduce it.

In figure 3.20, there is less difference between thresholds of 0 and 60 ADC channels. It suggests that there are no significant affects at the irradiated position (Center).

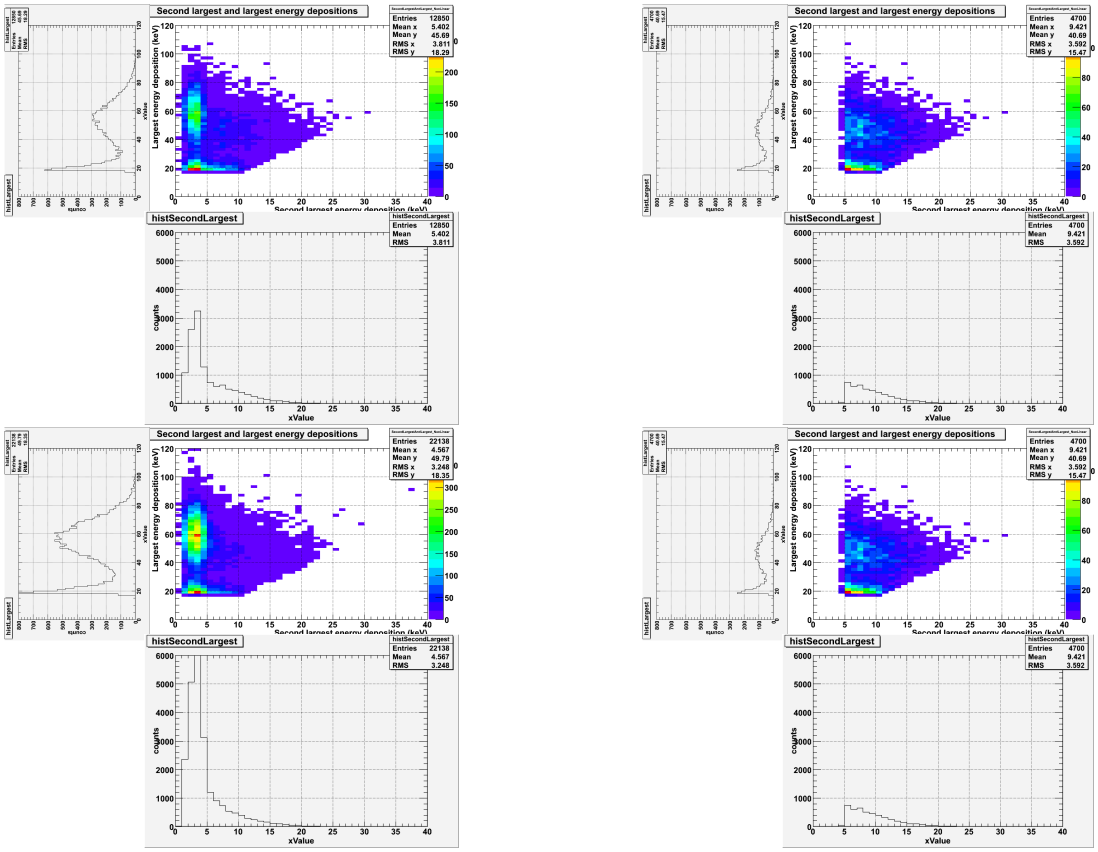

Figure. 3.19: 2-D histogram and the projections (i.e., the energy spectra) with the threshold 0 and 60 ADC channel. The data are irradiating non-polarized gamma-ray at Center PDC. Scattering site is one PDC in Ring1 and absorption site is any PDC with threshold 0 ADC channel and 60 ADC channel. Upper left: Scattering site is Jiro with threshold of 0 ADC channel. Upper right: Scattering site is Jiro with threshold of 60 ADC channel. Lower left: Scattering site is Hicks with threshold of 0 ADC channel. Lower right: Scattering site is Hikcs with threshold of 60 ADC channel.

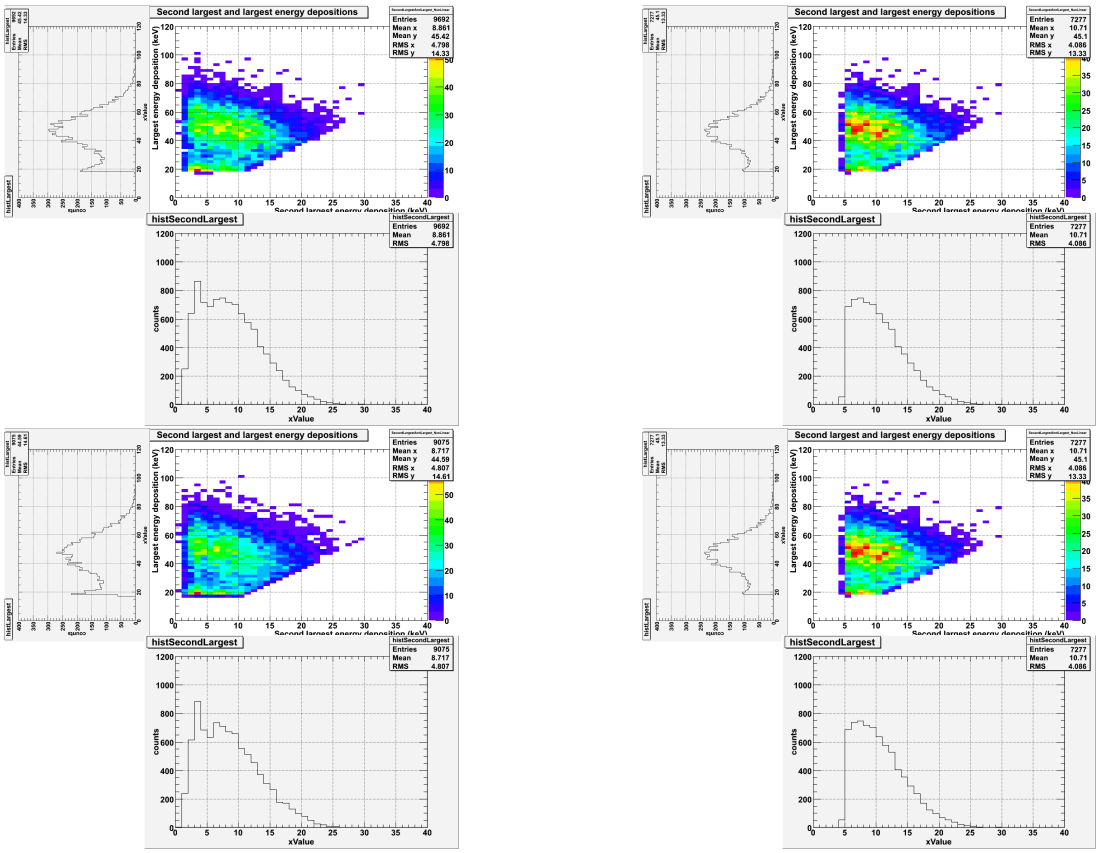

Figure. 3.20: The same as figure 3.19 but for the two selections: (1) the scattering site is Barret (Center) and absorption site is Jiro (Ring1), and (2) the scattering site is Barret (Center) and absorption site is Hicks (Ring1).

3.3.6 Summary and future works for the ground calibration

We have carried out ground calibration for over 150 hours. There are results of ground calibration about gain of each PDC, angular response, time resolution, the distribution of the interaction site among 61 PDCs, and modulation factor. The gain of each PDC, angular response, and time resolution are analyzed by other PoGOLite members and match the requirements. The distribution of the interaction site among 61 PDCs has the factor 2 difference in Ring1 between ground calibration and simulation, while the other Ring is consistent. It is confirmed that the systematical error of MF is better than $\sim$1% with polarized gamma-rays irradiation at the central PDC. MFs of the ground calibration is consistent with the Geant4 simulation, except for those including the events of Ring1 scattering. The differences might suggest that there are effects of the light leakage between PDC, and the light leakage can be reduced with the higher threshold.

For the future works, we need ground calibration tests, such as irradiating ^{137}Cs at bottom BGO, which emits more number of photons, to confirm this problem. After investigating this issue in more detail, we will construct a new simulator and re-calibrate the MF of the PoGOLite instrument.

Chap.4 Analysis of 2013-flight data

While in the line-of-sight of Esrange communications, the gondola were operated through the high bandwidth E-Link system which offers ∼1 Mbit/sec full duplex. E-Link stations are located at Esrange in Sweden and the Andoya rocket range in Norway (Fig. 4.1). E-Link is available in the yellow and red circles, and outside of these circle, we utilize the Iridium communications. E-Link communications were lost at ∼0100 UT on 13th July. The Iridium data link is much slower than E-Link, with data rates of, at best, ∼1 kbit/s. This means that only a summary of scientific data and housekeeping can be downloaded. A full scientific analysis of the polarimeter data therefore requires recovery of the solid state storage units in the gondola, and finally returned to Royal Institute of Technology at mid-January in 2014. In this chapter, preliminary results based on data downlinked over E-Link are presented.

Figure. 4.1: The trajectory of PoGOLite after the launch from Esrange. The tendency for the balloon to follow a Northerly track is seen in the days prior to termination. The launch took place from Esrange on 12th July at 0818 UT and the gondola landed in Siberia on July 25th at 0015 UT. In the yellow and red circles, E-Link communications are available.

Altitude In figure 4.2, the altitude of PoGOLite during the ascent is shown. In this region, the altitude is at most ∼40 km and over the requirement of 38 km.

Number of hits in different units of the detector Figure 4.3 is an example of the number of hits in different units of the detector during flight. The unit number of 0–60 is corresponding to PDC, 62–91 is corresponding to SAS, 93 is corresponding to LiCAF (neutron scintillator). For SAS, the unit number of 62–84 is connected to FADC 9–11 and, 85–91 is connected to FADC 12, which the LiCAF is

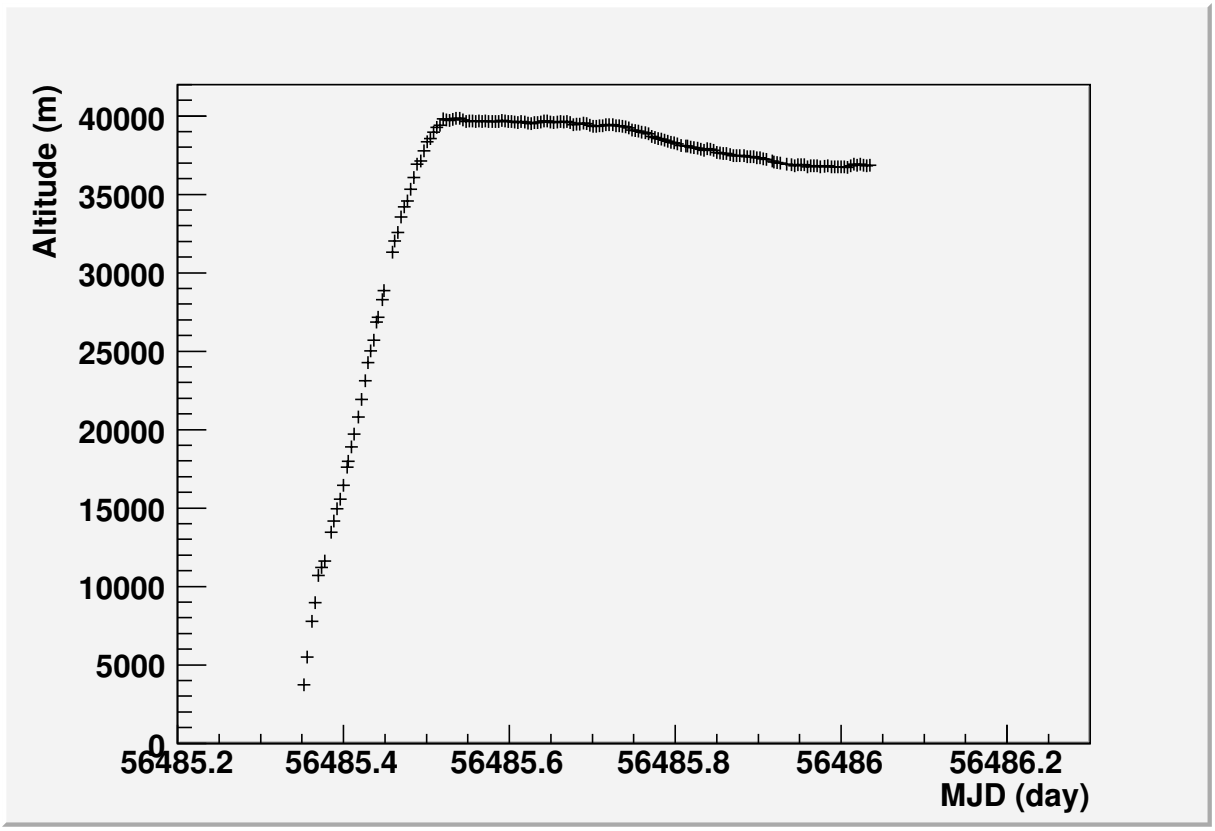

Figure. 4.2: The altitude of the PoGOLite balloon. From the launch to the end of E-Link region.

also connected to and has a special trigger function to obtain neutron events. This function issues more triggers, and the units of 85–91 have a large number of events than the other SASs. The channels on FADC 12 are always read out when there is a hit in the neutron scintillator, which means that this board can cause triggers even without the involvement of the DIO board.

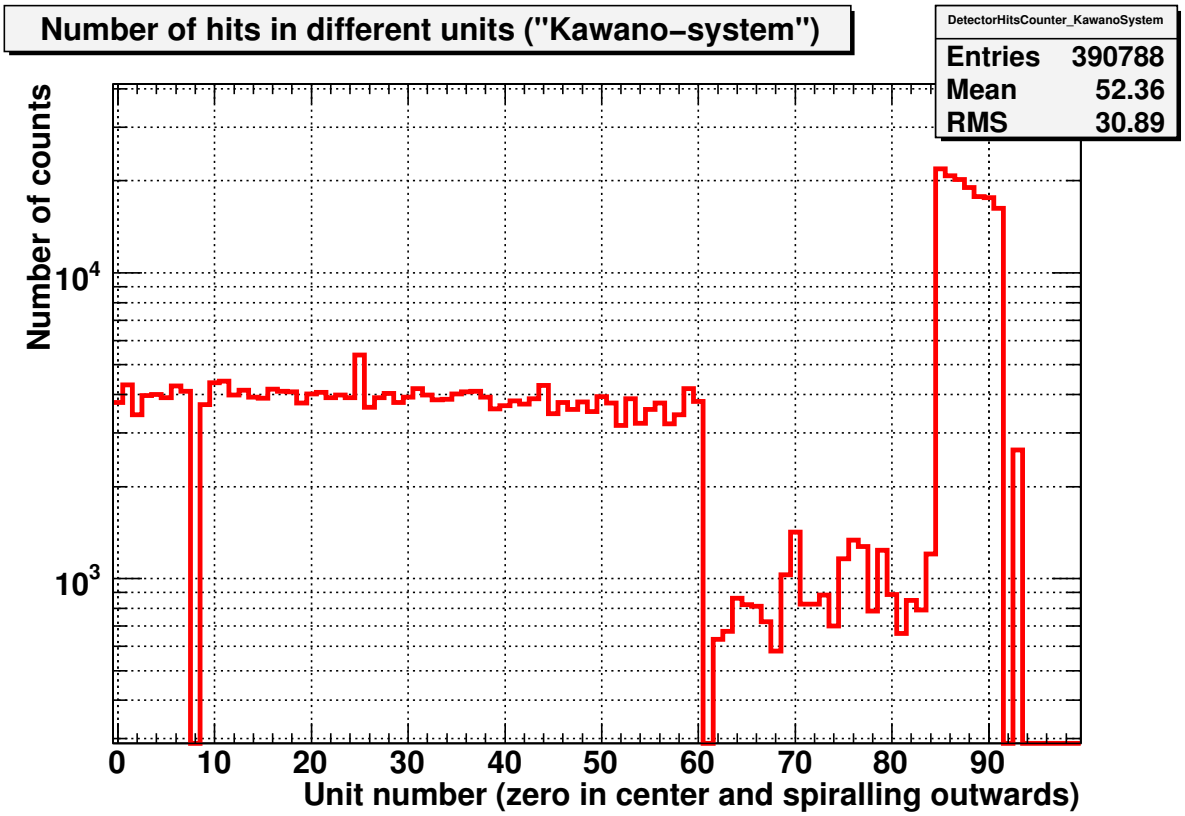

Figure. 4.3: An example of the number of hits in different units of the detector during the flight. The exposure time is 300 sec.

Counting rates In figure 4.4, the average counting rate in SAS is shown. The counting rate increases during ascent and displays a maximum. In the top of this figure, there is a flare around 56485.9061226852–56485.910162037. It seems to be a solar flare or a gamma-ray burst, but it is dismissed because there is no observation/detection with any satellite at that time.

In figure 4.5, the average counting rate in one PDC unit is shown. The counting rate also increases during ascent and displays a maximum. In this figure, we can see different behavior with different Ring. The averaged count rate of Ring2 shows the highest rate. Ring1, Ring3, Center and Ring4 follow it. It might be caused that Ring4 locates neighbor to SAS and is covered most efficiently from gamma-ray or cosmic-ray background events. Center is the farthest away from outside and less affected by neutron background events stopped by the polyethylene shield and outer PDCs.

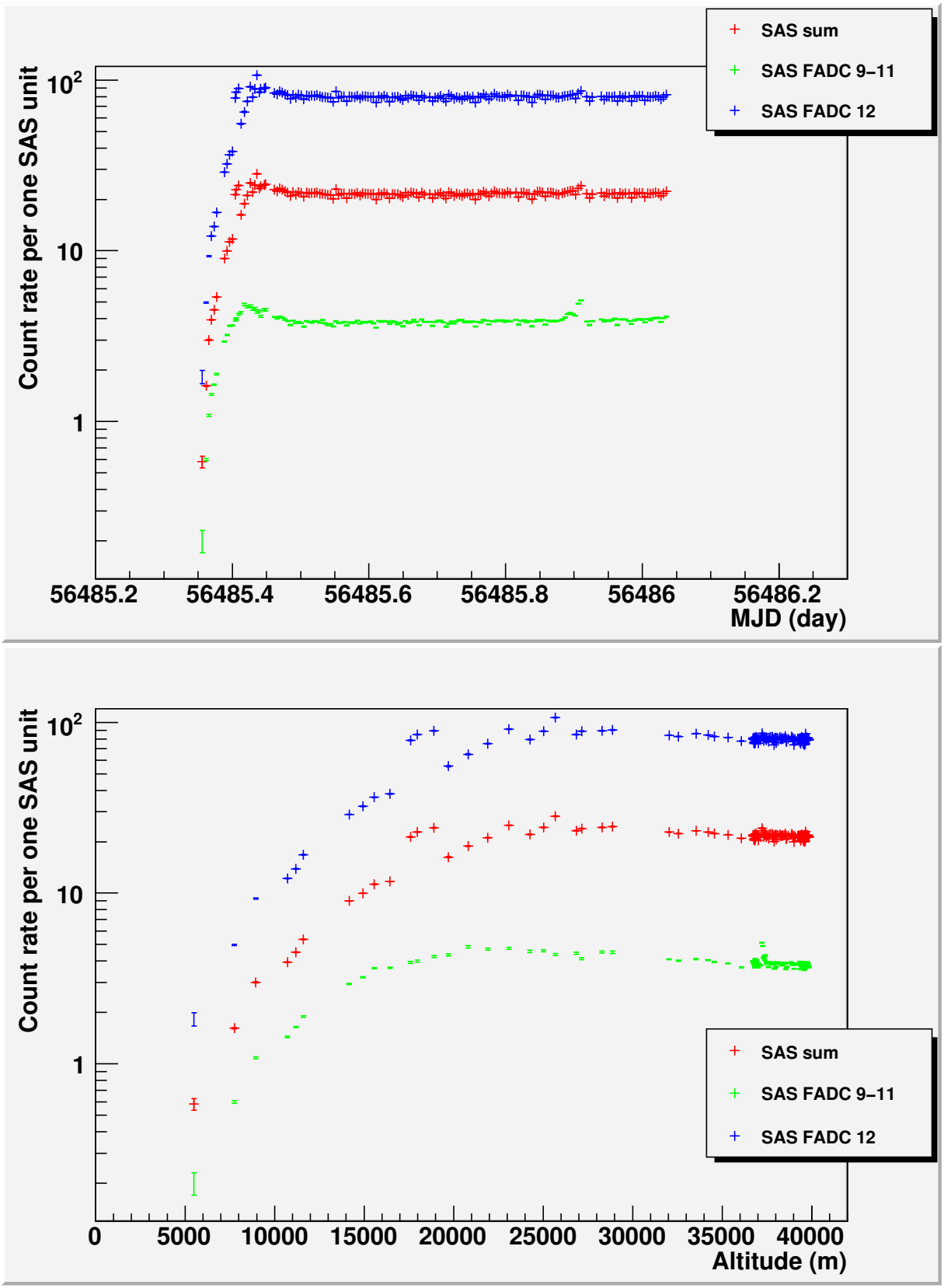

Figure. 4.4: The count rate per one SAS unit . Upper: The plot as a function of time (MJD). Lower: The plot as a function of altitude.

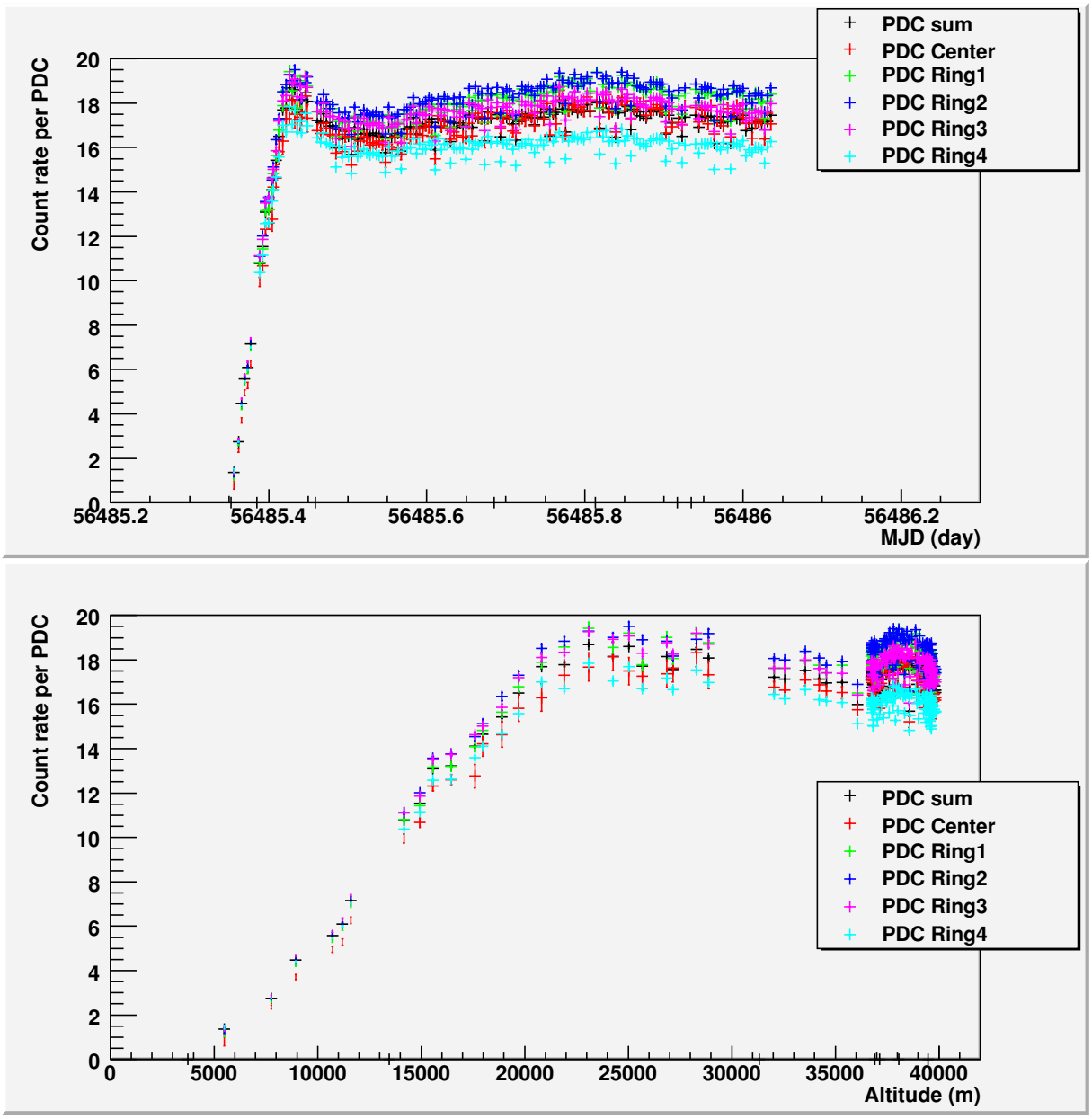

Figure. 4.5: The count rate per PDC. Upper: The plot as a function of time (MJD). Lower: The plot as a function of altitude.

The counting rate for 2-hit events is shown in figure 4.6 and 4.7. In figure 4.6, only the scatting sites are shown, and in figure 4.7, only absorption sites are shown. In these figures, the event rates are so low that there is no clear different among the Rings. Detail comparison of 2-hit event is in AppendixC.

The counting rate for LiCAF event is shown in figure 4.8. Since LiCAF and BGO crystal are connected together as the phoswich detector, this event is including both LiCAF and BGO crystal events. To investigate the ratio of figure 4.8, I have operated the following detail analysis.

Figure 4.9 left is an example of "Fast" and "slow" outputs of detector cell of LiCAF. Since LiCAF and BGO crystal have different decay time, ∼1200 ns for LiCAF and ∼300 ns for BGO crystal, there are two branches: one corresponding to events detected by LiCAF and another for events by BGO crystal. Figure 4.10 right is projection of the left and fitted with detected by gauss function. The separated LiCAF and BGO event rates are shown in figure 4.10.

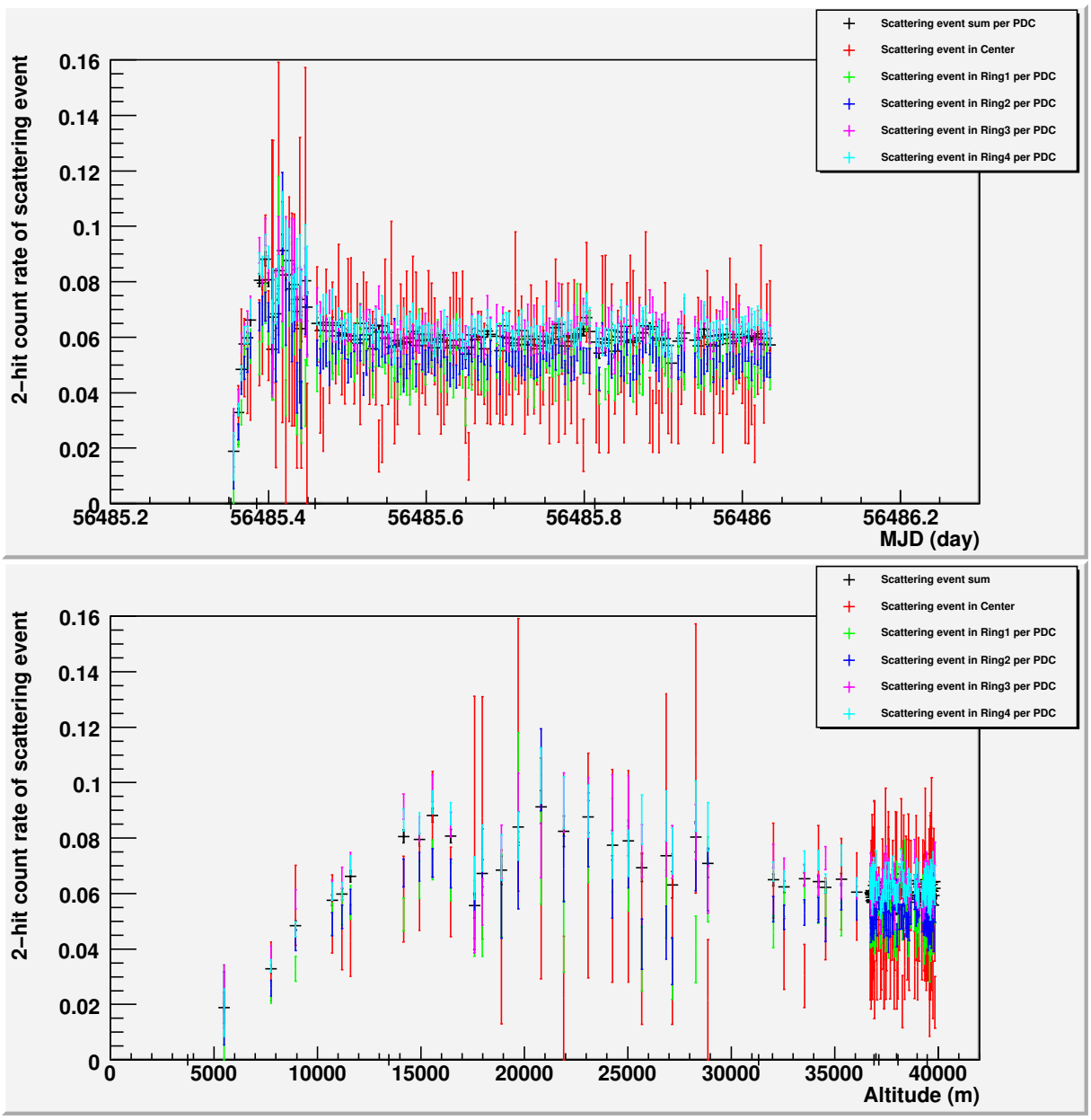

Figure. 4.6: The 2-hit count rate per PDC for scattering site. Upper: The plot as a function of time (MJD). Lower: The plot as a function of altitude.

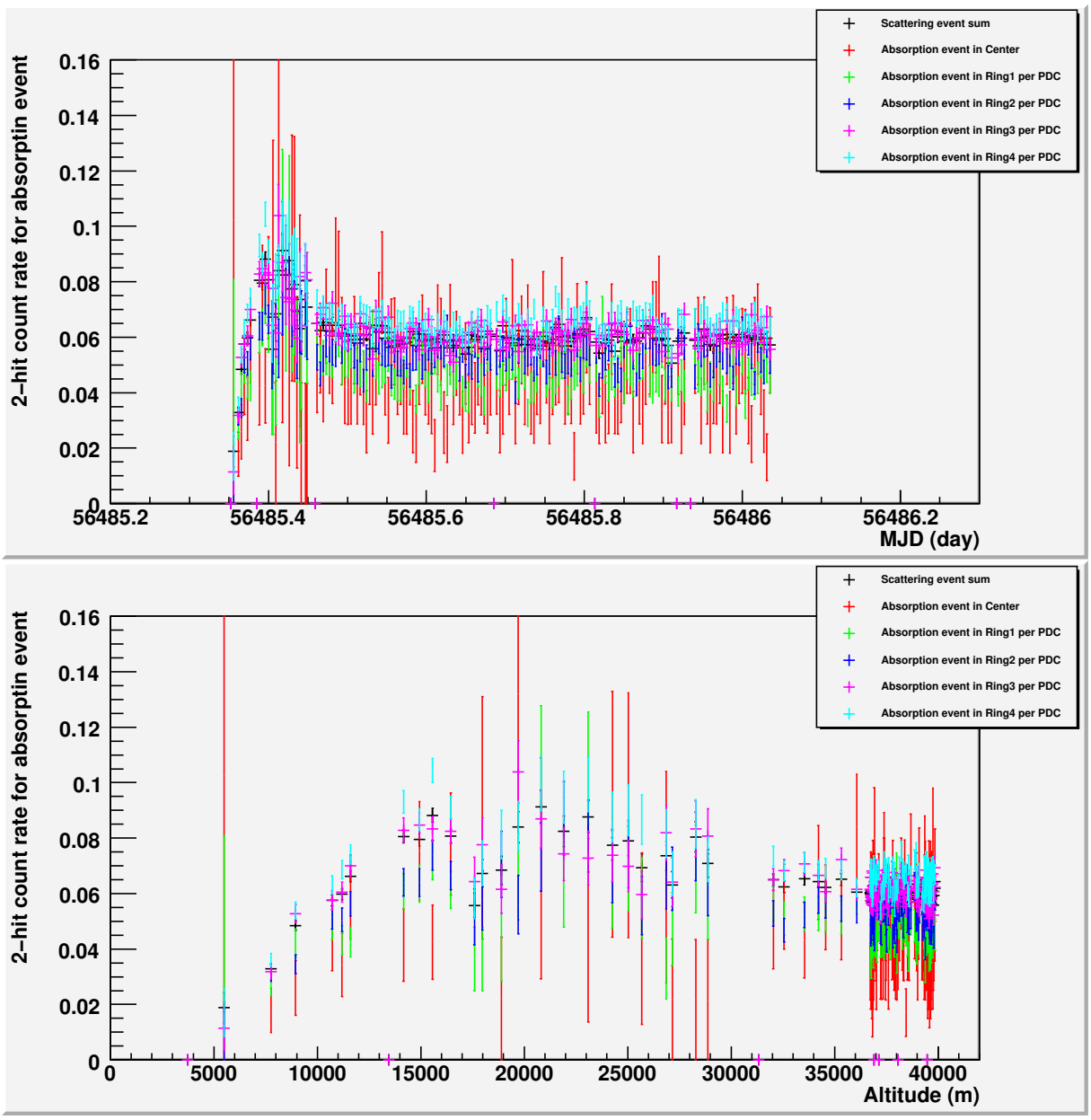

Figure. 4.7: The 2-hit count rate per PDC for absorption site. Upper: The plot as a function of time (MJD). Lower: The plot as a function of altitude.

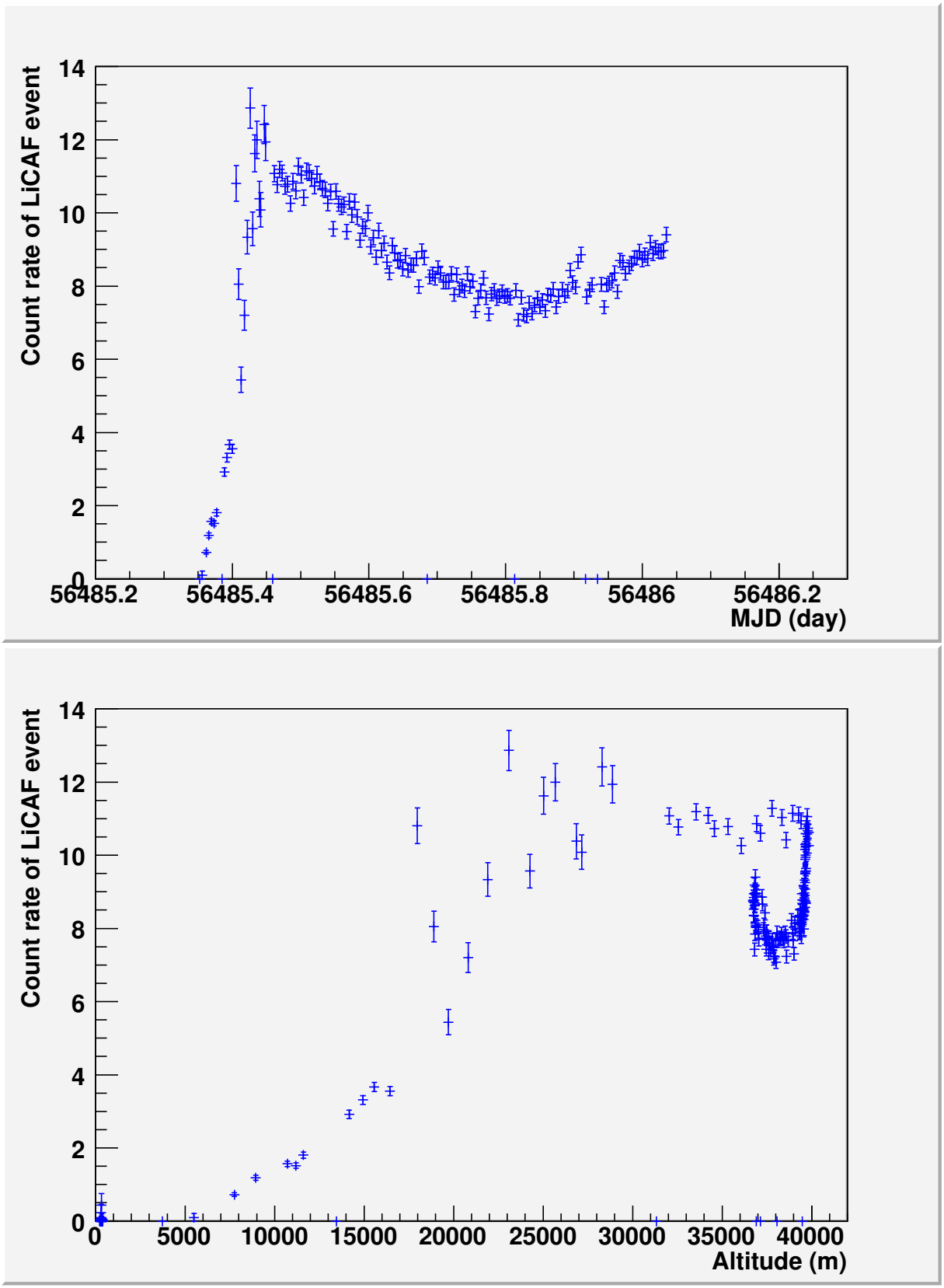

Figure. 4.8: The LiCAF count rate. Upper: The plot as a function of time (MJD). Lower: The plot as a function of altitude.

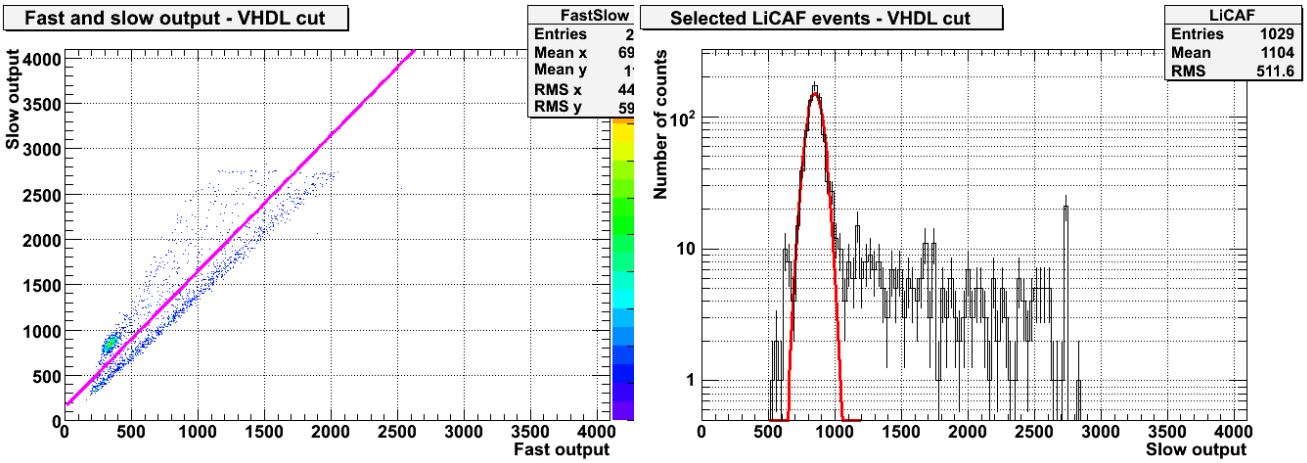

Figure. 4.9: Left: An example of "Fast" and "slow" outputs of detector cell of LiCAF. Right: Projection of the left figure after selecting only LiCAF events and fitted with Gauss function.

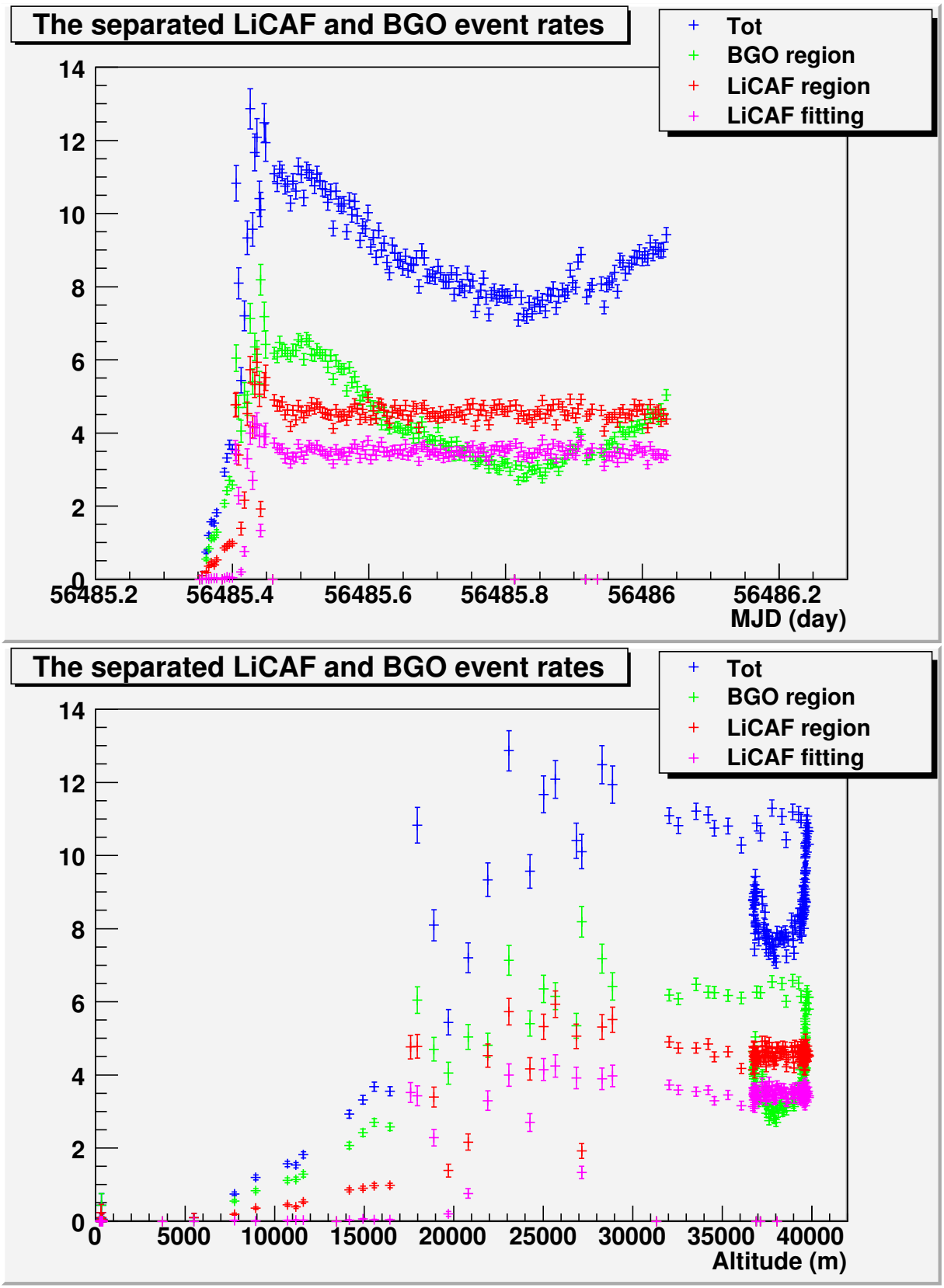

Figure. 4.10: Event rates of LiCAF and BGO in the neutron detector. Blue: Total, Green: Events of BGO crystal, Red: Events of LiCAF region, Magenta: Events in the Gauss function. Upper: The plot as a function of time (MJD). Lower: The plot as a function of altitude.

Chap.5 Summary and future works

In 2012 and 2013, we have operated the ground calibration over 150 hours, and studied the capability of the detector. There are results of the ground calibration about the gain of each PDC, angular response, time resolution, the interaction site distribution of 61 PDCs, and modulation factor. The gain of each PDC, angular response, and time resolution are analyzed by the other members and confirmed they achieve the requirements. It is confirmed that the systematical error of MF is better than $\sim$1% with polarized gamma-rays irradiation at the central PDC. The distribution of the interaction site among 61 PDCs has the factor 2 difference in Ring1 between ground calibration and simulation, while the other Ring is consistent. MFs of the ground calibration is consistent with the Geant4 simulation, except for those including the events of Ring1 scattering. There is a doubt of light leakage in the detector. The light leakage might cause the factor 2 difference of the Ring1 in the distribution of the interaction site among 61 PDCs and lower MF.

For the future works, we need ground calibration tests, such as irradiating ^{137}Cs at bottom BGO, which emits more number of photons, to confirm this problem. After investigating this issue in more detail, we will construct new a simulator and re-calibrate the MF of the PoGOLite instrument. The detail analysis of of flight full-data will be performed after these analyses of the ground calibration.

Appendix A

A.1 Modulation curves with some set up and event selection of the ground calibration

A.2 Comparison of modulation curves between the ground calibration (left) and the Geant4 simulation (right)

CenterIrradiating, ???Scattering, ???Absorption, NonRandomized, 90-270degree, 1440m(2012)

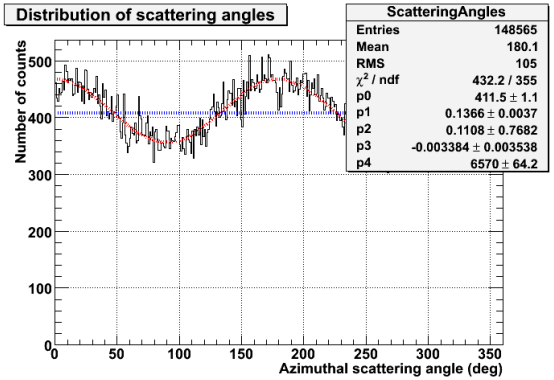

AnyScattering
AnyAbsorption

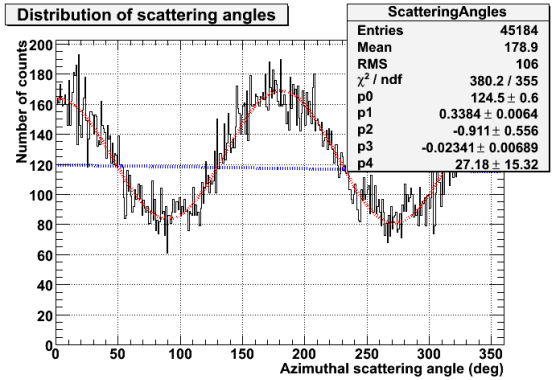

CenterScattering
AnyAbsorption

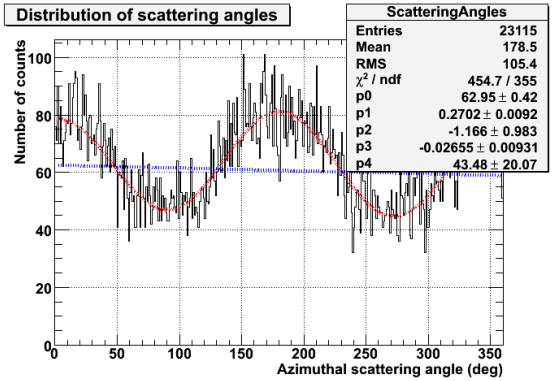

CenterScattering
Ring1Absorption

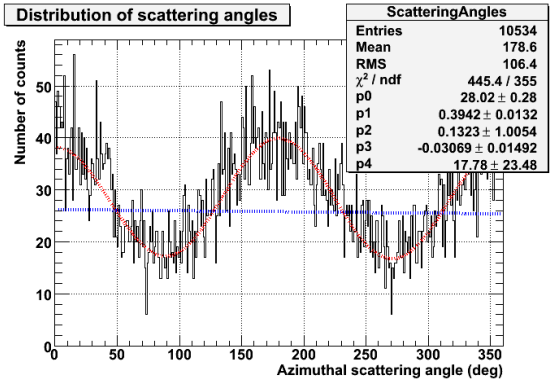

CenterScattering
Ring2Absorption

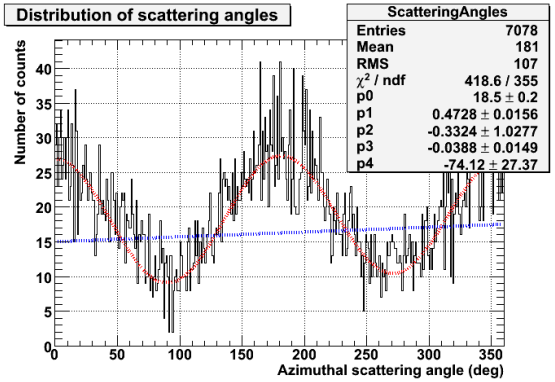

CenterScattering
Ring3Absorption

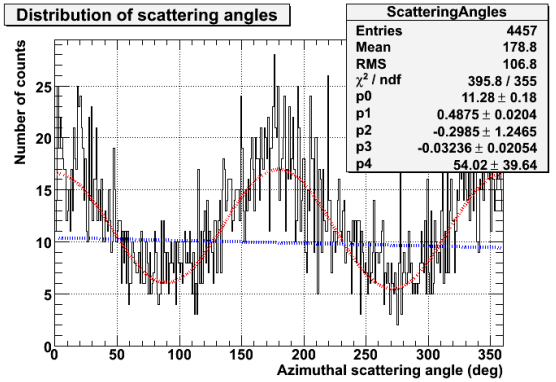

CenterScattering
Ring4Absorption

CenterIrradiating, ???Scattering, ???Absorption, WithRandomized, 90-270degree, 1440m(2012)

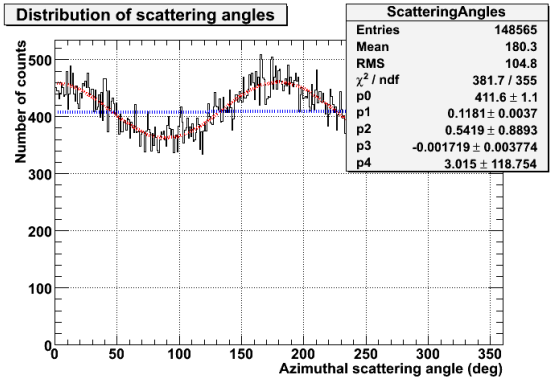

AnyScattering
AnyAbsorption

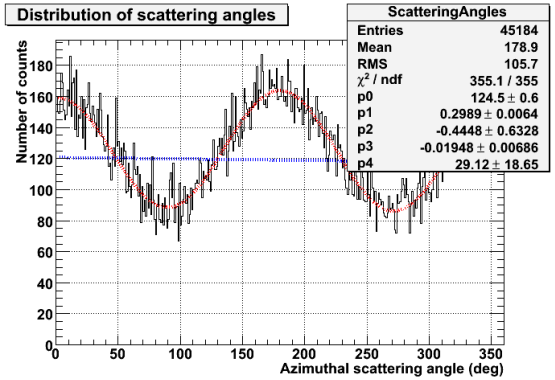

CenterScattering
AnyAbsorption

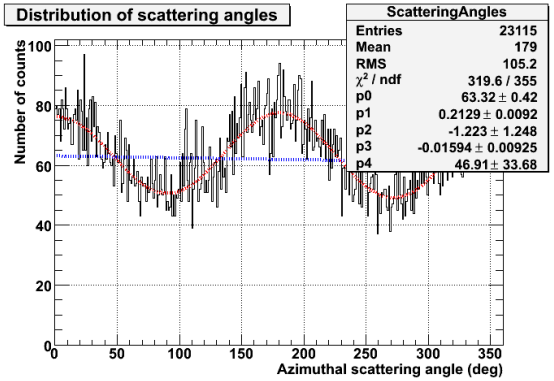

CenterScattering
Ring1Absorption

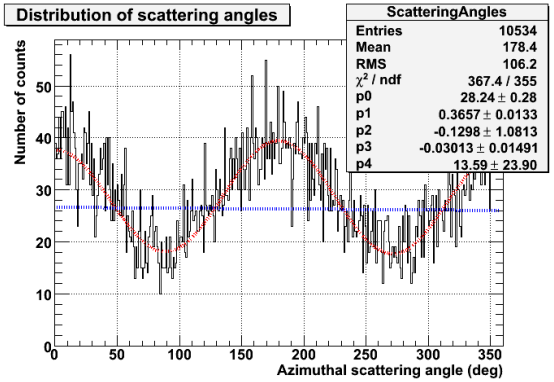

CenterScattering
Ring2Absorption

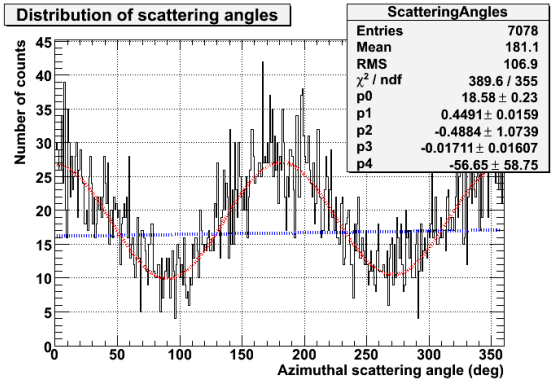

CenterScattering
Ring3Absorption

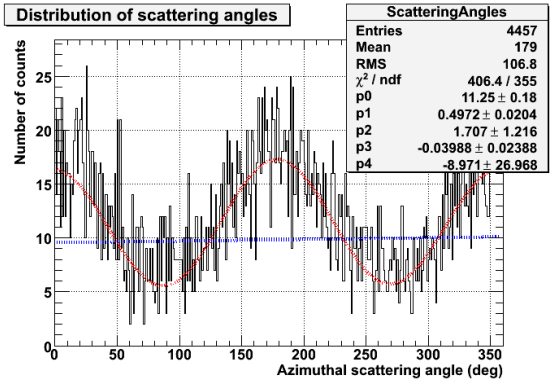

CenterScattering
Ring4Absorption

CenterIrradiating, Ring?Scattering, AnyAbsorption, NonRandomized, 90-270degree, 1440m(2012)

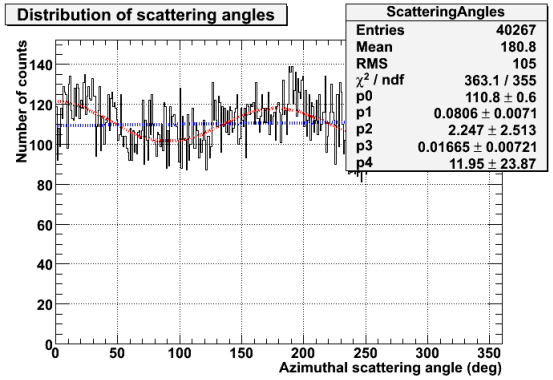

Ring1Scattering
AnyAbsorption

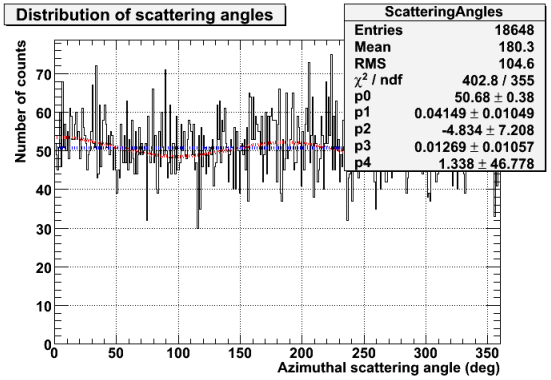

Ring2Scattering
AnyAbsorption

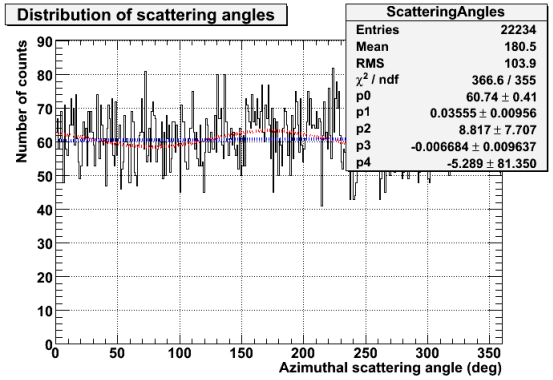

Ring3Scattering
AnyAbsorption

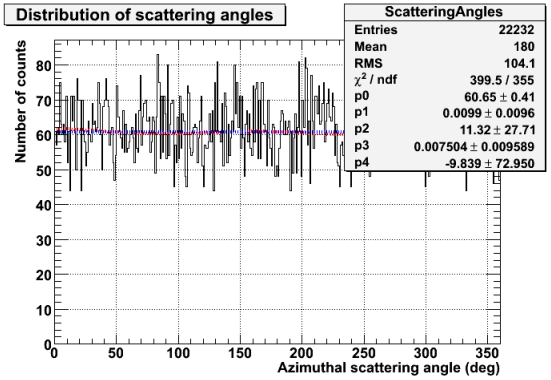

Ring4Scattering
AnyAbsorption

CenterIrradiating, Ring?Scattering, AnyAbsorption, WithRandomized, 90-270degree, 1440m(2012)

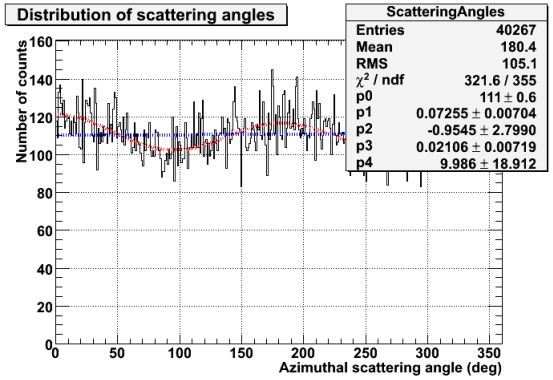

Ring1Scattering
AnyAbsorption

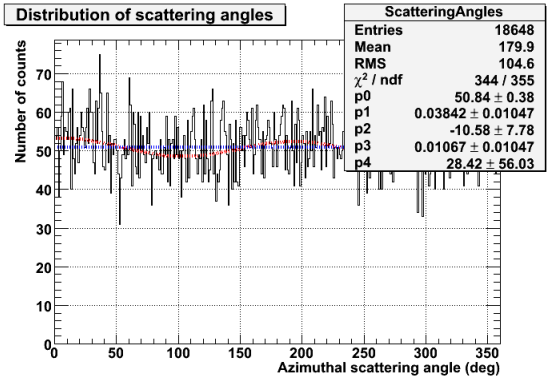

Ring2Scattering
AnyAbsorption

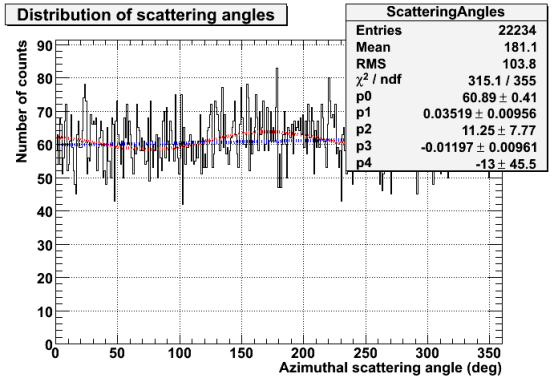

Ring3Scattering
AnyAbsorption

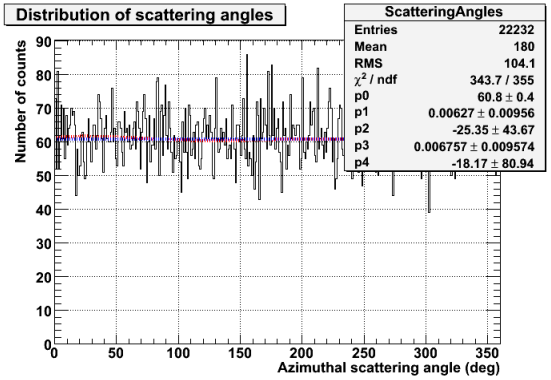

Ring4Scattering
AnyAbsorption

Ring1Irradiating, ???Scattering, ???Absorption, NonRandomized, 90-270degree, 505m(2012)

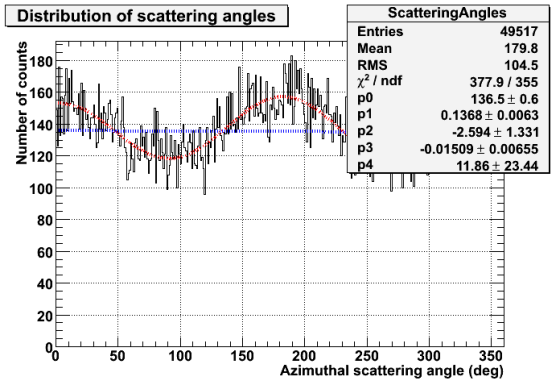

AnyScattering
AnyAbsorption

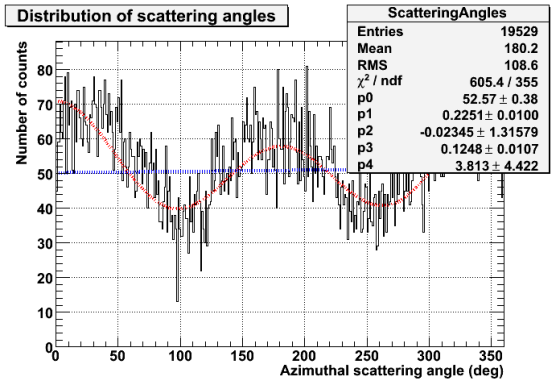

Ring1Scattering
AnyAbsorption

Ring1Irradiating, ???Scattering, ???Absorption, WithRandomized, 90-270degree, 505m(2012)

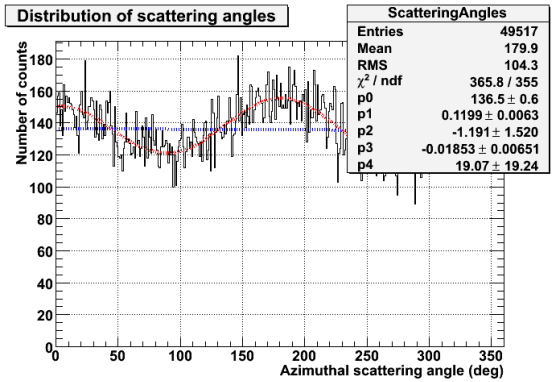

AnyScattering
AnyAbsorption

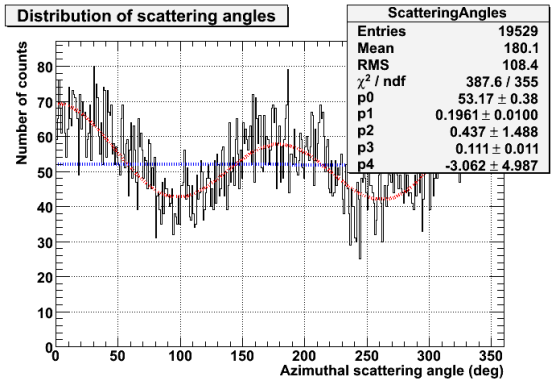

Ring1Scattering
AnyAbsorption

Ring2Irradiating, ???Scattering, ???Absorption, NonRandomized, 90-270degree, 625m(2012)

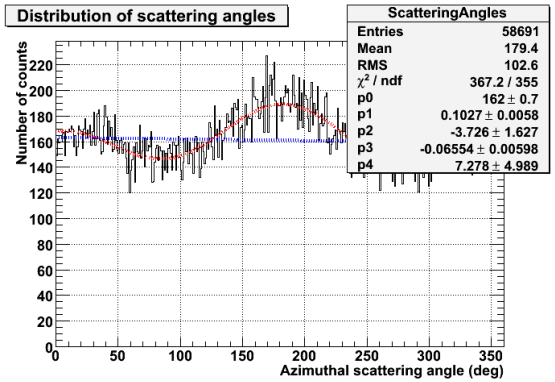

AnyScattering
AnyAbsorption

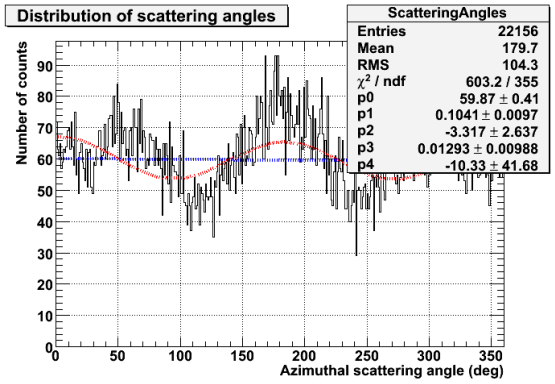

Ring2Scattering
AnyAbsorption

Ring2Irradiating, ???Scattering, ???Absorption, WithRandomized, 90-270degree, 625m(2012)

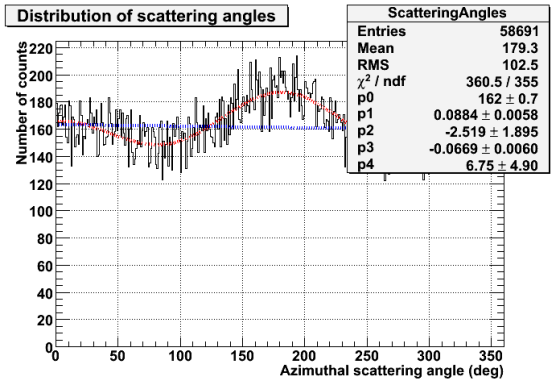

AnyScattering
AnyAbsorption

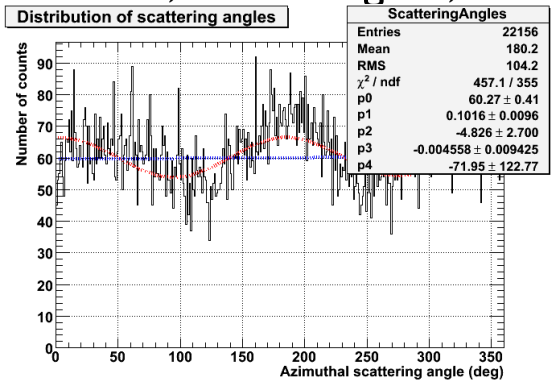

Ring2Scattering
AnyAbsorption

Ring3Irradiating, ???Scattering, ???Absorption, NonRandomized, 90-270degree, 600m(2012)

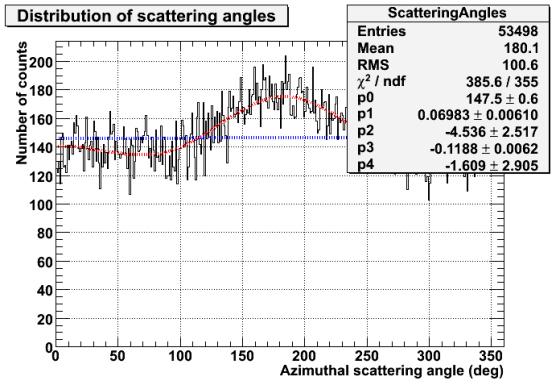

AnyScattering
AnyAbsorption

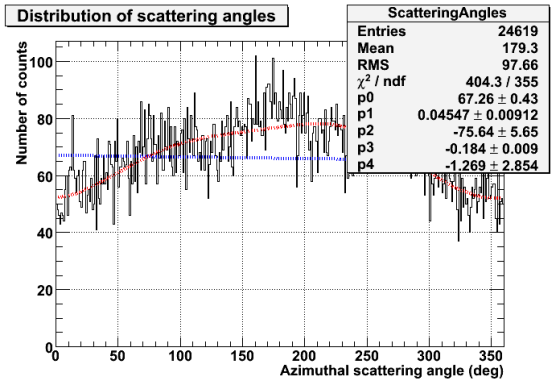

Ring3Scattering
AnyAbsorption

Ring3Irradiating, ???Scattering, ???Absorption, WithRandomized, 90-270degree, 600m(2012)

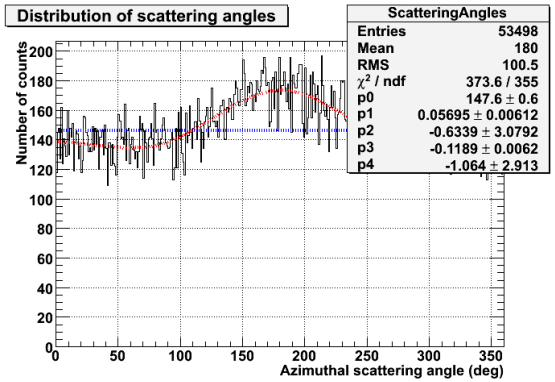

AnyScattering
AnyAbsorption

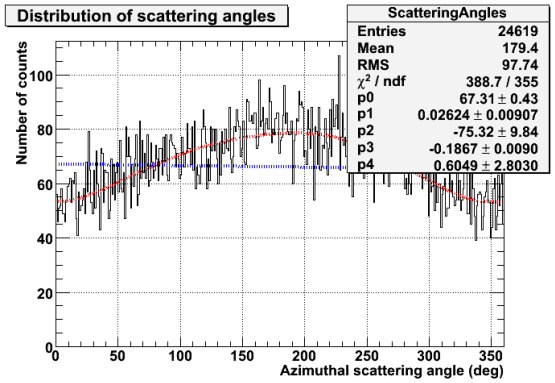

Ring3Scattering
AnyAbsorption

Ring4Irradiating, ???Scattering, ???Absorption, NonRandomized, 90-270degree, 925m(2012)

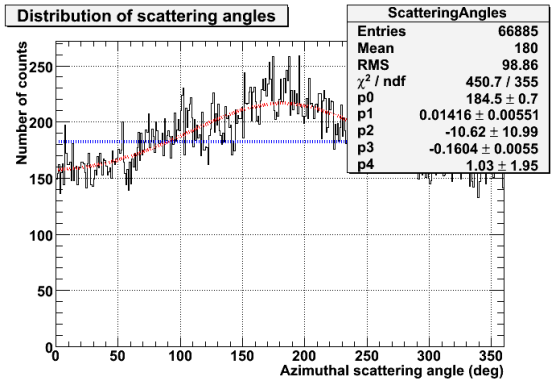

AnyScattering
AnyAbsorption

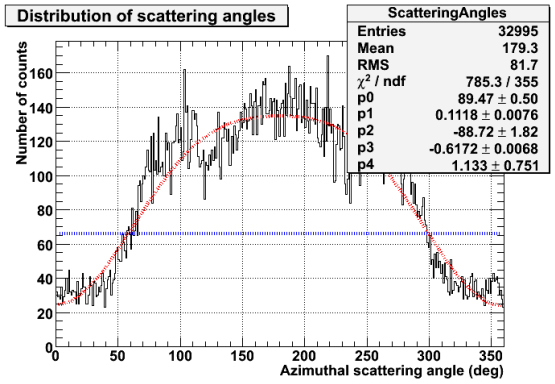

Ring3Scattering
AnyAbsorption

Ring4Irradiating, ???Scattering, ???Absorption, WithRandomized, 90-270degree, 925m(2012)

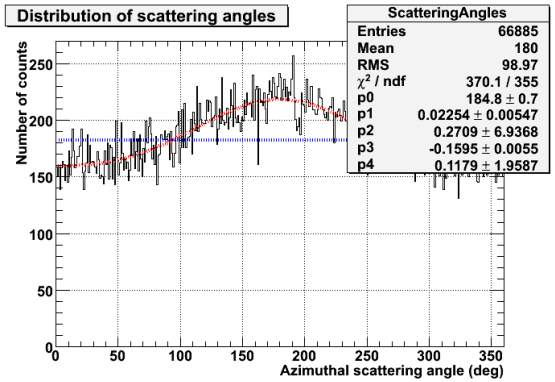

AnyScattering
AnyAbsorption

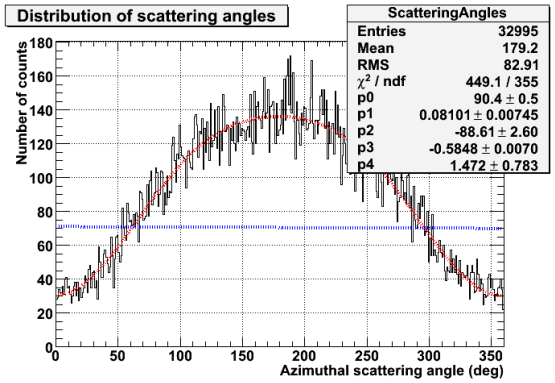

Ring3Scattering
AnyAbsorption

CenterIrradiating AnyScattering AnyAbsorption

The Geant4 simulation

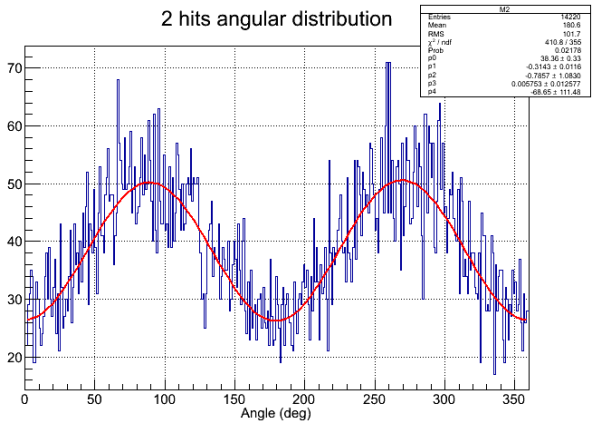

The ground calibration

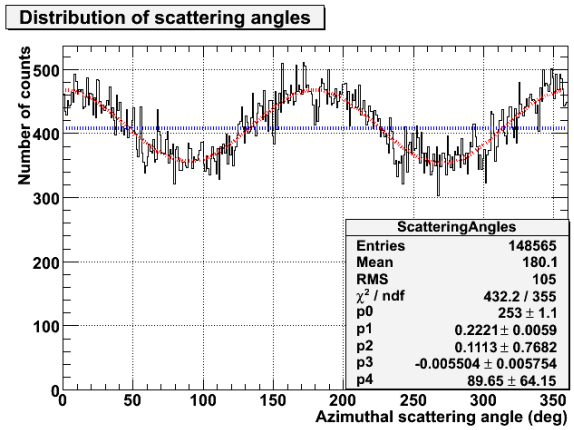

CenterIrradiating CenterScattering AnyAbsorption

The Geant4 simulation

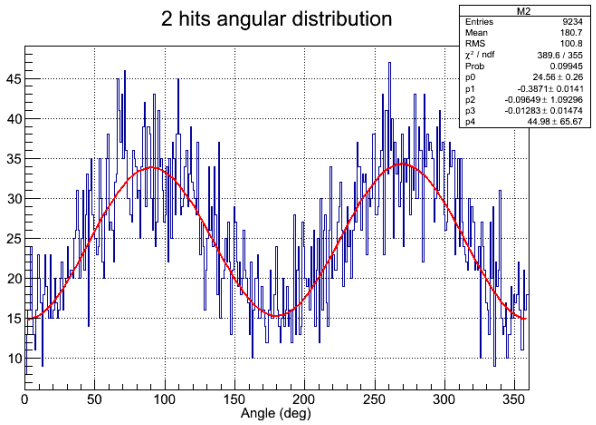

The ground calibration

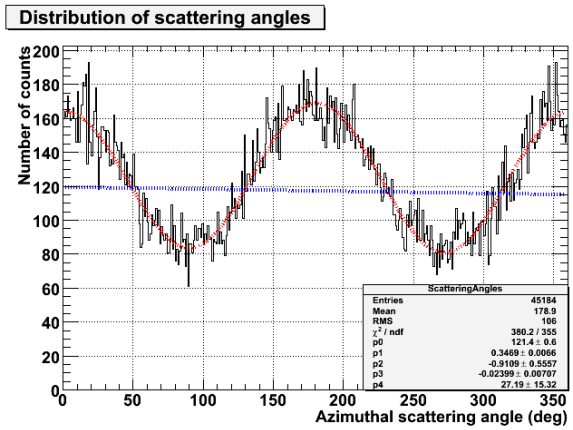

CenterIrradiating CenterScattering Ring1Absorption

The Geant4 simulation

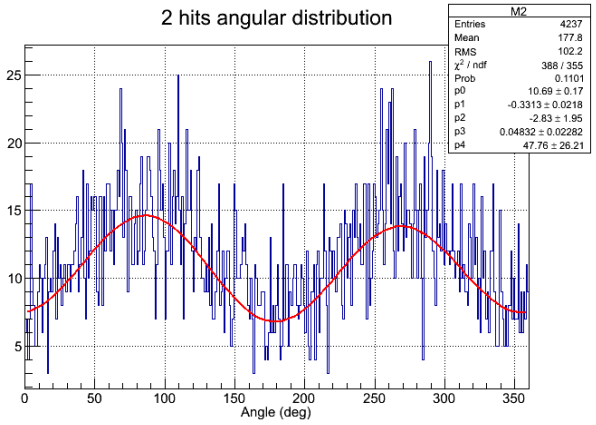

The ground calibration

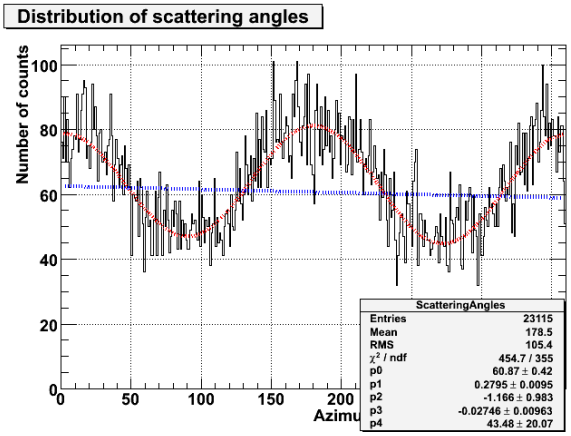

CenterIrradiating CenterScattering Ring2Absorption

The Geant4 simulation

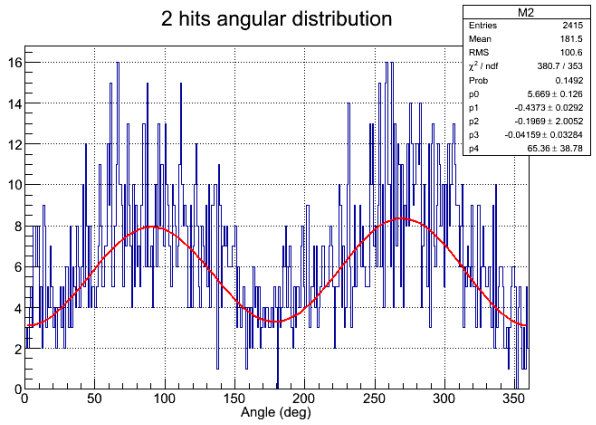

The ground calibration

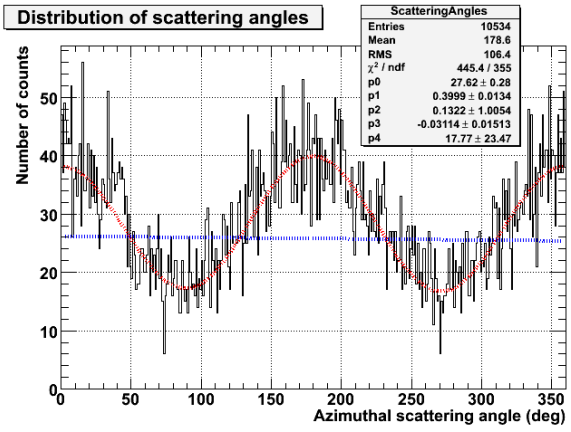

CenterIrradiating CenterScattering Ring3Absorption

The Geant4 simulation

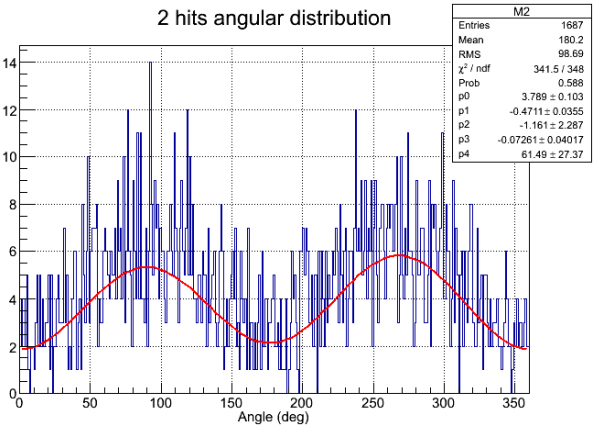

The ground calibration

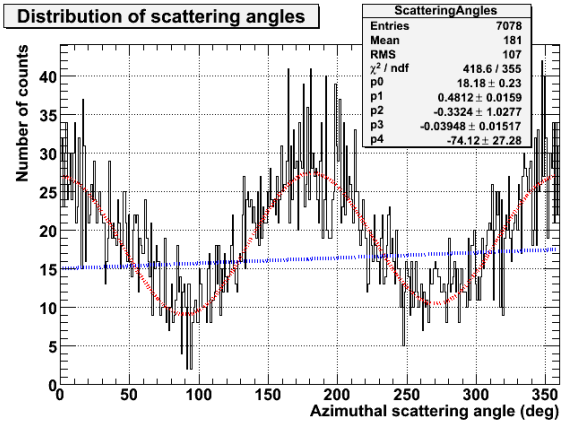

CenterIrradiating CenterScattering Ring4Absorption

The Geant4 simulation

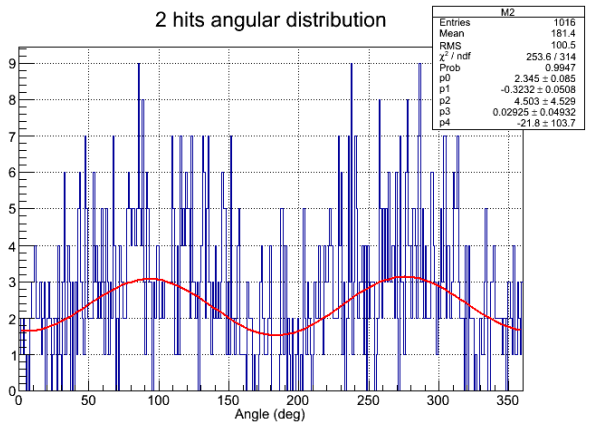

The ground calibration

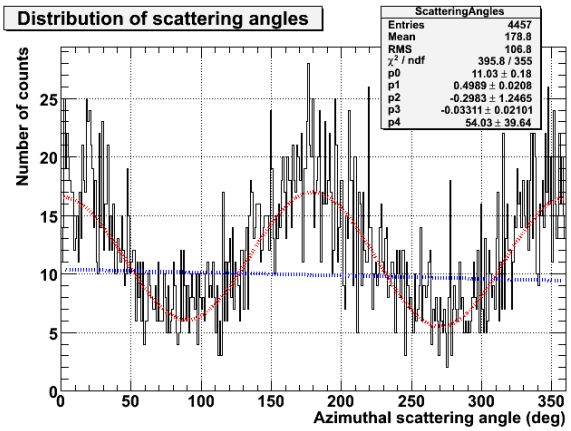

CenterIrradiating Ring1Scattering AnyAbsorption

The Geant4 simulation

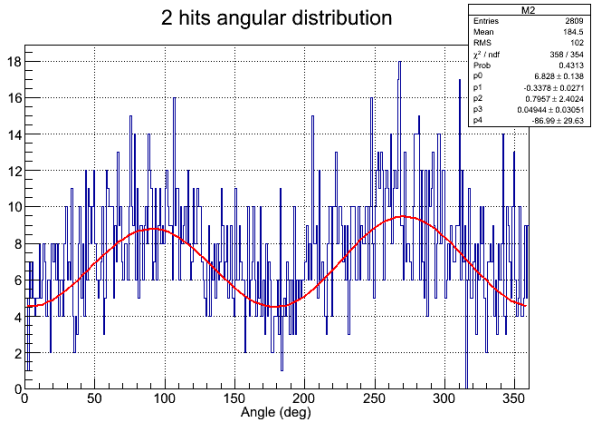

The ground calibration

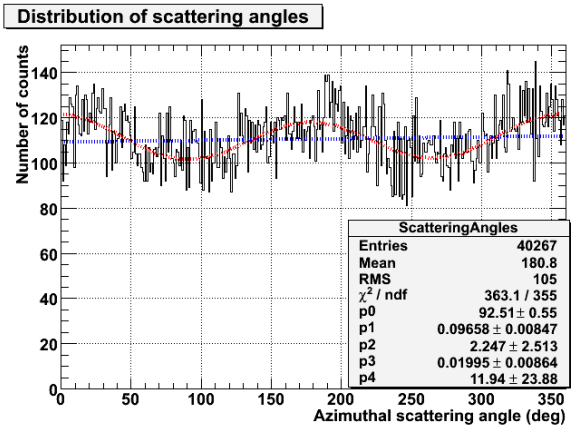

CenterIrradiating Ring2Scattering AnyAbsorption

The Geant4 simulation

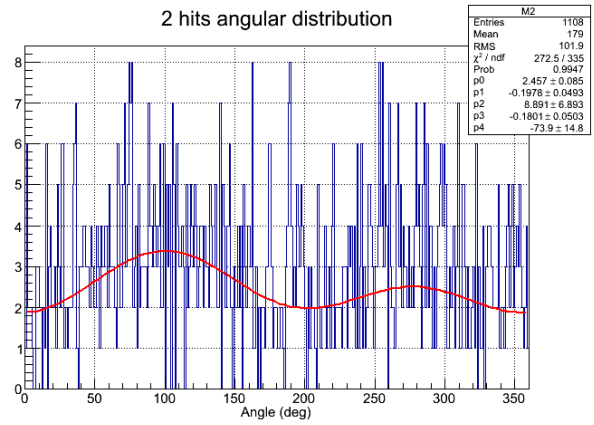

The ground calibration

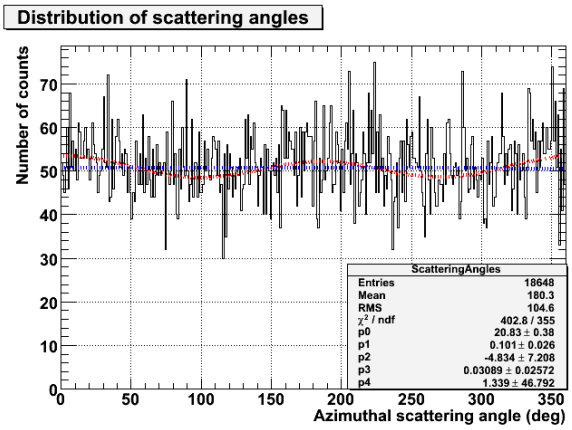

CenterIrradiating Ring3Scattering AnyAbsorption

The Geant4 simulation

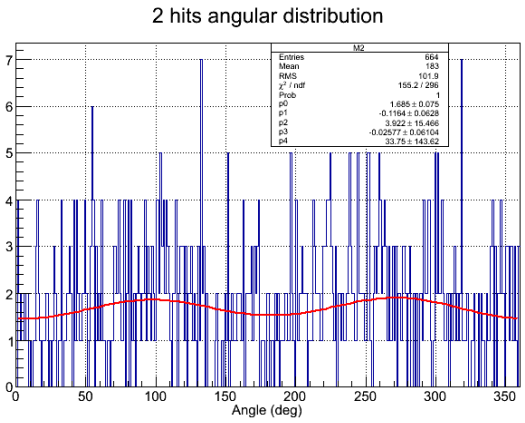

The ground calibration

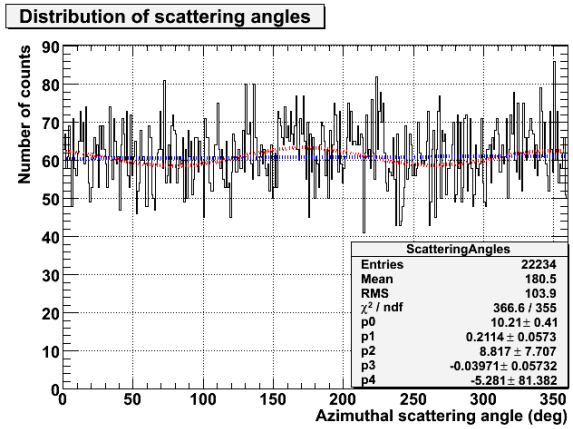

CenterIrradiating Ring4Scattering AnyAbsorption

The Geant4 simulation

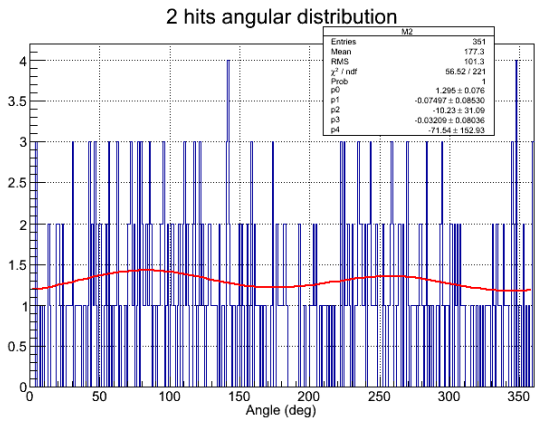

The ground calibration

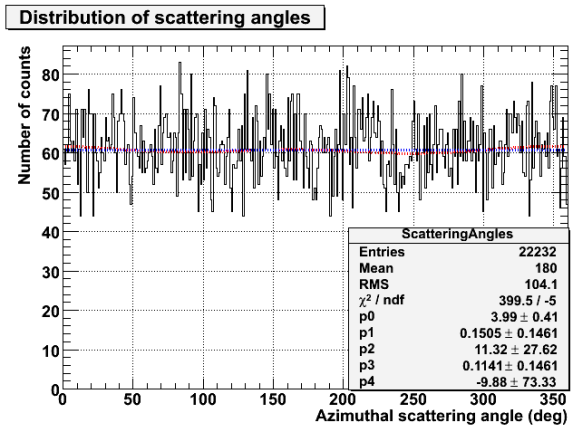

Ring1 Irradiating AnyScattering AnyAbsorption

The Geant4 simulation

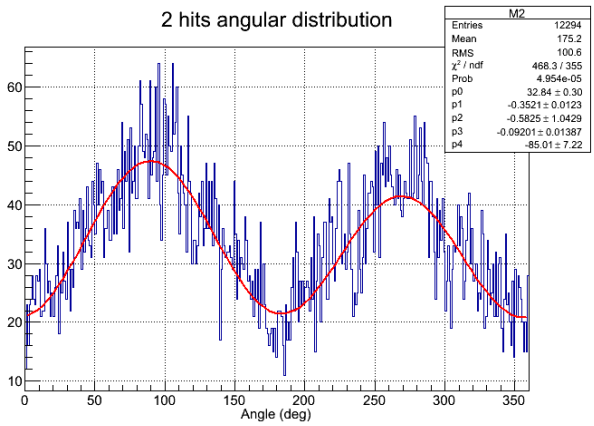

The ground calibration

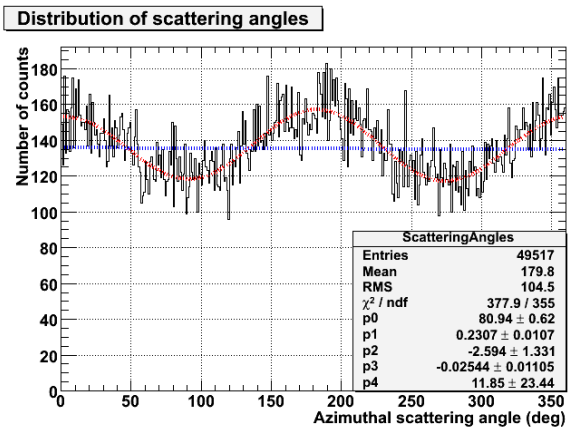

Ring1Irradiating Ring1Scattering AnyAbsorption

The Geant4 simulation

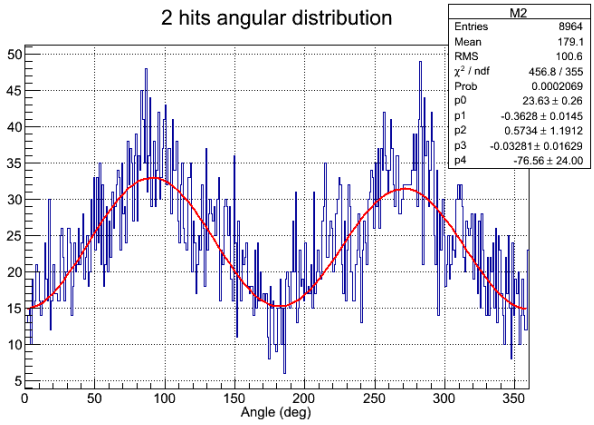

The ground calibration

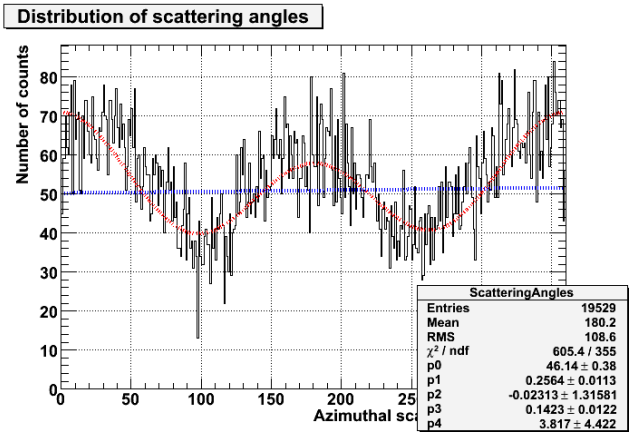

Ring2Irradiating AnyScattering AnyAbsorption

The Geant4 simulation

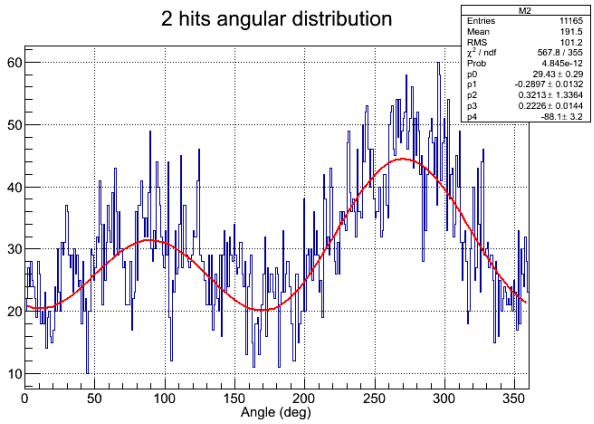

The ground calibration

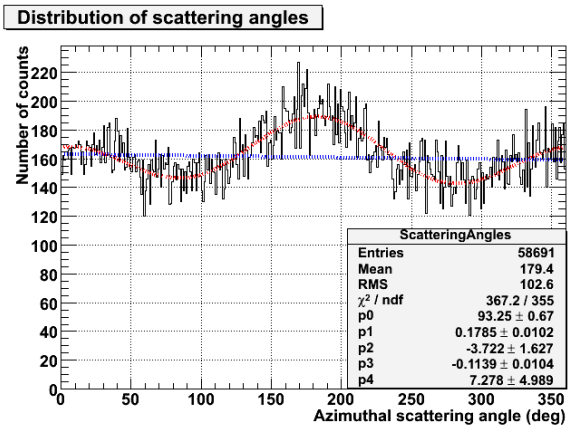

Ring2Irradiating Ring2Scattering AnyAbsorption

The Geant4 simulation

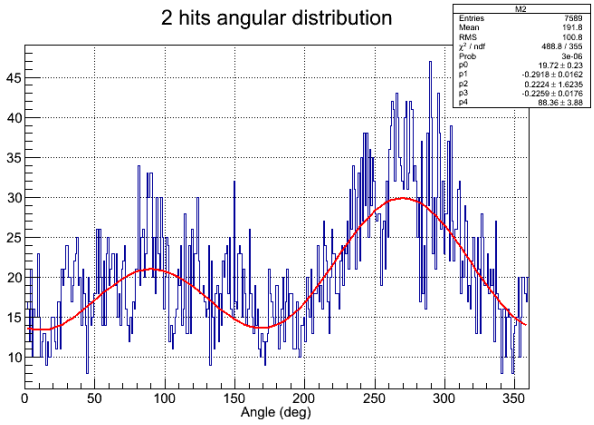

The ground calibration

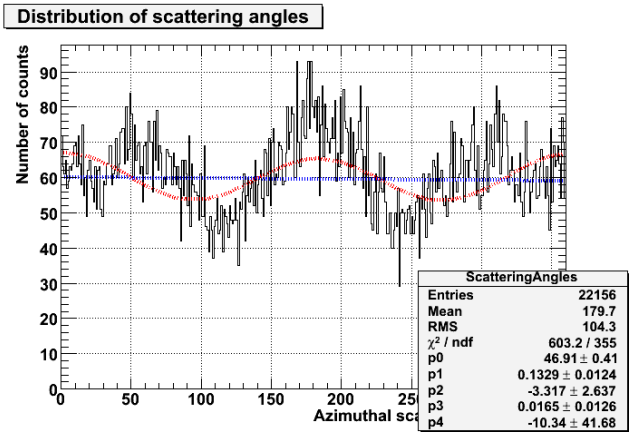

Ring3Irradiating AnyScattering AnyAbsorption

The Geant4 simulation

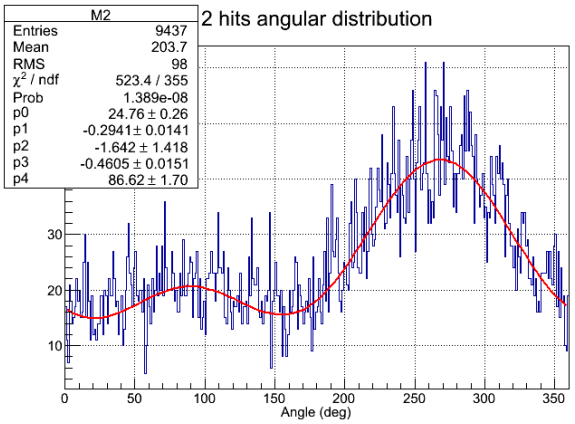

The ground calibration

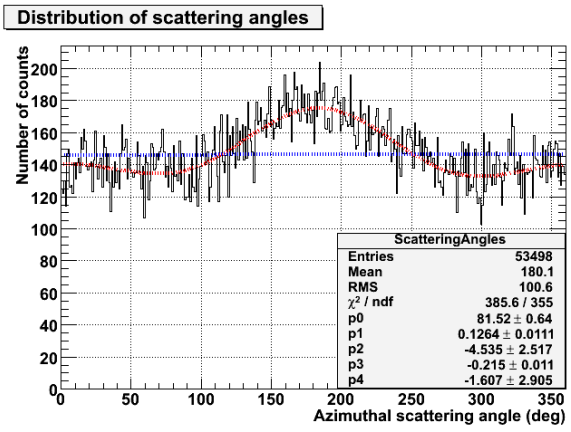

Ring3Irradiating Ring3Scattering AnyAbsorption

The Geant4 simulation

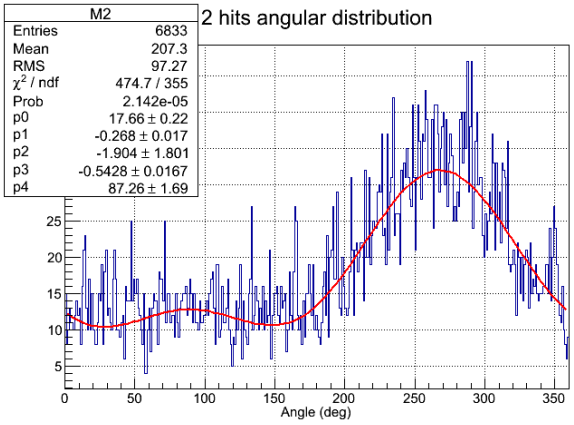

The ground calibration

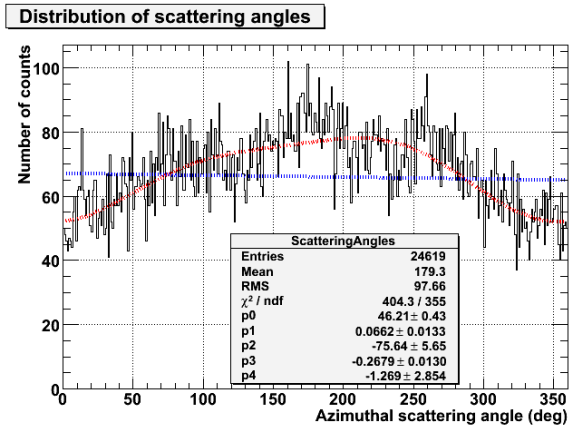

Ring4Irradiating AnyScattering AnyAbsorption

The Geant4 simulation

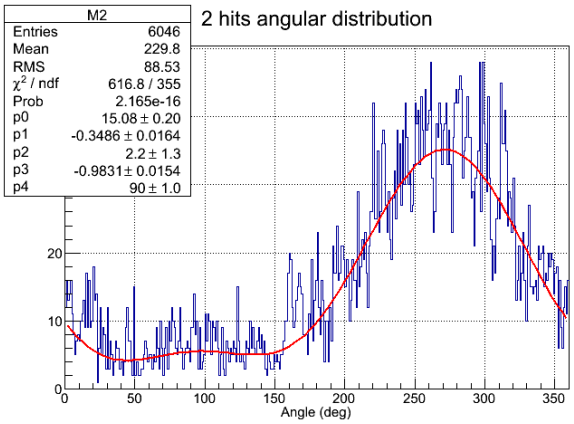

The ground calibration

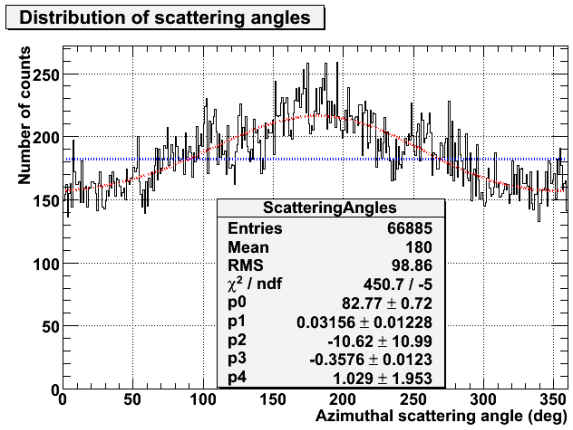

Ring4Irradiating Ring4Scattering AnyAbsorption

The Geant4 simulation

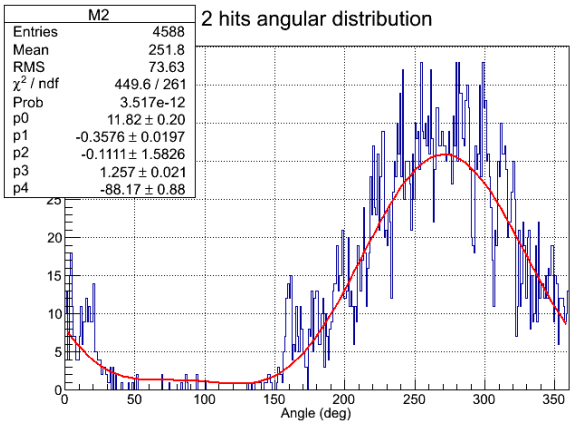

The ground calibration

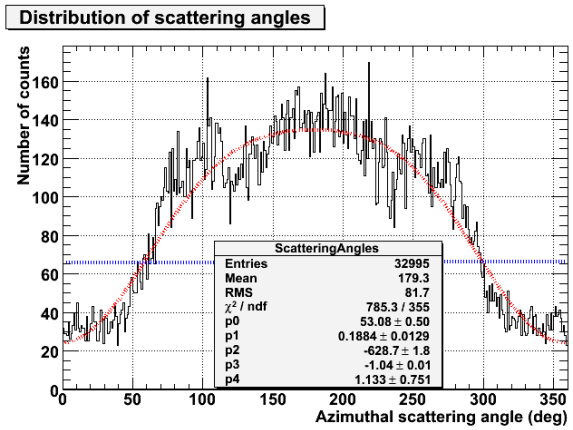

Appendix B

B.1 2D histogram and the projection (means energy spectrum) with the threshold 0 ADC channel and 60 ADC channel

CenterIrradiating, ???Scattering, AnyAbsorption, Threshold 0ch

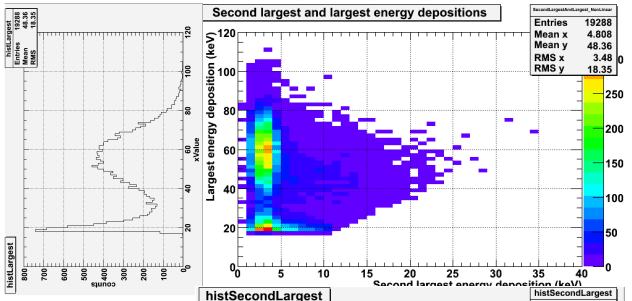

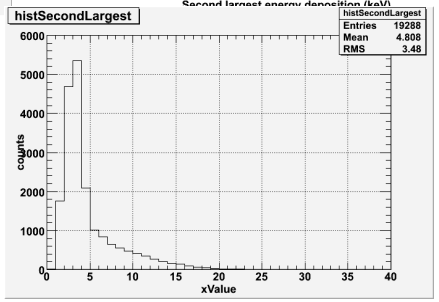

Angela

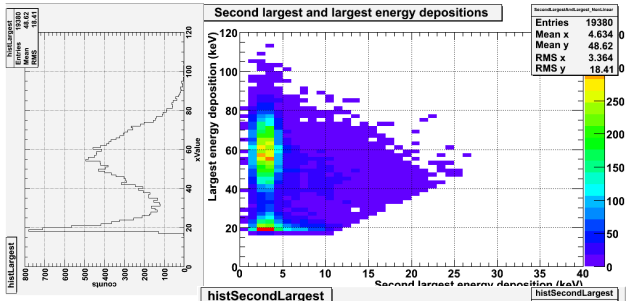

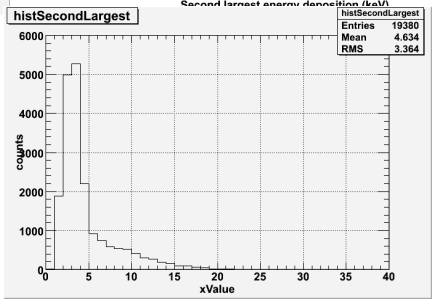

Yngve

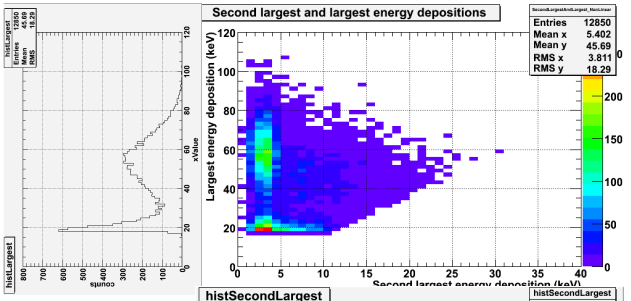

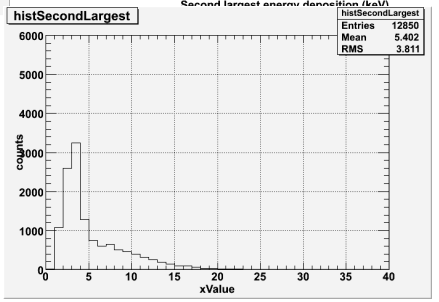

Jiro

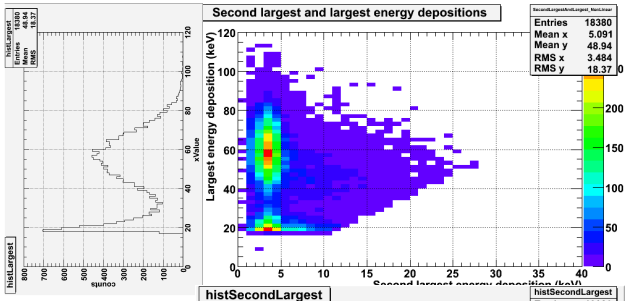

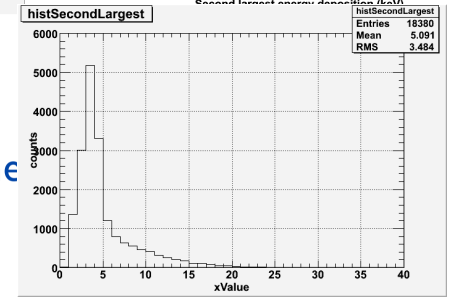

Persephone

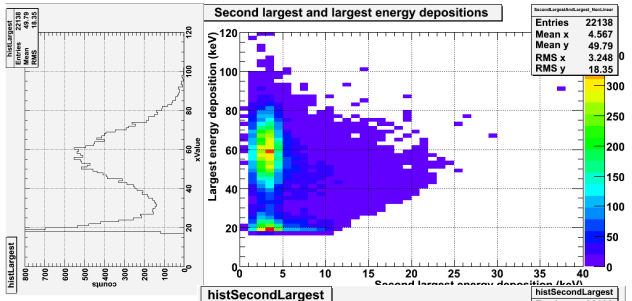

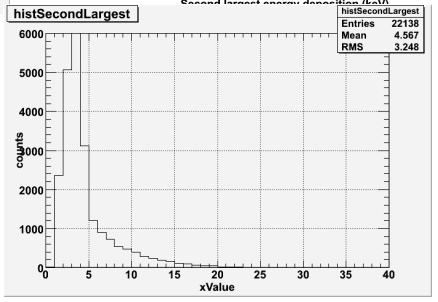

Hicks

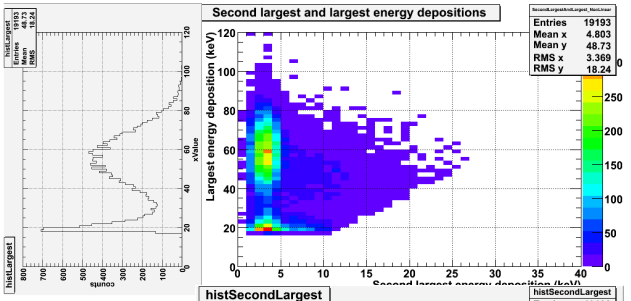

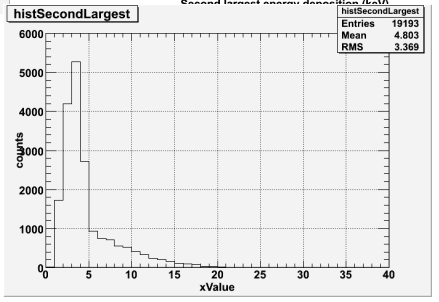

Sara

CenterIrradiating, ???Scattering, AnyAbsorption, Threshold 10ch

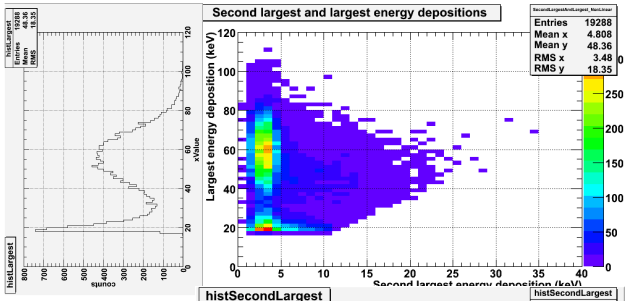

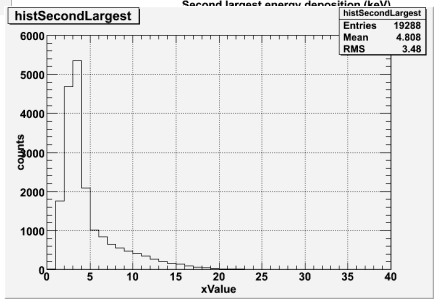

Angela

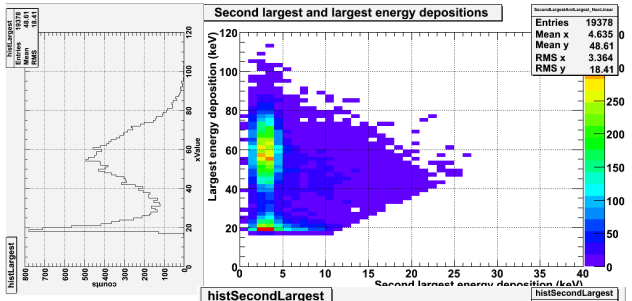

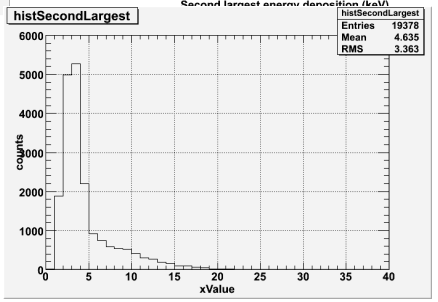

Yngve

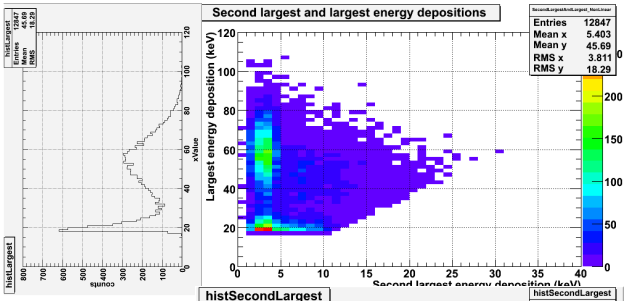

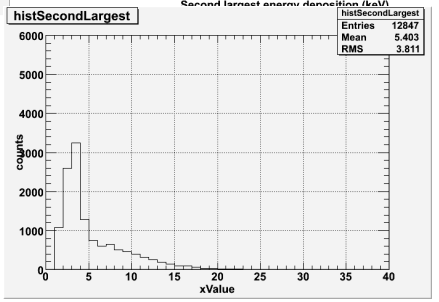

Jiro

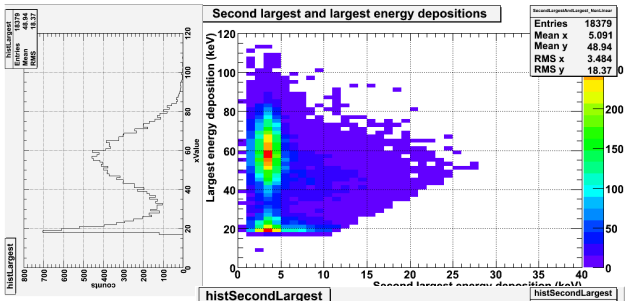

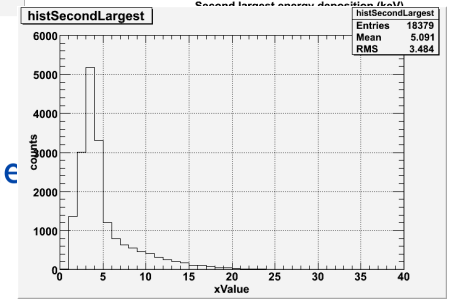

Persephone

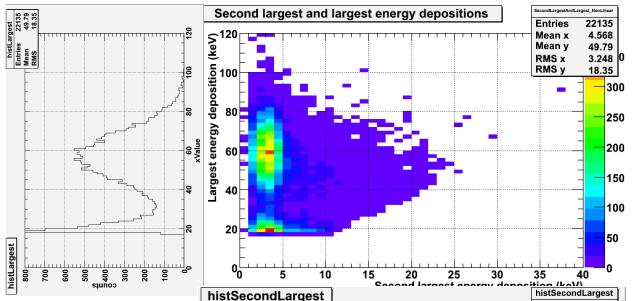

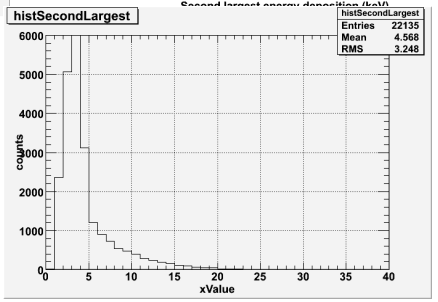

Hicks

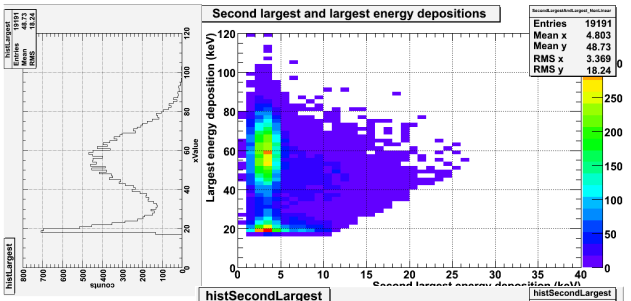

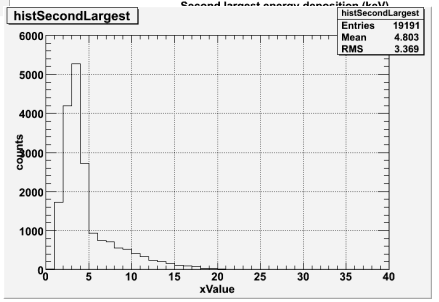

Sara

CenterIrradiating, ???Scattering, AnyAbsorption, Threshold 20ch

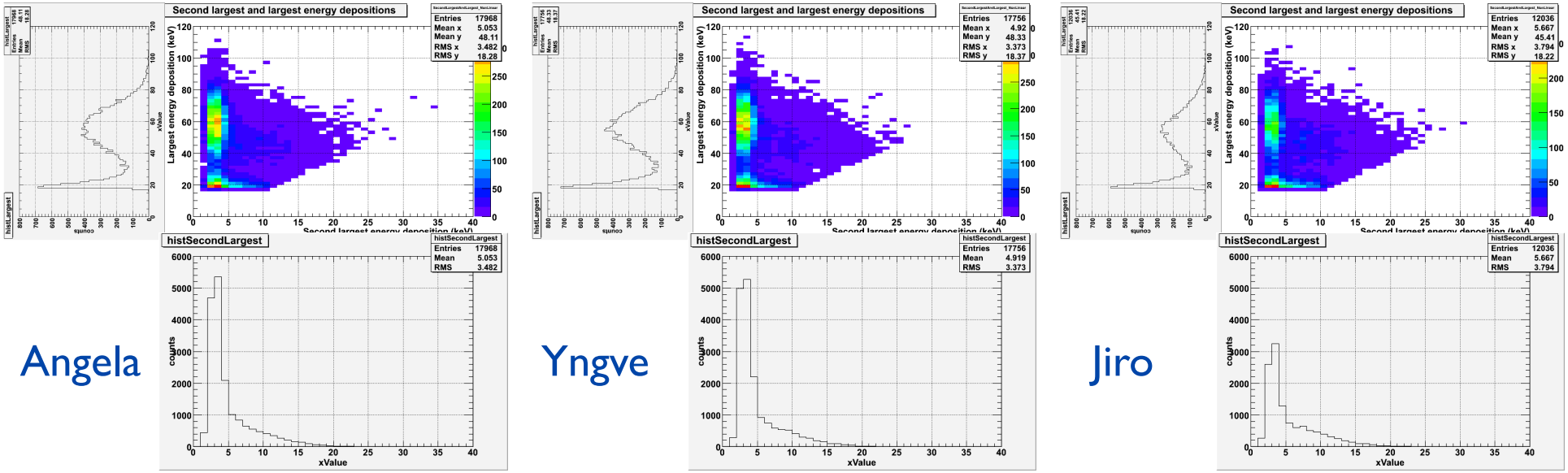

Angela Yngve Jiro

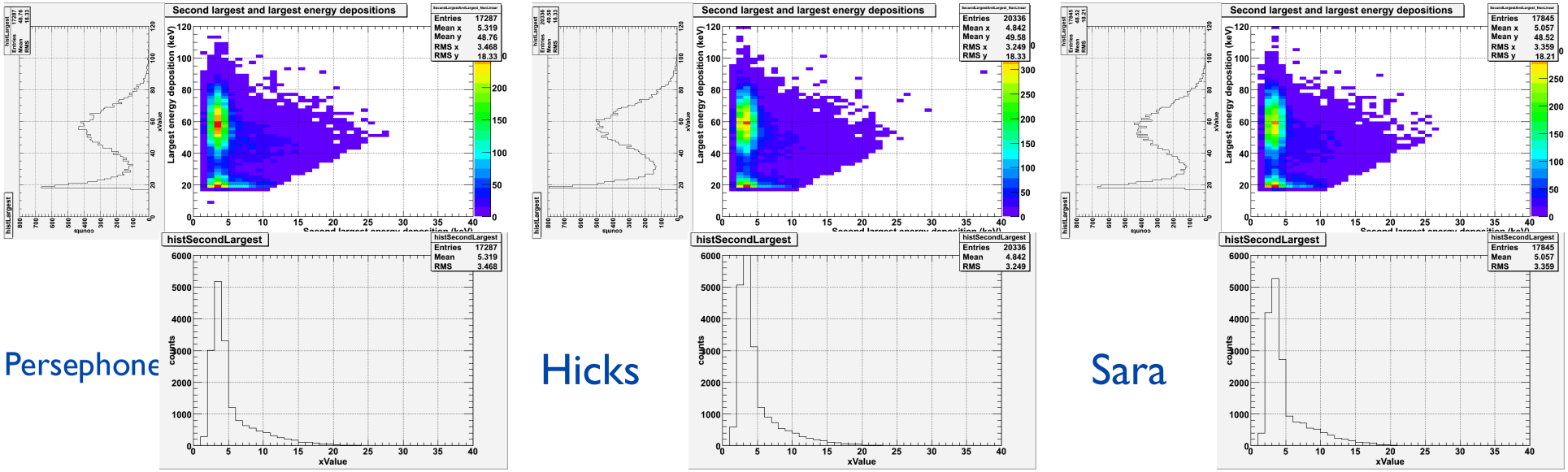

Persephone Hicks Sara

CenterIrradiating, ???Scattering, AnyAbsorption, Threshold 30ch

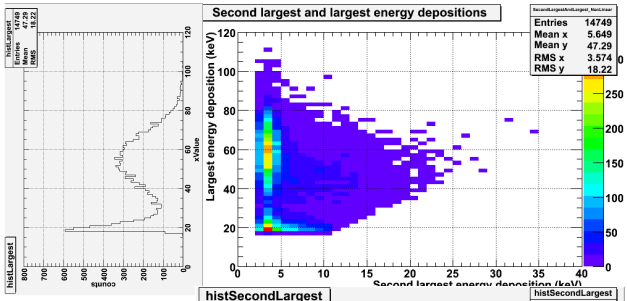

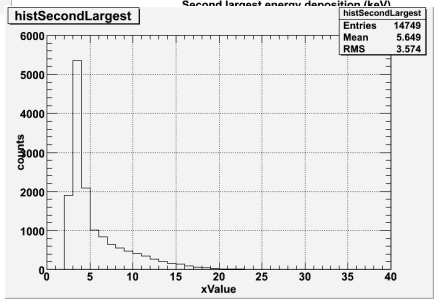

Angela

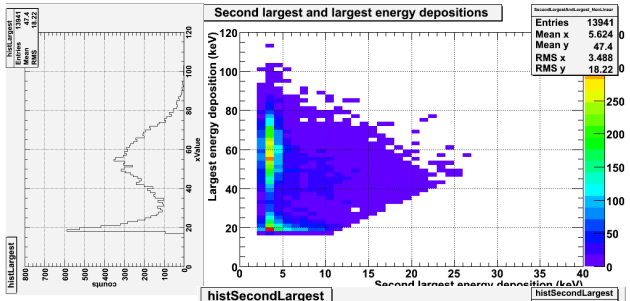

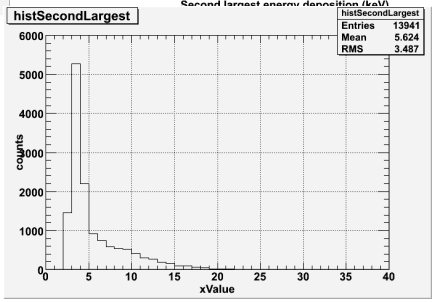

Yngve

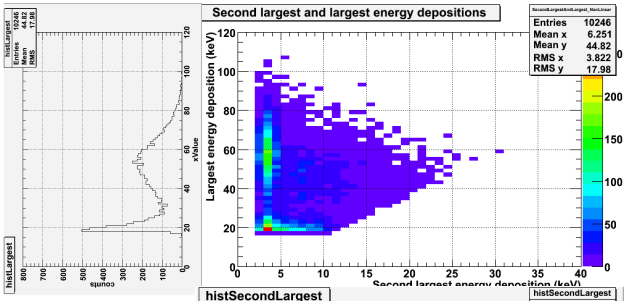

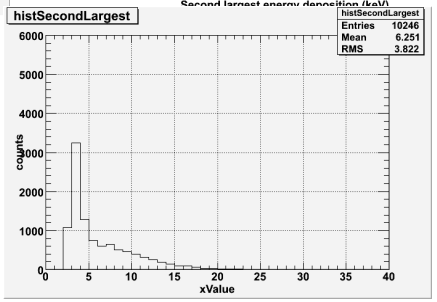

Jiro

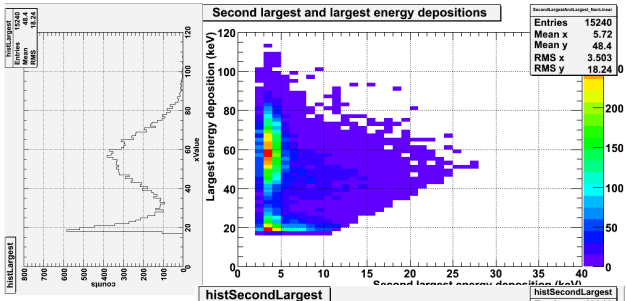

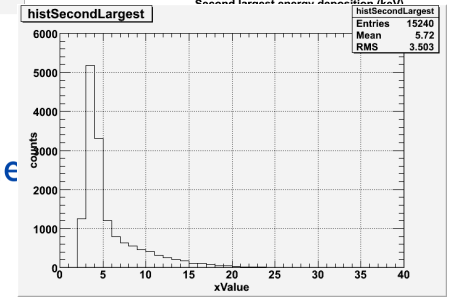

Persephone

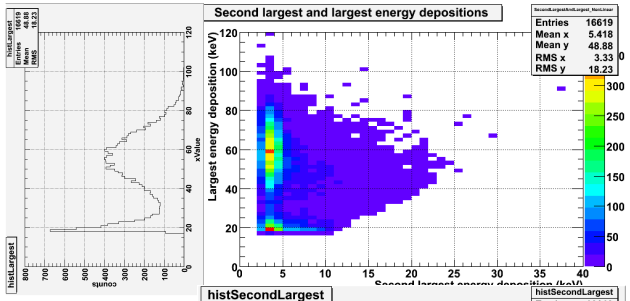

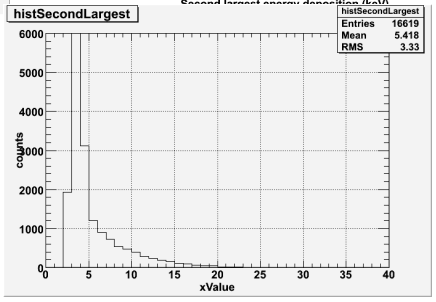

Hicks

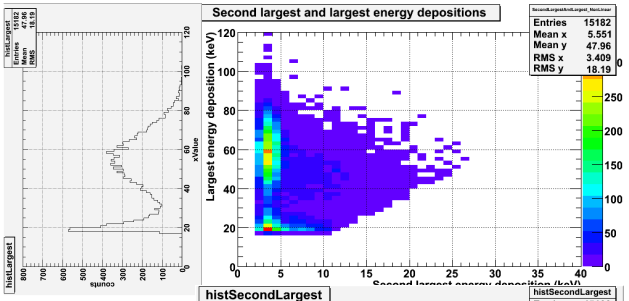

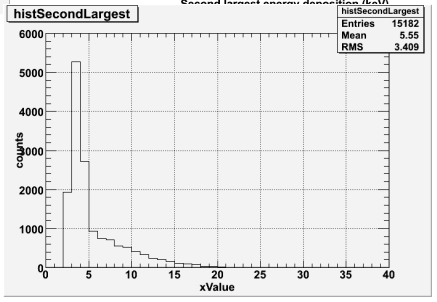

Sara

CenterIrradiating, ???Scattering, AnyAbsorption, Threshold 40ch

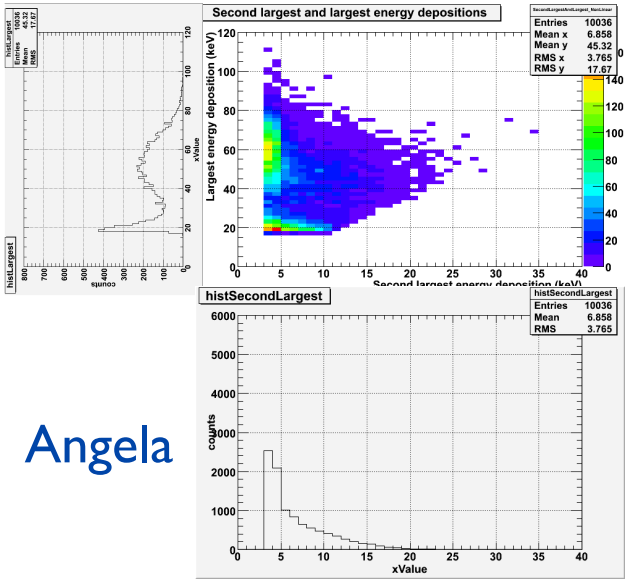

Angela

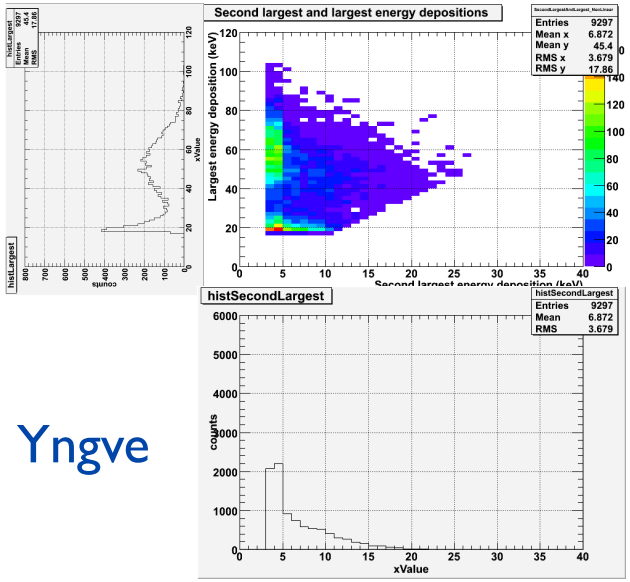

Yngve

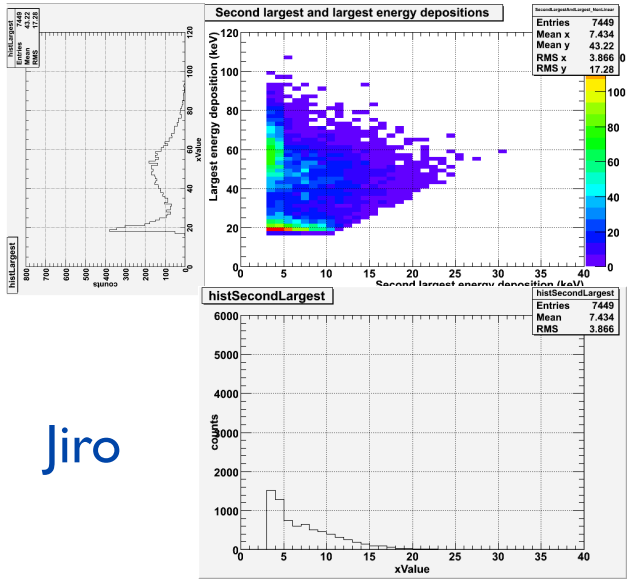

Jiro

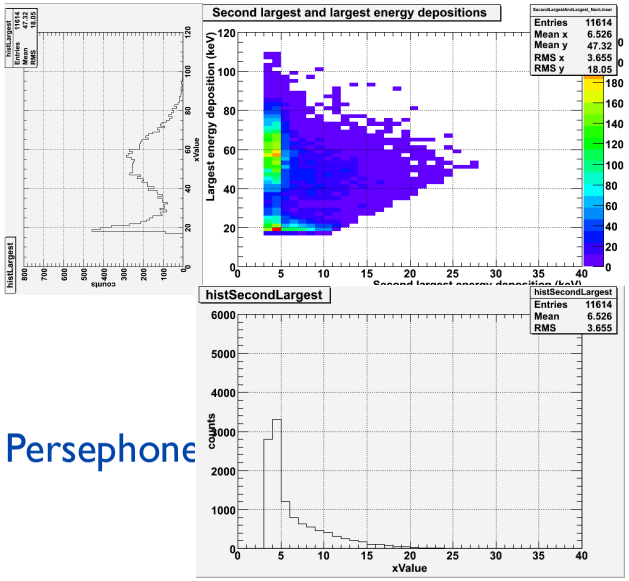

Persephone

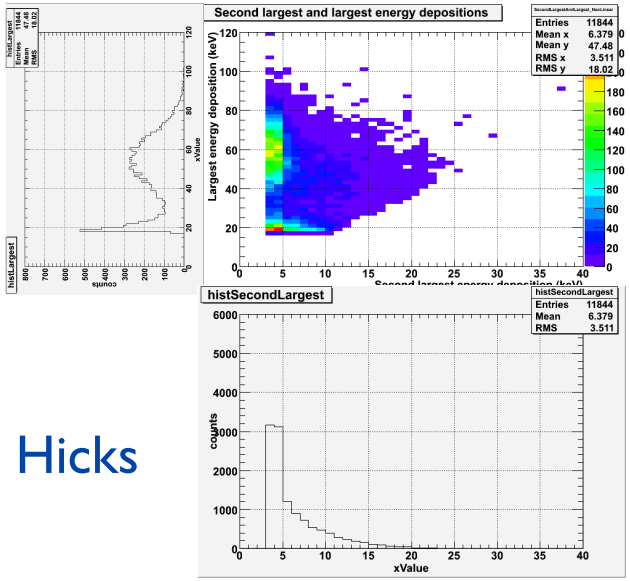

Hicks

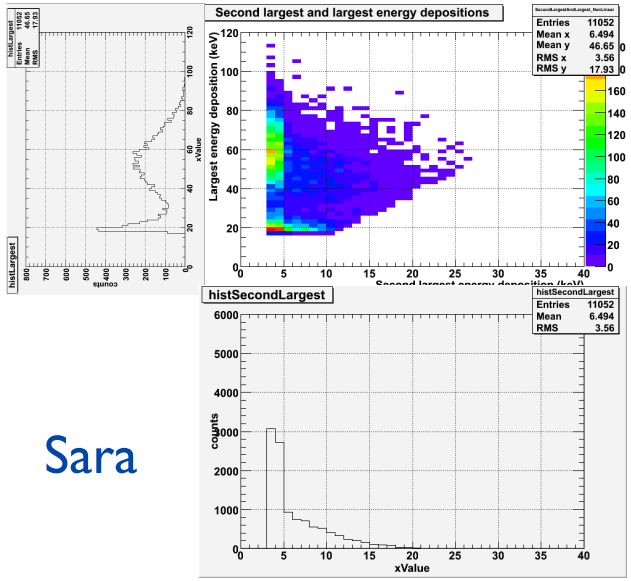

Sara

CenterIrradiating, ???Scattering, AnyAbsorption, Threshold 50ch

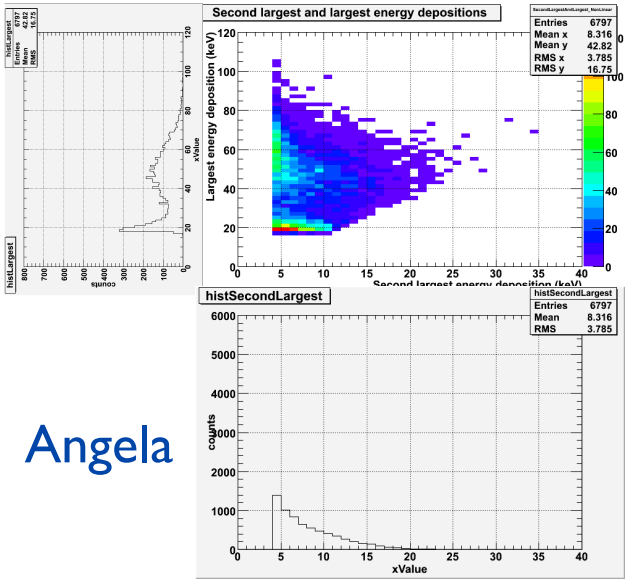

Angela

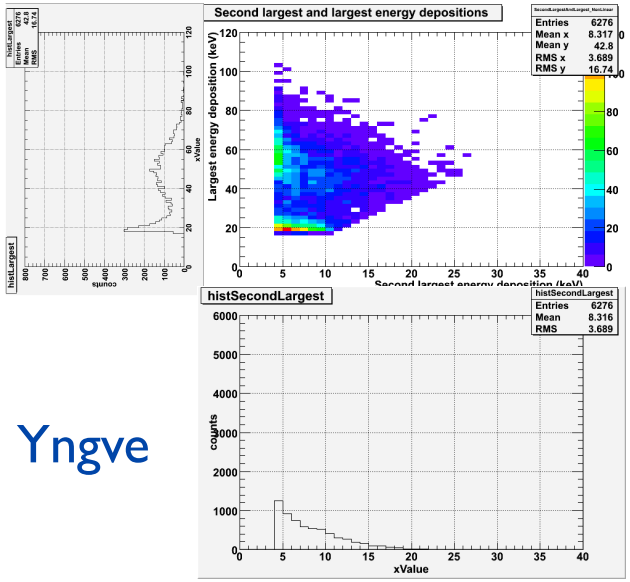

Yngve

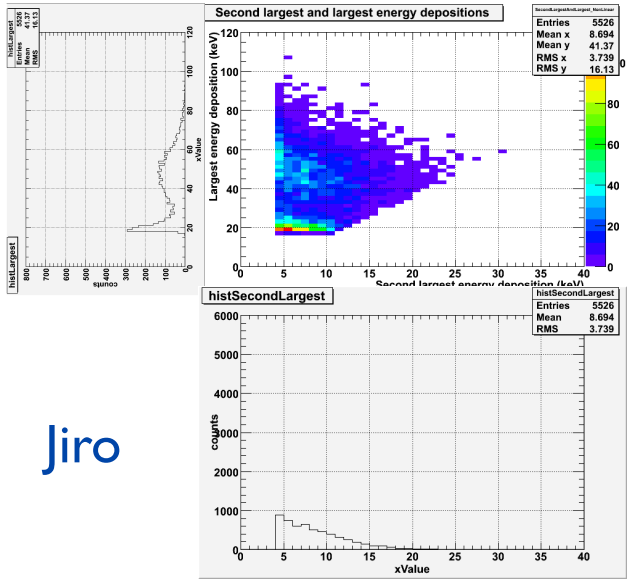

Jiro

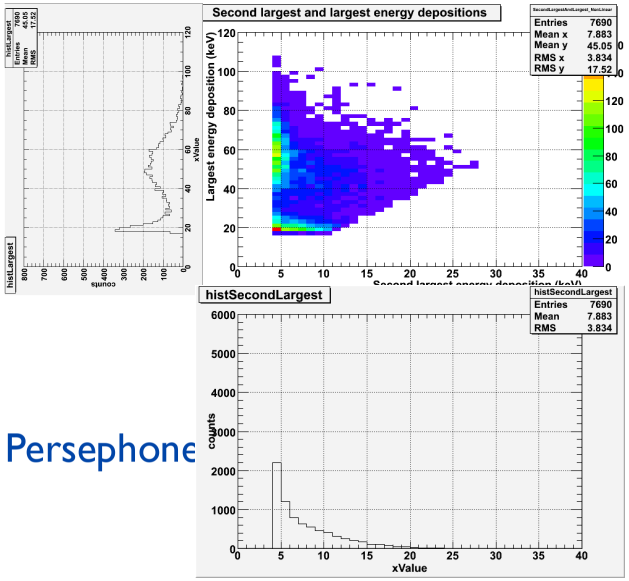

Persephone

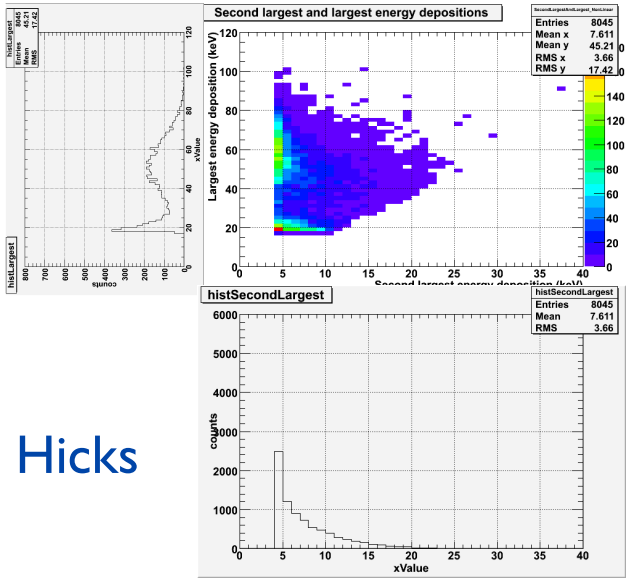

Hicks

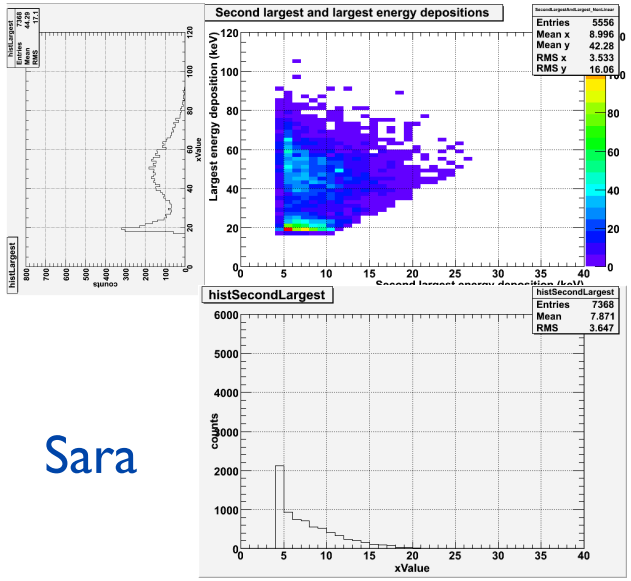

Sara

CenterIrradiating, ???Scattering, AnyAbsorption, Threshold 60ch

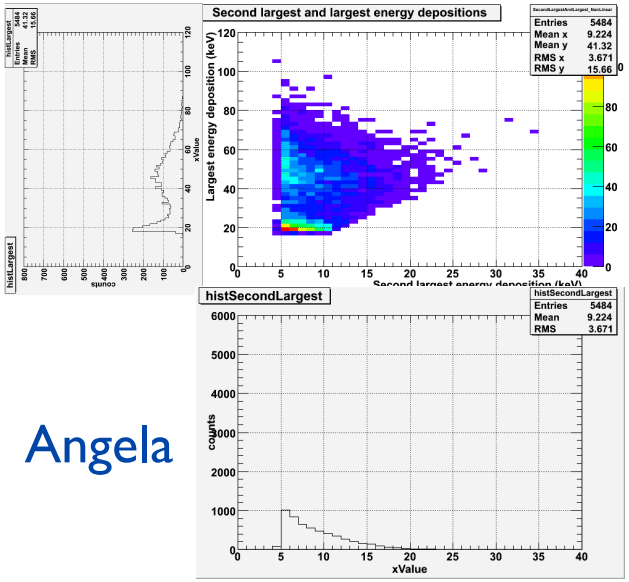

Angela

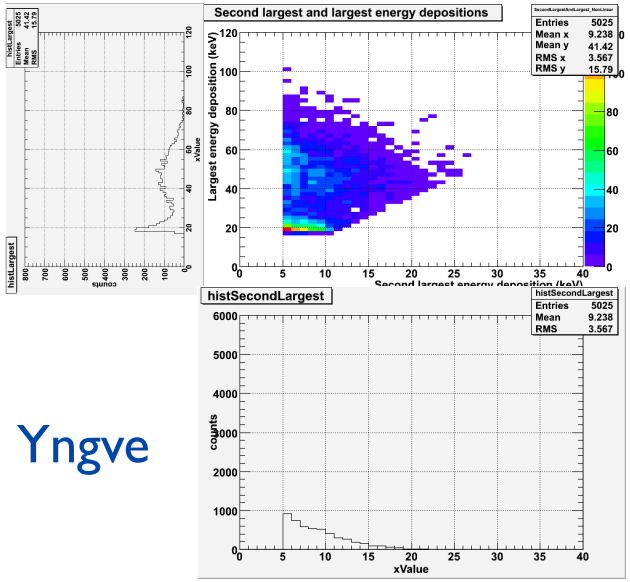

Yngve

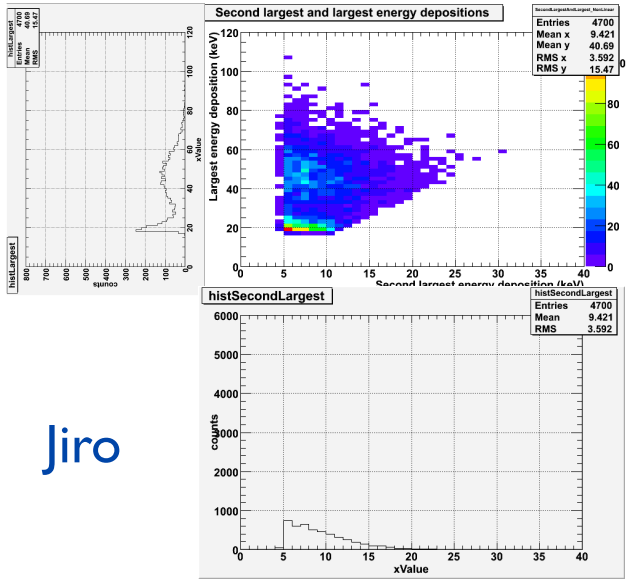

Jiro

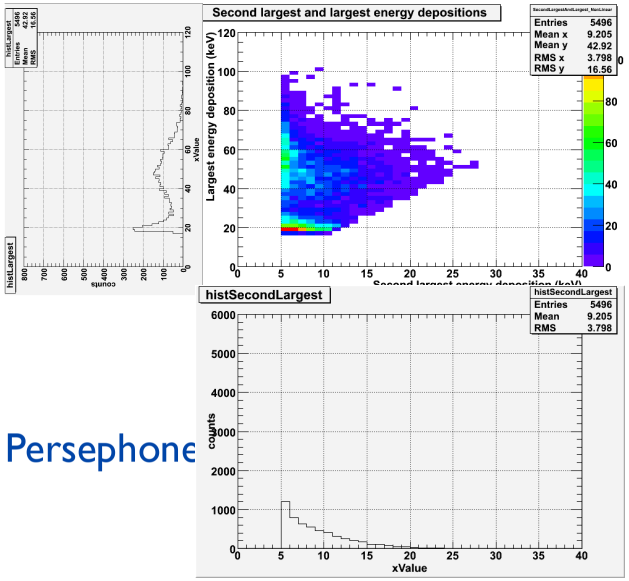

Persephone

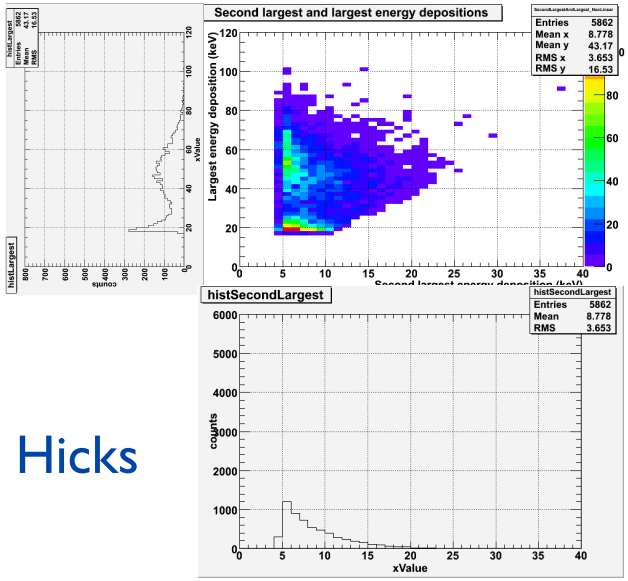

Hicks

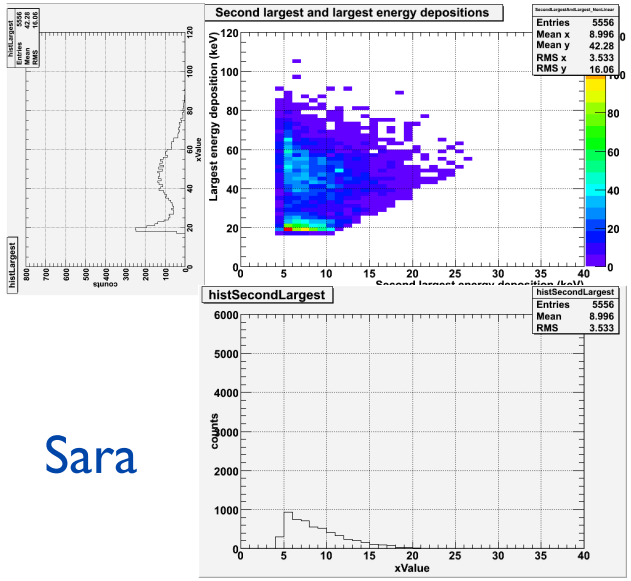

Sara

100

CenterIrradiating, BarretScattering, ???Absorption, Threshold 0ch

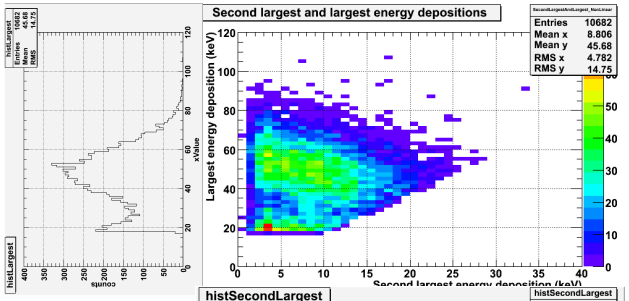

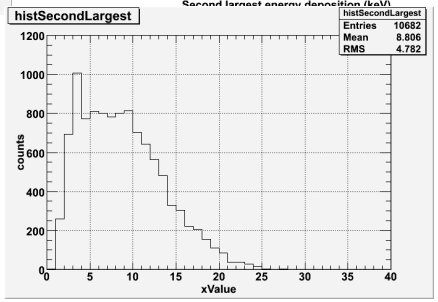

Angela

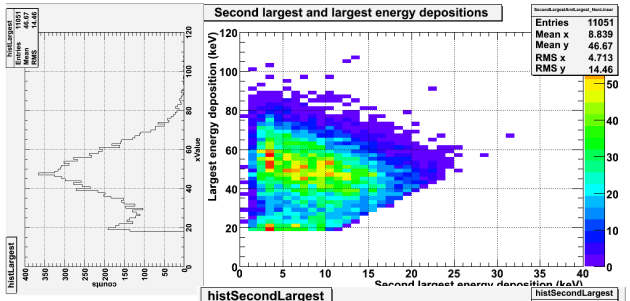

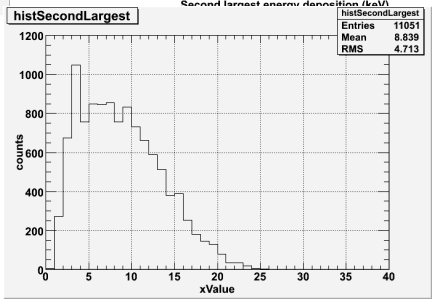

Yngve

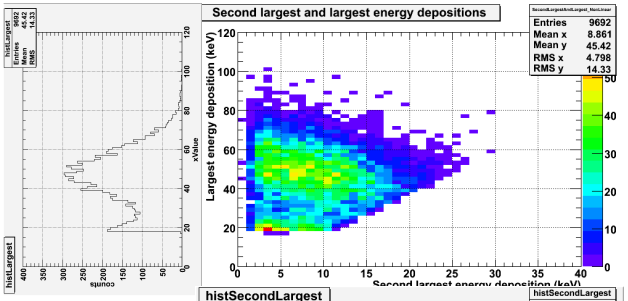

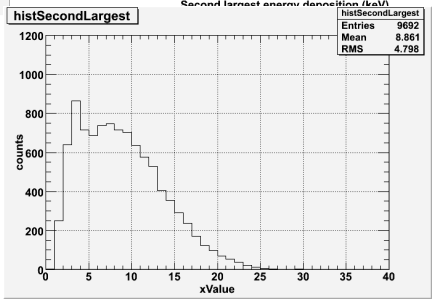

Jiro

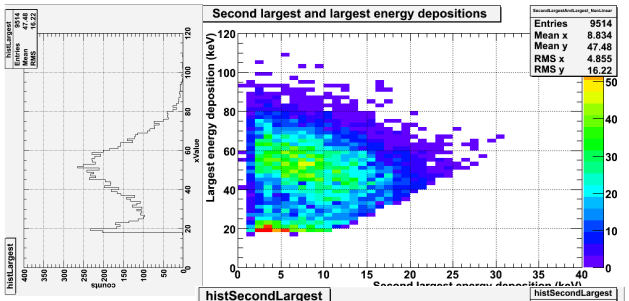

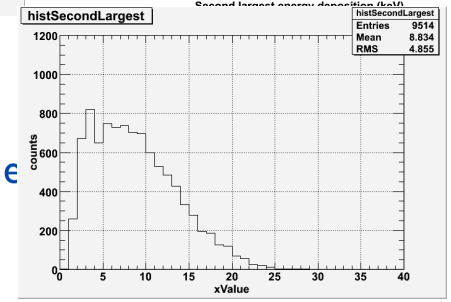

Persephone

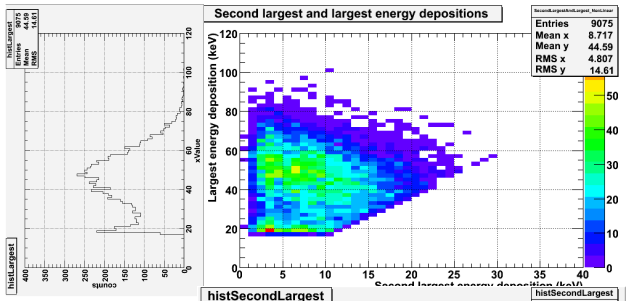

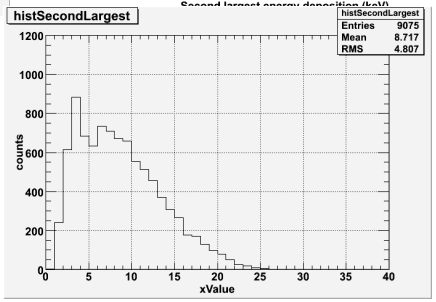

Hicks

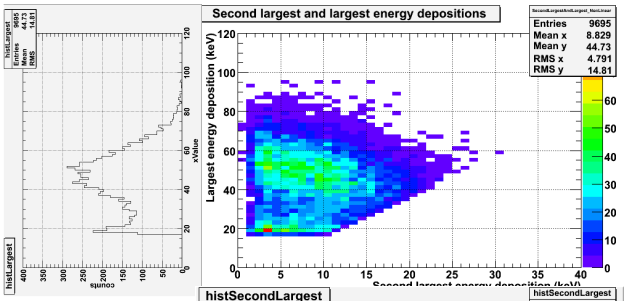

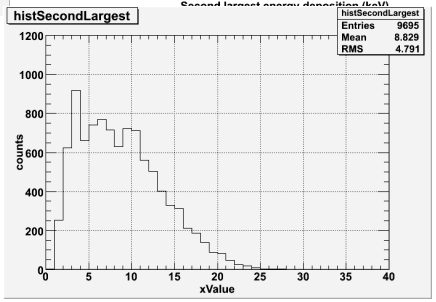

Sara

CenterIrradiating, BarretScattering, ???Absorption, Threshold 10ch

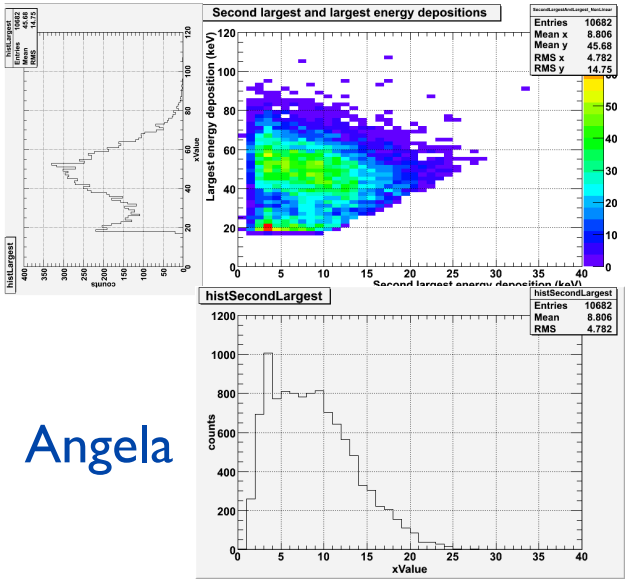

Angela

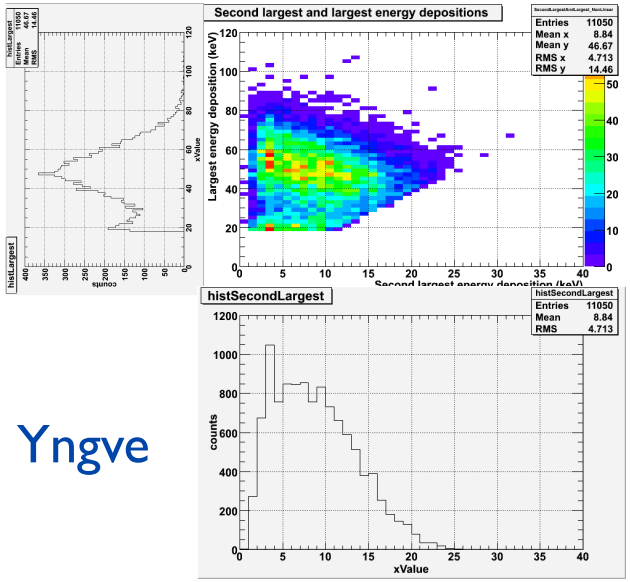

Yngve

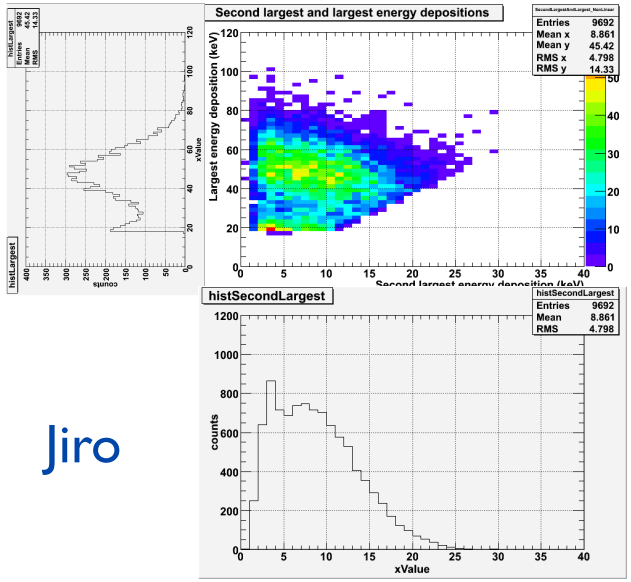

Jiro

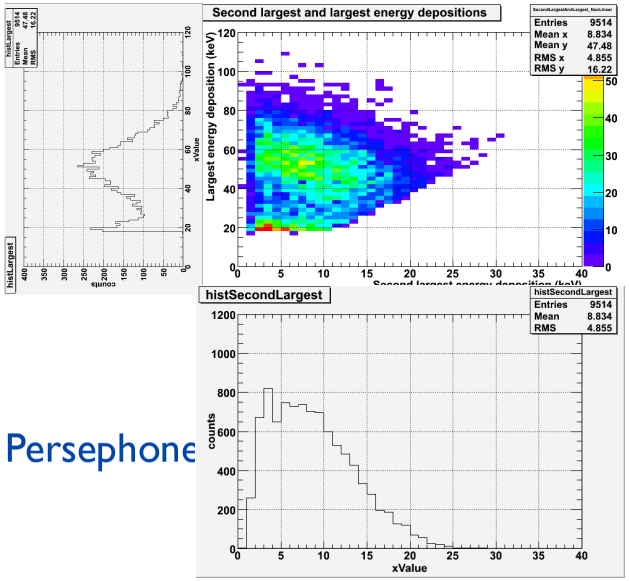

Persephone

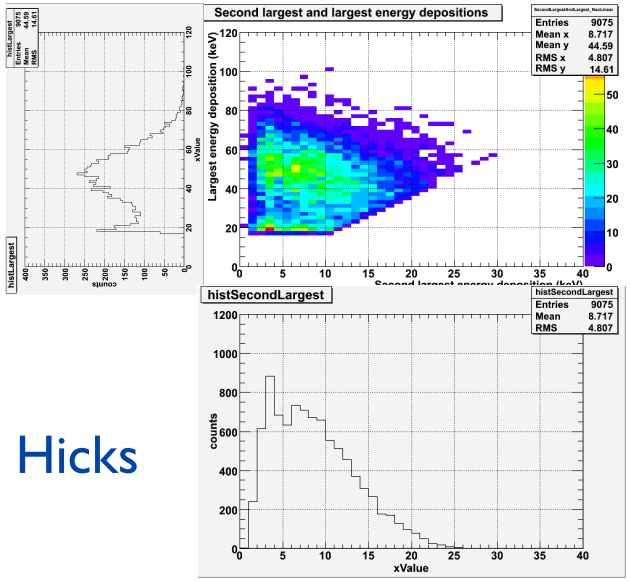

Hicks

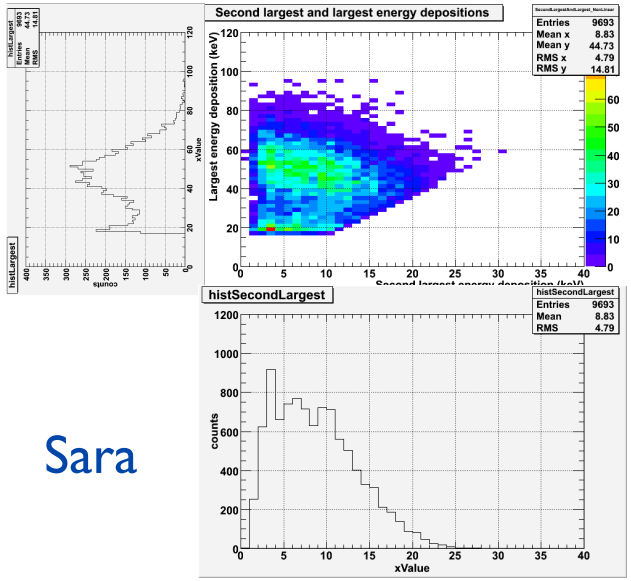

Sara

CenterIrradiating, BarretScattering, ???Absorption, Threshold 20ch

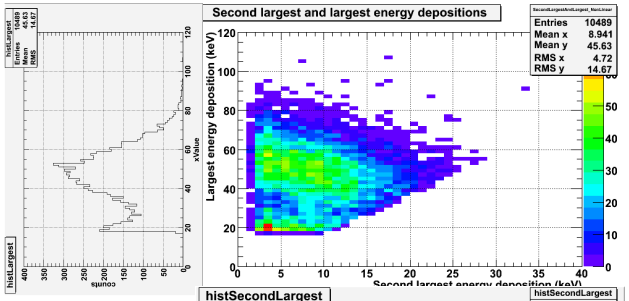

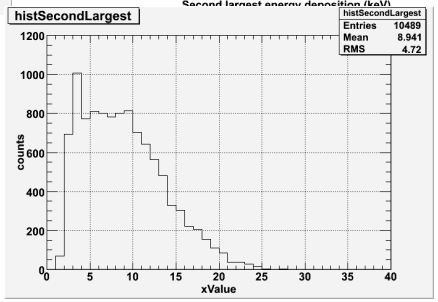

Angela

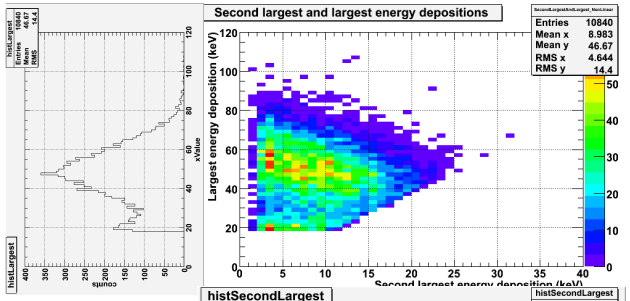

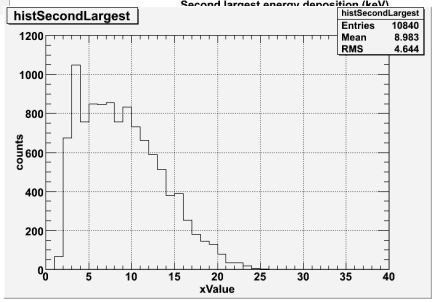

Yngve

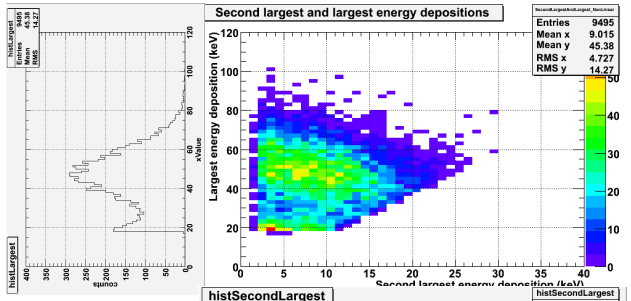

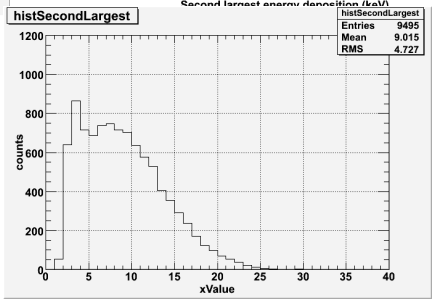

Jiro

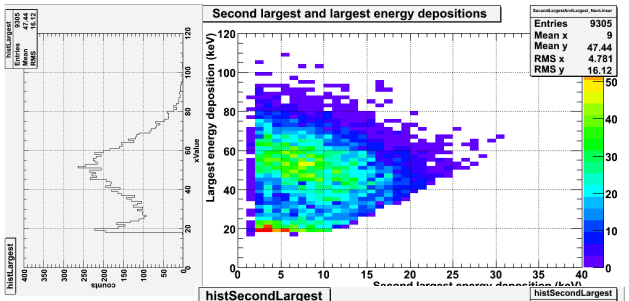

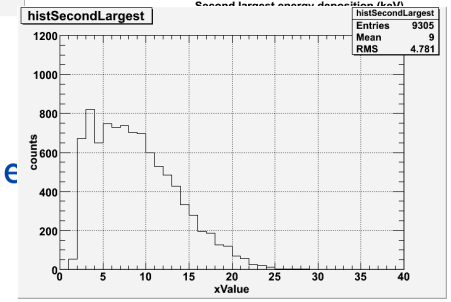

Persephone

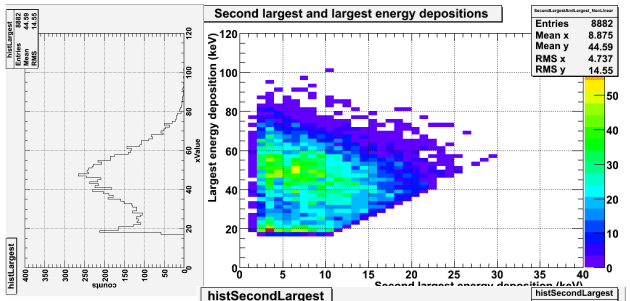

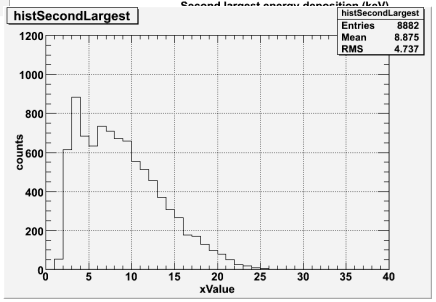

Hicks

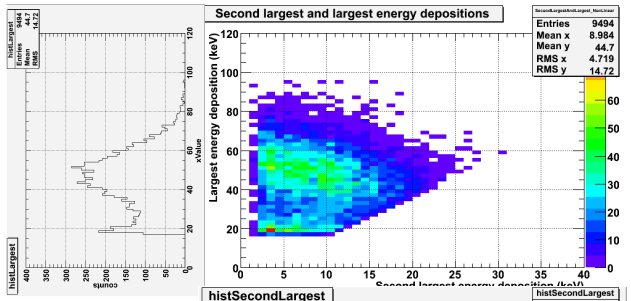

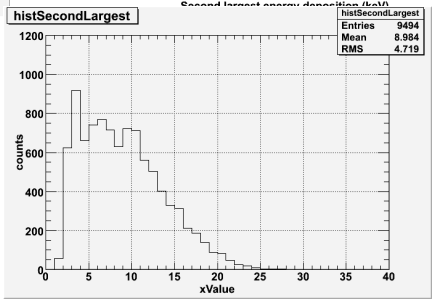

Sara

CenterIrradiating, BarretScattering, ???Absorption, Threshold 30ch

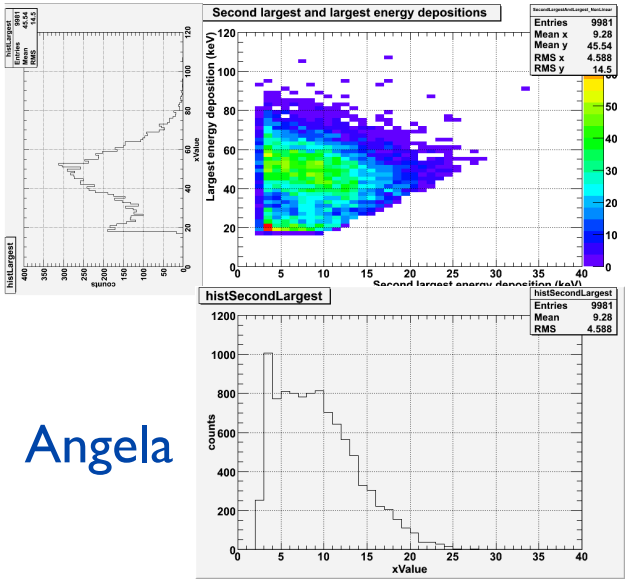

Angela

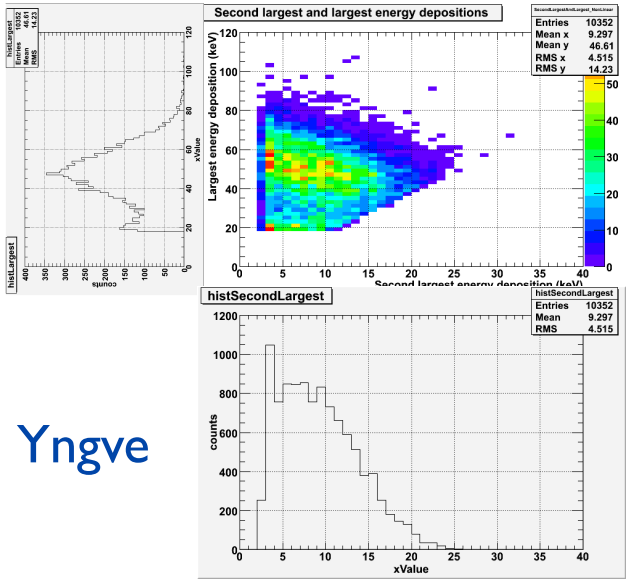

Yngve

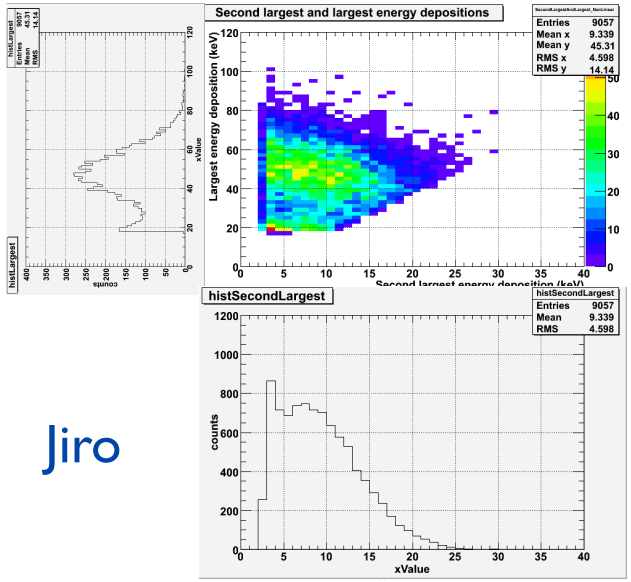

Jiro

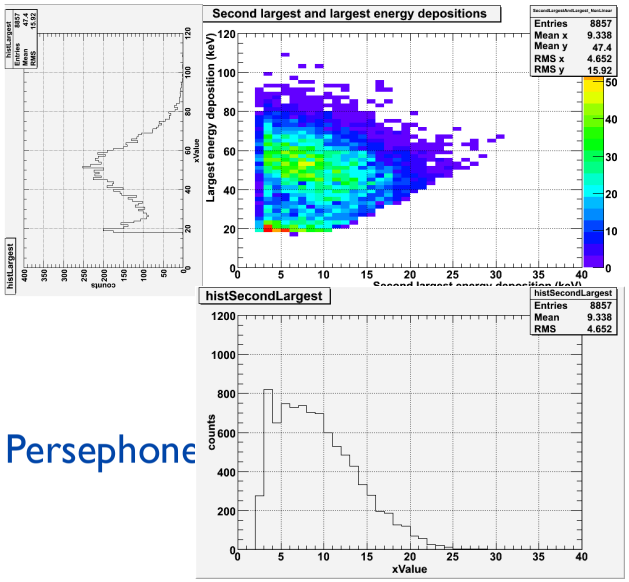

Persephone

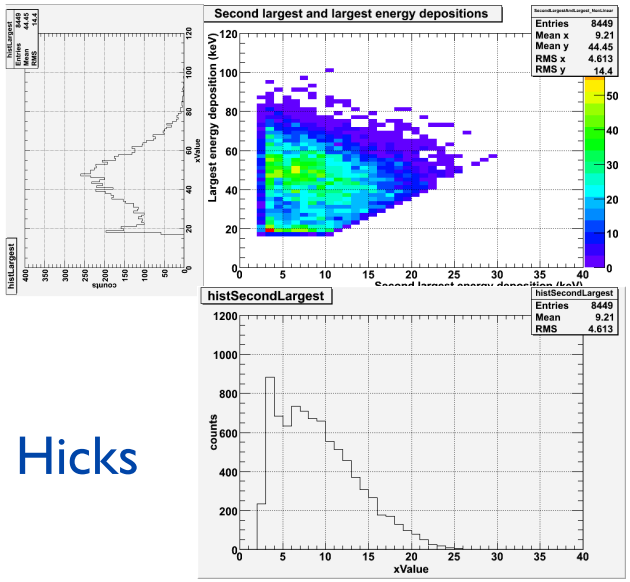

Hicks

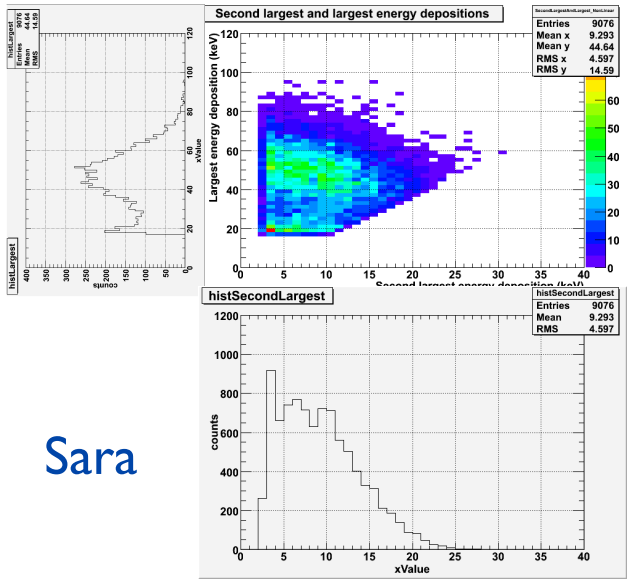

Sara

CenterIrradiating, BarretScattering, ???Absorption, Threshold 40ch

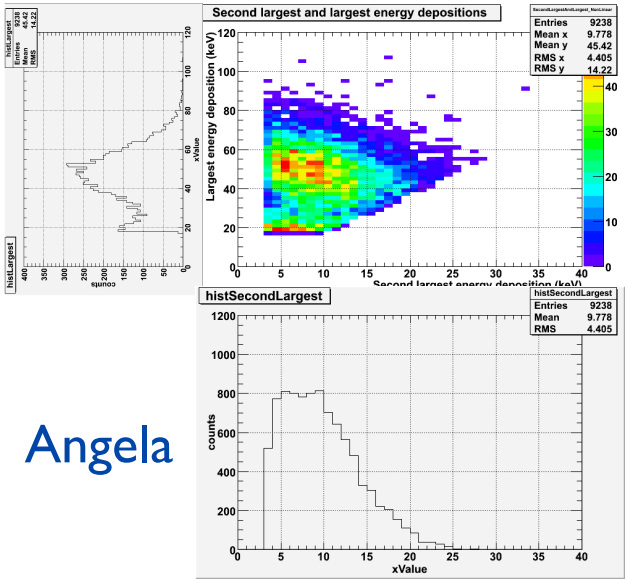

Angela

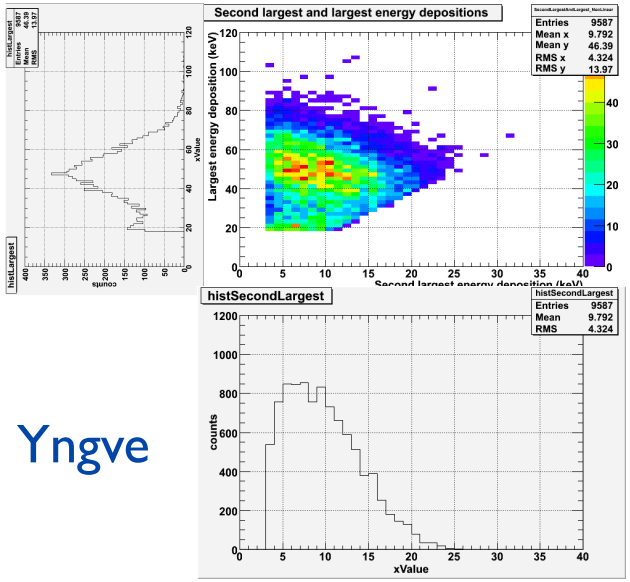

Yngve

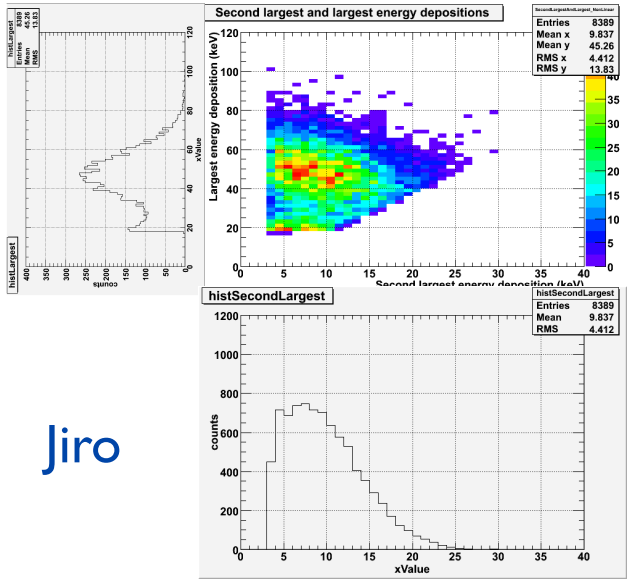

Jiro

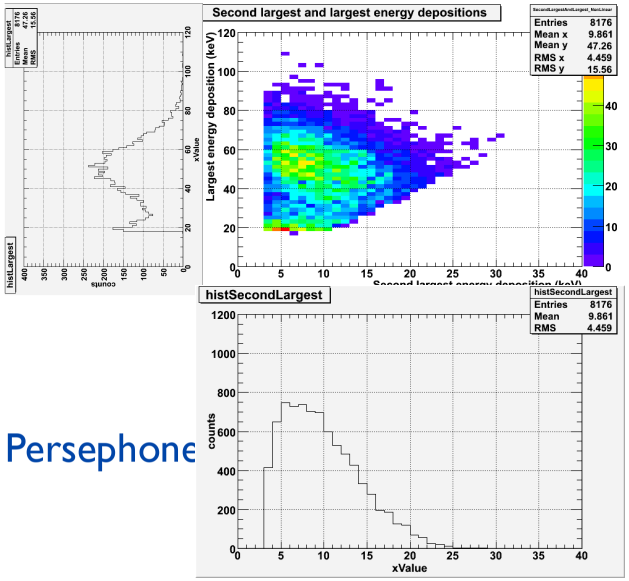

Persephone

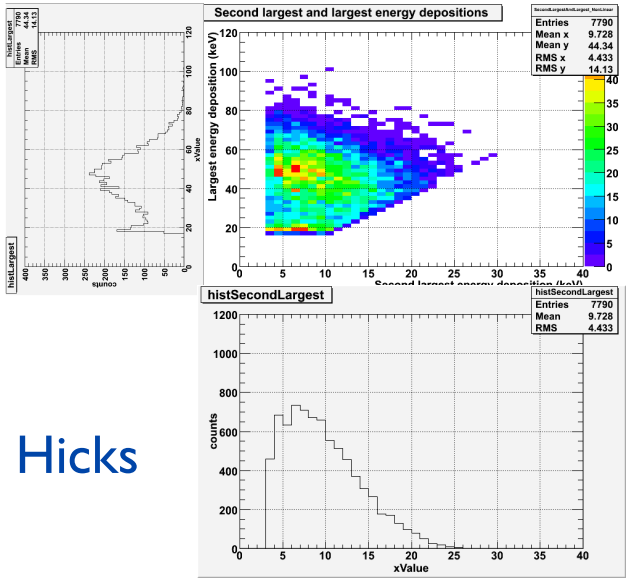

Hicks

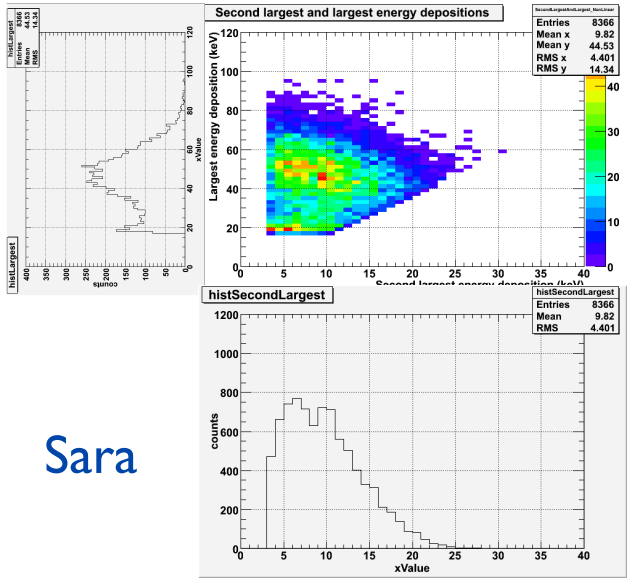

Sara

CenterIrradiating, BarretScattering, ???Absorption, Threshold 50ch

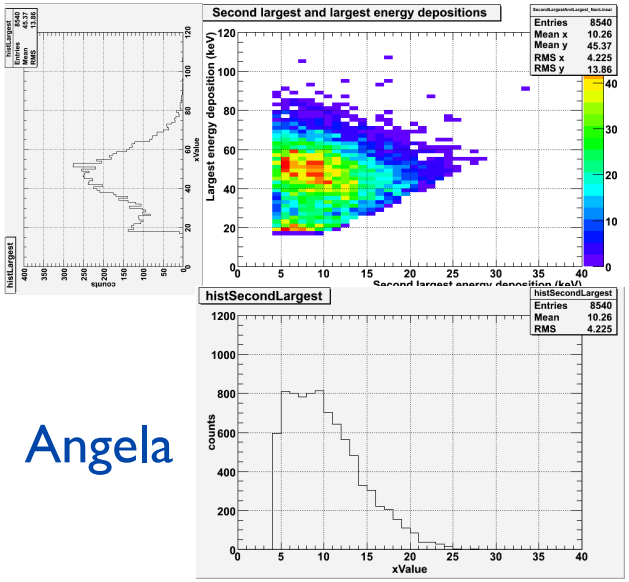

Angela

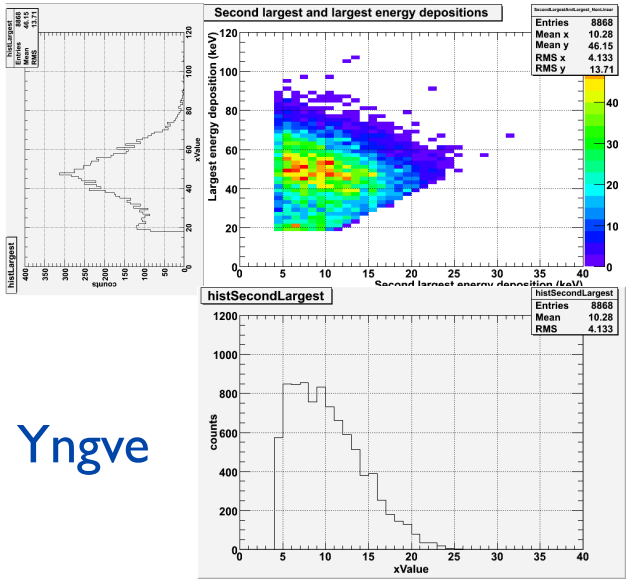

Yngve

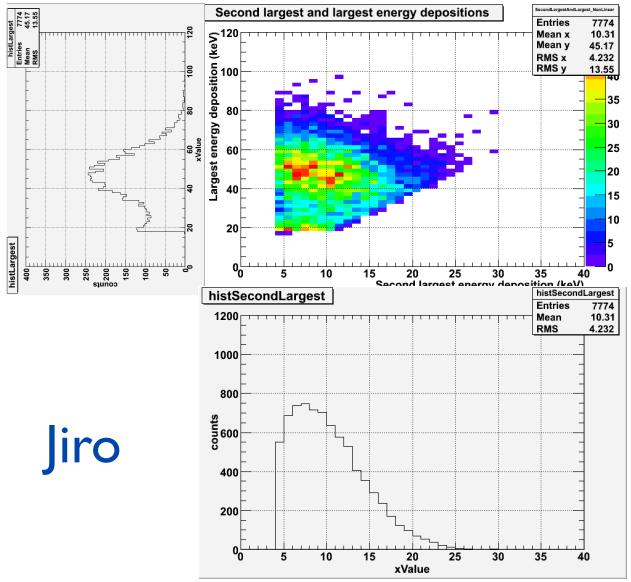

Jiro

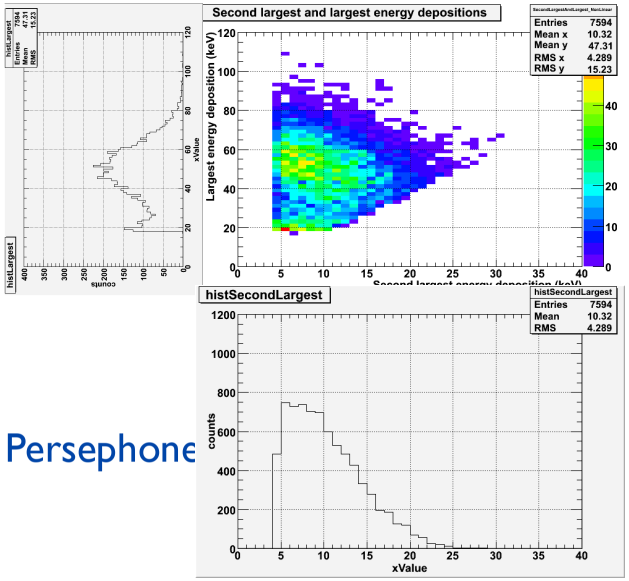

Persephone

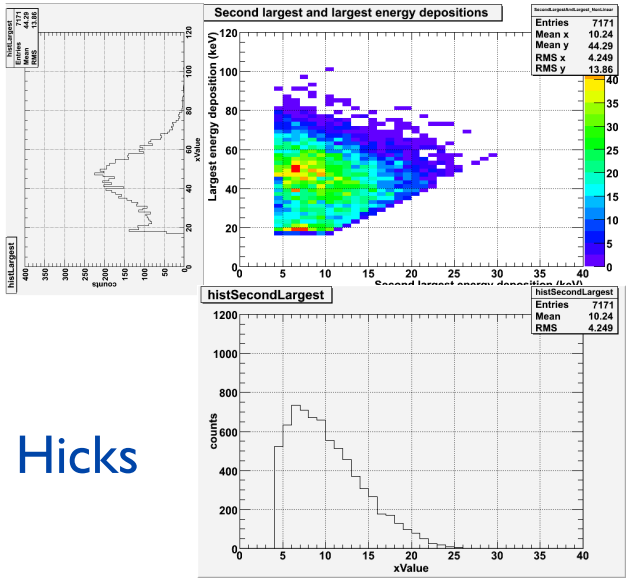

Hicks

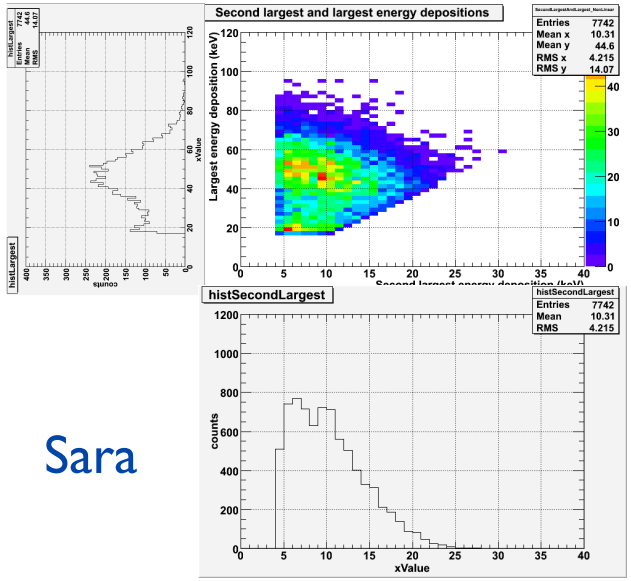

Sara

CenterIrradiating, BarretScattering, ???Absorption, Threshold 60ch

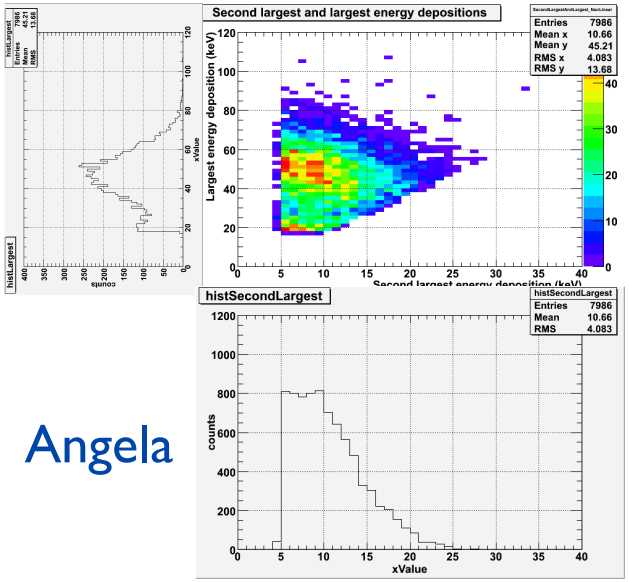

Angela

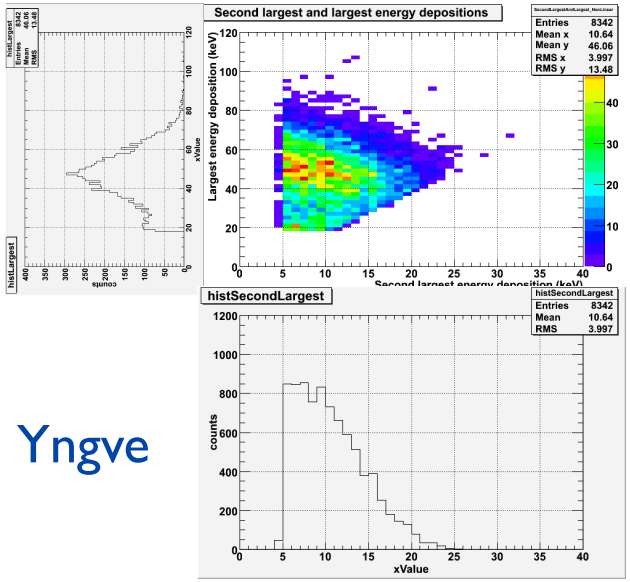

Yngve

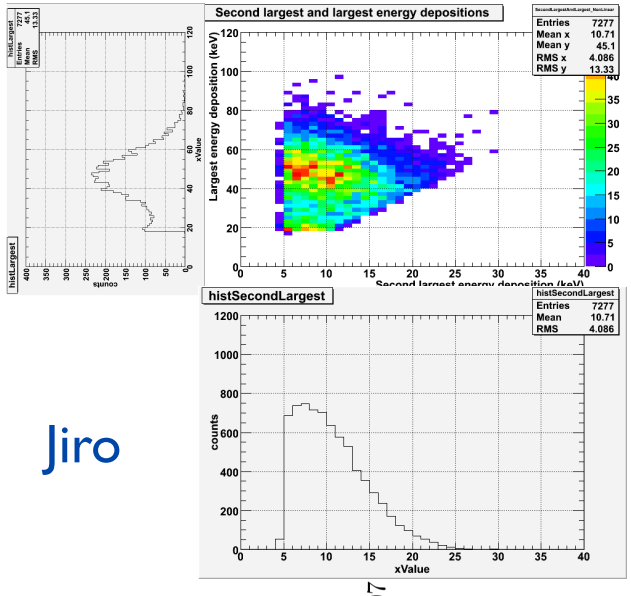

Jiro

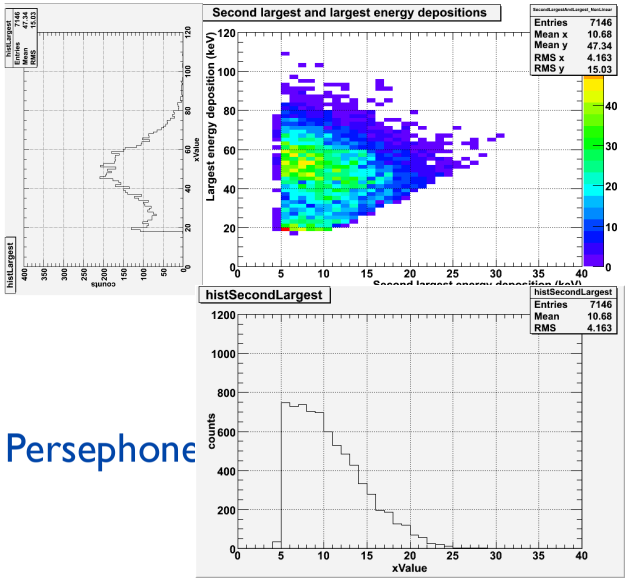

Persephone

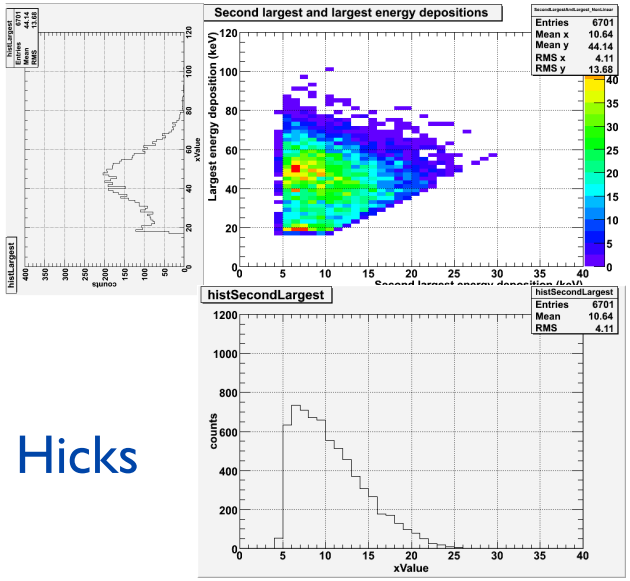

Hicks

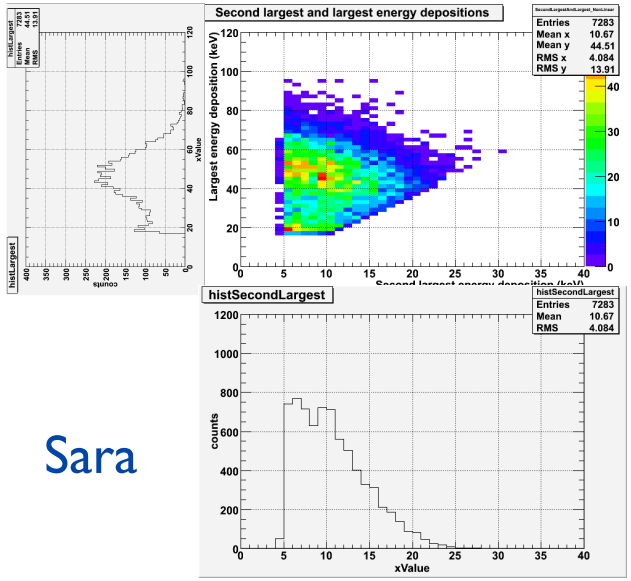

Sara

Appendix C

C.1 Comparison between scattering event and absorption event of 2-hit event based on flight-data

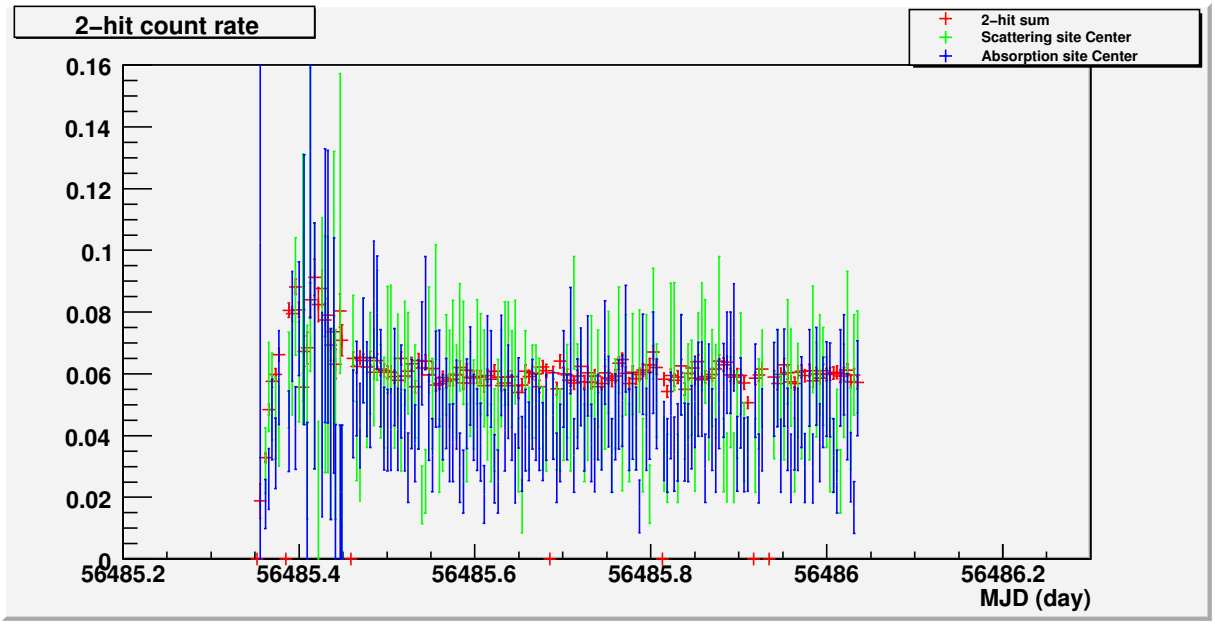

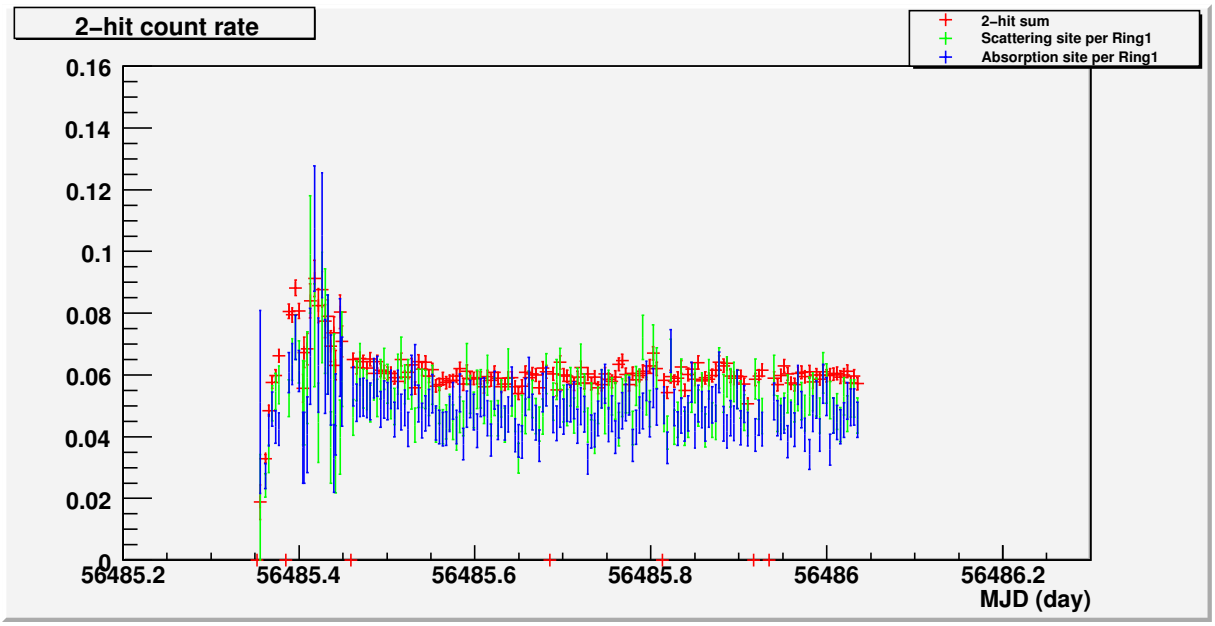
2–hit count rate
2–hit sum
Scattering site per Ring1
Absorption site per Ring1
0.16
0.14
0.12
0.1
0.08
0.06
0.04
0.02
0
56485.2
56485.4
56485.6
56485.8
56486
56486.2
MJD (day)

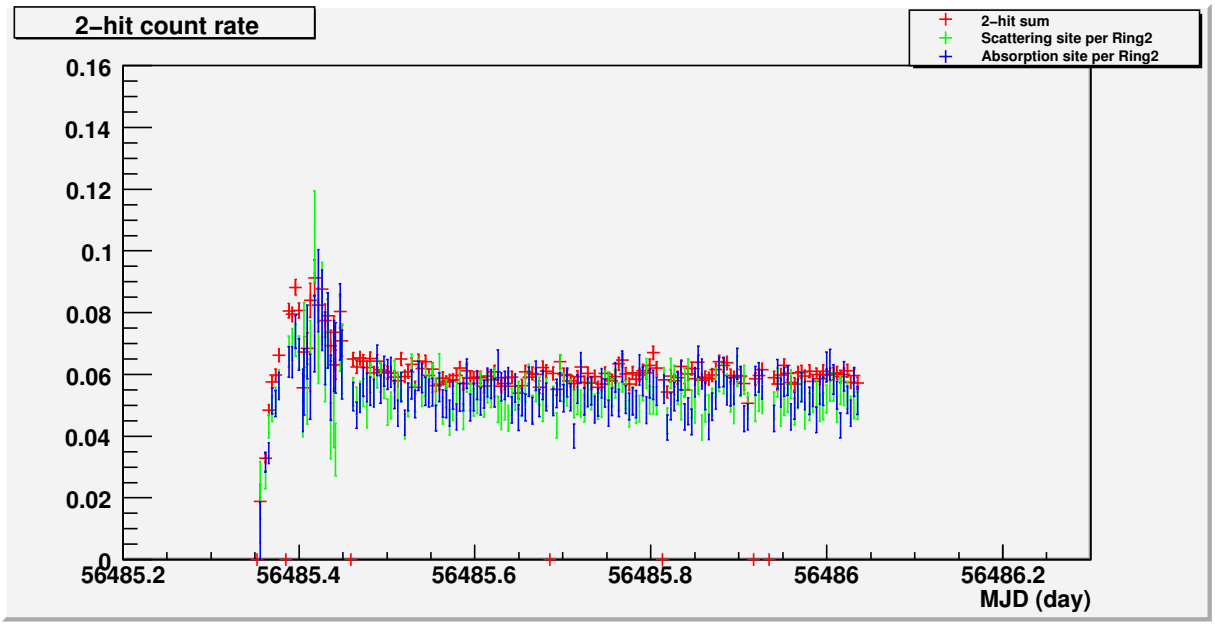
2–hit count rate
2–hit sum
Scattering site per Ring2
Absorption site per Ring2
0.16
0.14
0.12
0.1
0.08
0.06
0.04
0.02
0
56485.2
56485.4
56485.6
56485.8
56486
56486.2
MJD (day)

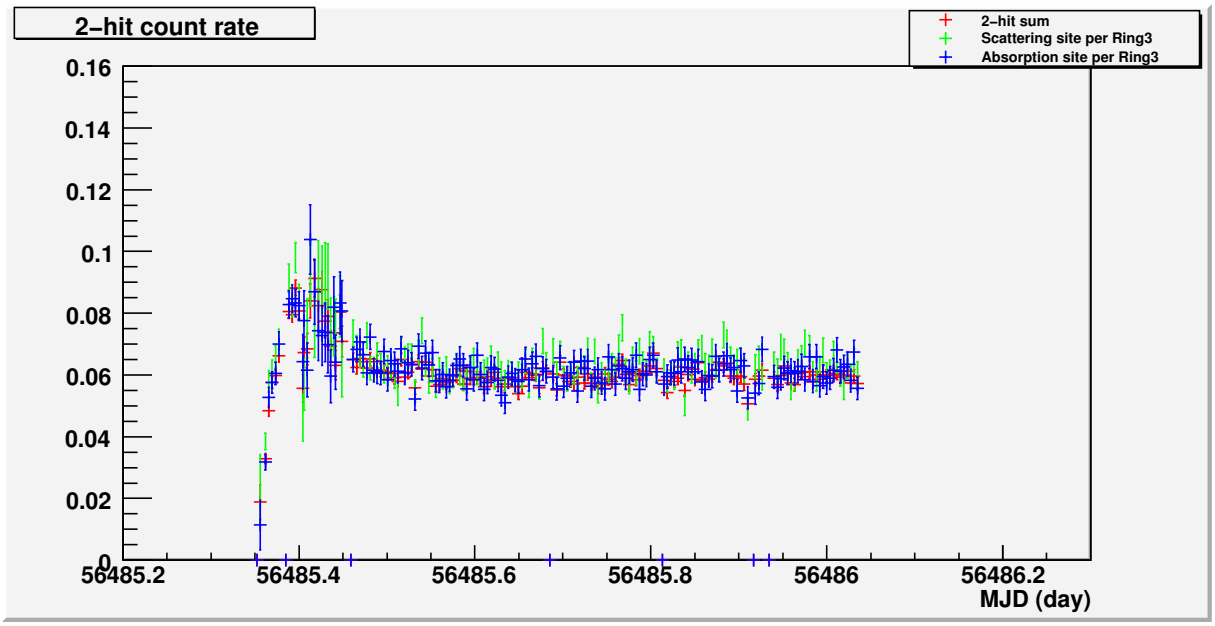
2–hit count rate
2–hit sum
Scattering site per Ring3
Absorption site per Ring3
0.16
0.14
0.12
0.1
0.08
0.06
0.04
0.02
0
56485.2
56485.4
56485.6
56485.8
56486
56486.2
MJD (day)

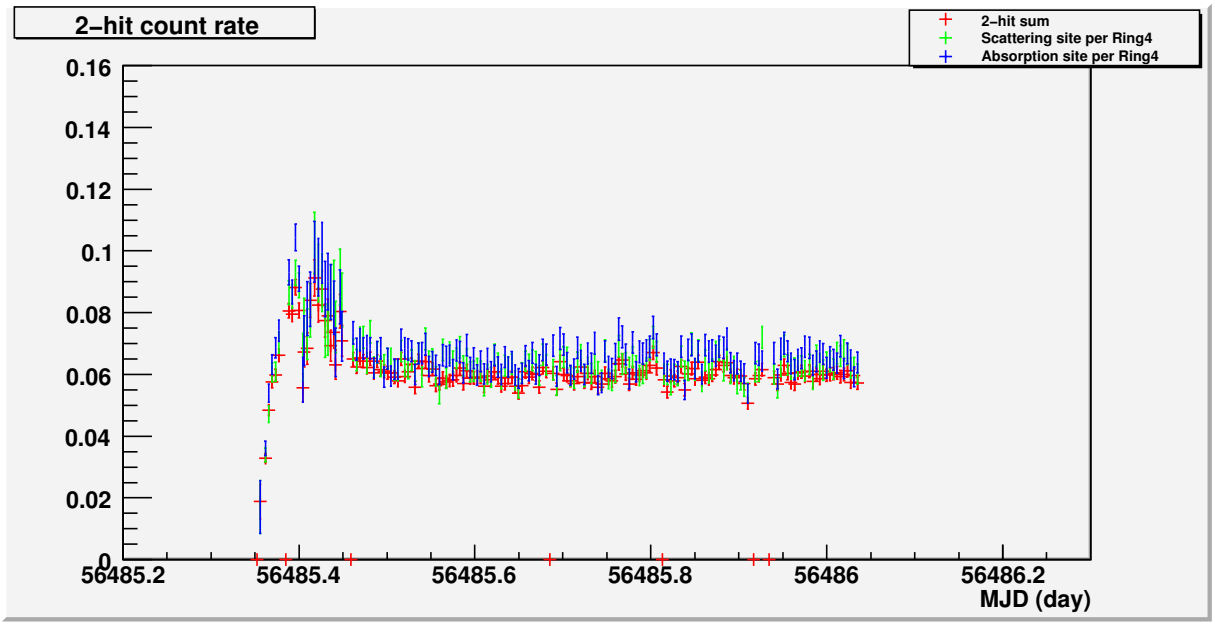
2–hit count rate
2–hit sum
Scattering site per Ring4
Absorption site per Ring4
0.16
0.14
0.12
0.1
0.08
0.06
0.04
0.02
0
56485.2
56485.4
56485.6
56485.8
56486
56486.2
MJD (day)

Appendix D

D.1 List of grand calibration data

- 2012_CenterIrr_24h_90-270.list
- 2012_CenterIrr_30m_ThroughScatter.list
- 2012_CenterIrr_600m_0-180.list
- 2012_Ring1Irr_30m_ThroughScatter.list
- 2012_Ring1Irr_505m_90-270.list
- 2012_Ring1Irr_610m_0-180.list
- 2012_Ring2Irr_30m_ThroughScatter.list
- 2012_Ring2Irr_570m_0-180.list
- 2012_Ring2Irr_625m_90-270.list
- 2012_Ring3Irr_30m_ThroughScatter.list
- 2012_Ring3Irr_600m_90-270.list
- 2012_Ring4Irr_30m_ThroughScatter.list
- 2012_Ring4Irr_925m_90-270.list
- 2012_BackGround_200min_WO_cover.list
- 2012_BackGround_250min_Lead.list
- 2012_BackGround_250min_NoHole.list
- 2012_BackGround_30min_Room.list
- 20130620_CenterIrr_250m_FastPra_90-270.list
- 20130622_CenterIrr_250m_FastPra_90-270.list
- 2013_CenterIrr_15m_Non.list
- 2013_CenterIrr_15m_Non_WO_Rotation.list

- 2013_CenterIrr_5m_1.25cmLen_2.0mmPhi.list
- 2013_CenterIrr_5m_1.25cmLen_2.5mmPhi.list
- 2013_CenterIrr_5m_1.25cmLen_3mmPhi.list
- 2013_CenterIrr_5m_2.5cmLen_2.0mmPhi.list
- 2013_CenterIrr_5m_3.75cmLen_2.0mmPhi.list
- 2013_CenterIrr_5m_5.00cmLen_2.0mmPhi.list
- 2013_CenterIrr_5m_5.00cmLen_2.0mmPhi_2.list
- 2013_CenterIrr_5m_6.25cmLen_2.0mmPhi.list
- 2013_CenterIrr_5m_7.5cmLen_2.0mmPhi.list
- 2013_CenterIrr_5m_Non.list
- 2013_CenterIrr_5m_WO_Collimator.list
- 2013_CenterIrr_5m_WO_Collimator_2.list
- 2013_CenterIrr_750m_LargePra_90-270.list
- 2013_Ring1Irr_20m_Non.list
- 2013_Ring1Irr_275m_90-270.list
- 2013_BarbieIrr_5m_2.5cmLen_2.0mmPhi.list
- 2013_BarbieIrr_5m_WO_Collimator.list
- 2013_Wall-eIrr_10m_2.5cmLen_2.0mmPhi.list
- 2013_Wall-eIrr_5m_10.0cmLen_2.0mmPhi.list
- 2013_Wall-eIrr_5m_2.5cmLen_2.0mmPhi.list
- 2013_Wall-eIrr_5m_5.0cmLen_2.0mmPhi.list
- 2013_Wall-eIrr_5m_7.5cmLen_2.0mmPhi.list
- 2013_Wall-eIrr_5m_WO_Collimator.list
- 2013_BackGround_295min_Lead.list
- 2013_BackGround_300m_Room.list

Acknowledgments

研究を指導して頂いたひろたかさんには大変感謝しています。英語も物理も拙い私に丁寧に指導して頂いたおかげで、研究を遂行することが出来ました。深澤先生には論文の添削や研究の相談など、色々とお世話になりました。研究室の皆様にも日々の生活で度々お世話になりました。

この研究を進めるにあたって、計 2ヶ月ほどスウェーデンのキルナに滞在して実験・解析を行いました。初めてキルナに滞在した M1 時は、拙い英語力と乏しい物理の知識の為に大変、大変、苦労しました。その際にもひろたかさんには、非常にお世話になりました。そこから英語の勉強を本格的に頑張り、M2 ではそこそこ喋れるようになったので生活が楽になりました。英語力って大事です。

PoGOLite 実験はスウェーデン王立工科大学を筆頭に多くの機関が参加しており、そこには多くの国籍の人が在籍しています。キルナ滞在時には、スウェーデンチームの皆様にも非常にお世話になりました。夕飯を交代で作ってチーム皆で食べる生活は、私にとっては初めての体験だったのでとても新鮮で楽しかったですし、お陰でチームの親睦も深まったと思います。お世話になった皆様へ各国の言葉で、”ありがとう”。

Dear Mark, Thank you very much.

Dear Elena, Grazie mille.

Dear Mózsi and Jan-Erik, Tack så mycket.

Dear Maxime, Merci beaucoup.

Dear Merlin, Dank u wel.

Dear Victor, Б о л ь ш о е с п а с и б о з а

(Hopefully correct...)

Skål!!

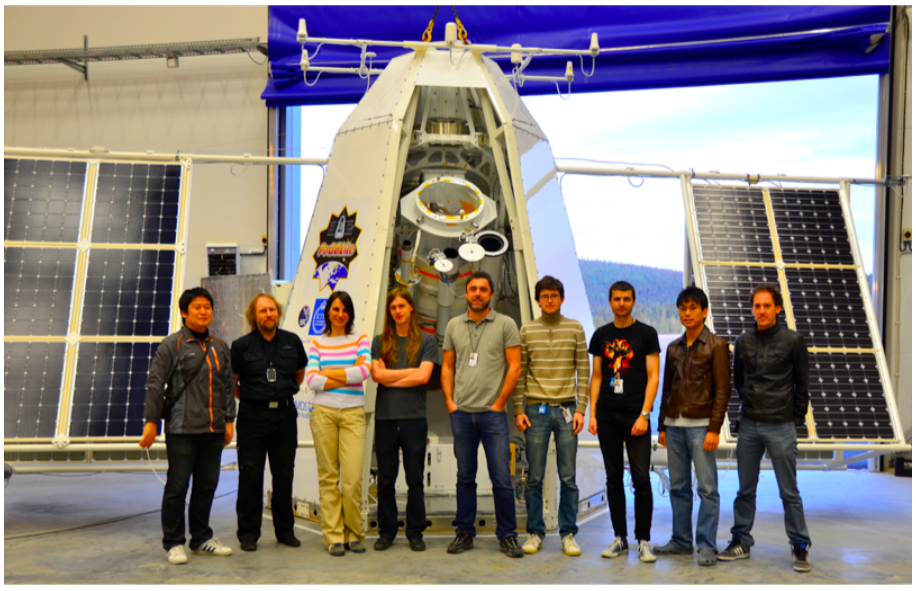

PoGOLite gondola and PoGOLite team

BIB

[1] Mzsi Kiss, Royal Institute of Technology Doctoral Thesis, "Performance Studies and Star Tracking for PoGOLite" (2011), ISBN 978-91-7415-896-0.

[2] C. Marini Bettolo, Royal Institute of Technology Doctoral Thesis, "Performance Studies and Star Tracking for PoGOLite" (2010), ISBN: 978-91-7415-641-6.

[3] 2008APh....30...72K Kamae, Tuneyoshi et al

[4] H. Yoshida, Master thesis (Hiroshima Univ. 2009)

[5] 2005NIMPA.540..158M Mizuno, T+

[6] 1975SSRv...18..389N Novick, R.

[7] 1976NASSP.389...81W Weisskopf, M. C.

[8] 2001Natur.411..662C Costa, Enrico+

[9] 1997SSRv...82..309L Lei, F+

[10] Radiation Physics and Chemistry, Volume 53, Issue 5, p. 455-459. G. O. Depaola & C. N. Kozameh

[11] Radiation Physics and Chemistry 75 (2006) 614—623 J.H. Hubbell

[12] 2008ARA&A..46..127H Hester, J. Jeff

[13] Kouzi Mori (Pennsylvania State University) Presentation

[14] 1998nspt.conf..439A Aharonian, F. A.; Atoyan, A. M.

[15] 1978ApJ...220L.117W Weisskopf, M. C. et al

[16] 2008Sci...321.1183D Dean, A. J. et al

[17] 5th INTEGRAL Workshop, 16-20 February 2004, Munich, Germany (ESA SP-552) E. Kalemci et al

[18] 2008ApJ...688L..29F Forot, M. et al

[19] Shinya Yamada (University of Tokyo) Presentation for 11th High Energy Astro Physics Association in Japan

[20] 1980ApJ...238..710L Long, K. S. et al

[21] 2008MNRAS.391...32D Doviak, M. et al

[22] 2011Sci...332..438L Laurent, P et al

[23] 2012ApJ...761...27J Jourdain, E